IMPROVING ENERGY EFFICIENCY AND PRODUCTIVITY IN INDUSTRIAL PLANTS USING DYNAMIC VOLTAGE MANAGEMENT

A Dissertation
Presented to
The Academic Faculty

by

Sathish Jayaraman

In Partial Fulfillment
of the Requirements for the Degree
Doctor of Philosophy in the
School of Electrical and Computer Engineering

Georgia Institute of Technology
May 2021

IMPROVING ENERGY EFFICIENCY AND PRODUCTIVITY IN INDUSTRIAL PLANTS USING DYNAMIC VOLTAGE MANAGEMENT

Approved by:

Prof. Deepak Divan, Advisor
School of Electrical and Computer Engineering
Georgia Institute of Technology

Prof. Marilyn Brown
School of Public Policy
Georgia Institute of Technology

Prof. Thomas Habetler
School of Electrical and Computer Engineering
Georgia Institute of Technology

Prof. Benjamin Klein
School of Electrical and Computer Engineering
Georgia Institute of Technology

Prof. Maryam Saeedifard
School of Electrical and Computer Engineering
Georgia Institute of Technology

Date Approved: March 09, 2021

To my father V. Jayaraman

ACKNOWLEDGEMENTS

I am thankful to my advisor Prof. Deepak Divan for the guidance and support throughout my PhD. Much of what I learnt is through discussions with him and the timely feedback he provided. I would be eternally grateful to Prof. Divan for the invaluable support and for helping me choose a career path. I would also like to thank the members of my reading committee – Prof. Thomas Habetler and Prof. Maryam Saeedifard for their constructive feedback during my proposal. I would like to thank Prof. Benjamin Klein and Prof. Marilyn Brown for their kind consideration and feedback. I would express my gratitude to Prasad Kandula for the guidance and the time invested in discussions. I would also like to thank Karthik Kandasamy for the guidance.

I would like to thank Frank and Suresh for their guidance. I would also like to thank Brandon and Yunkyung for their patience and support throughout my study. I would like to thank Daniela and Tasha for their guidance. I would like to gratefully acknowledge and thank the Center for Distributed Energy for supporting this work.

I would like to thank Hao Chen for helping us settle in during the initial days**.** I would like to thank Mohammadreza for the fabrication of the controller part of this thesis. I would like to thank him and my other friends with whom I have had the chance to learn from - especially Shreyas, Kavya, Rohit, Nishant, Xiangyu, Mickael, Liran, Zheng, Xiwei, Aniruddh, Priya, Kartavya and Decheng. It has been a pleasure knowing you all.

I would like to thank my mentor Sagarika and my friends as part of the prelim exam study group – Victor and Patrick for the useful discussions. I would like to thank my cousin and roommate for five years, Aravind for the support.

My family has always supported me as well as cheering me on throughout my study. I would like to thank my mother, brother, sister, and their loved ones from the bottom of my heart. I would also like to thank the Art of Living and the counseling center at GT for the mindfulness lessons. Finally, I would like to thank the Almighty for blessing me and for giving me strength to get through difficult times.

TABLE OF CONTENTS

LIST OF TABLES

LIST OF FIGURES

LIST OF SYMBOLS AND ABBREVIATIONS

ANSI	American National Standards Institute
CVR	Conservation voltage reduction
CVR_f	CVR factor
CWT	Coaxial winding transformer
COVI	‘Clamp-on’ voltage injection device
ITIC	Information technology Industry Council
LDC	Line drop compensation
LTC	Load tap changer
NC	Normally closed
OLTC	On-load tap changer
SCR	Silicon controlled rectifier
SIVOM	Static Isolated Voltage Optimization Module
PCC	Point of common coupling
ZIP	Constant impedance, constant current and constant power load

SUMMARY

Conservation voltage reduction (CVR) is an established practice of having the distribution system loads operate at the lower end of the accepted limits based on the standard ANSI C84.1 to provide reduction in power consumption. This standard stipulates optimal voltage levels where the customer equipment is expected to operate with normal performance.

CVR has been implemented traditionally by utilities by controlling the voltage on a distribution circuit to the lower end of the tolerance band defined by this standard. The effects of conservation voltage reduction are quantified by a metric called CVR factor (CVR_f). Some references have pointed out that utilities may have a concern about potential reduction in revenue they might incur due to conservation voltage reduction. CVR factor on an average at the distribution feeder level has been discussed to be 0.8.

This research investigates the mechanism of saving energy in industrial plants and suggests measures to quantify the CVR factor. The requirements of a device for voltage management are explained. The proposed solution employs coaxial winding transformers whose salient features have been discussed.

Existing solutions may have significant issues. Their limited fault handling capability makes them less robust to handle the forces and this may lead to destruction of the equipment or they may experience other issues including sluggish response or low efficiency.

CHAPTER 1. INTRODUCTION

There is a strong need to provide dynamic control of AC line voltage at low voltage and high power levels to make industrial and commercial facilities more energy efficient through conservation voltage reduction and utilities for meshed grids improve the overall system performance by reducing losses and improve the efficiency. The most typical solution in this realm uses a three-phase transformer-based system with tap changers, that provides fixed voltage reduction. Although transformer-based systems are efficient, some of these may lack dynamic response capability in the event of a voltage sag, that could expose the system to even lower voltages.

Low voltage high power meshed distribution grids such as Consolidated Edison, New York, known for high resiliency suffer poor control of the network, especially during system outages that lead to transformer overloads. Current solutions to these conditions are expensive, including upgrades of existing 1 MVA transformers. These hyper dense meshed grids are exposed to fault currents of tens of kA that could lead to harsh mechanical forces which the solution must withstand. The other significant challenge is the limited space constraint, and the solution must retrofit existing vault which is challenging. It is thus critical that the solution must be unique to address all of these issues.

Industrial users fed by dedicated feeders have the need to improve energy efficiency and reduce peak demand on an ongoing basis for targeted sections of the facility or the entire plant. They also need to continue their productivity and reduce unscheduled downtime in the event of power disturbances such as voltage sag or swell which they are

susceptible to. The solution that can address both of these issues must have a compact form factor.

Existing power converter-based solutions that are commercially available may lack the features to the above problems. Their limited fault handling capability makes them less robust to handle the short circuit forces which may destroy the equipment in the event of a fault and don't have the capability to implement behind-the-meter conservation voltage reduction to provide energy savings for the industrial and commercial plant.

The objective of this research is to investigate and develop a low-cost solution that can address the issues explained and to able to provide validation of the solution through simulation and experimental data. This thesis discusses the use of coaxial winding transformers, explaining various requirements for operation at high power levels and merits. The design of the prototype is explained along with detailed results based on experiments.

1.1 Outline of chapters

To support the objectives of the research, this work is divided into the following chapters.

Chapter two explains in detail the problem statement concerning improvement in energy efficiency and that it is beginning to gain momentum, discussing other challenges from the utility perspective. This chapter further explains that it may be possible to improve energy efficiency through physical principles such as voltage management although there has not been a widespread adoption of a solution, delving further into possible reasons.

Chapter three provides a detailed literature survey of the state of the art, methods to extract CVR factor discussed in references, load modeling as well as existing systems for voltage management. The chapter explains the need to assess the effects of conservation voltage reduction and quantify CVR factor.

The methods to quantify the effects of conservation voltage reduction and to extract CVR factor along with simulation and experimental results have been discussed in chapter four.

Chapter five explains the requirements of a device for voltage management as well as the choice of topology. The salient attributes have been explained that leads to the discussion of the proposed solution in chapter six, based on the concept of SIVOM. Detailed simulation and experimental results have been explained that shows the feasibility of the approach and the important attributes.

Chapter seven focuses on the thermal characterization, discusses the results of thermal characterization, device losses and operation at high power.

Conclusions, contributions, and recommendations for future work are discussed in chapter eight.

CHAPTER 2. PROBLEM STATEMENT

2.1 Introduction

The broader theme of the thesis surrounds improving energy efficiency in industrial and commercial plants. Regulations monitoring greenhouse emissions in the US have resulted in retirement of coal plants due to which energy efficiency is starting to gain momentum. If utilities can take advantage and extract savings out of energy through conservation voltage reduction, this would be beneficial.

It has been discussed in literature that prior to the industrial revolution, greenhouse emissions remained relatively at manageable levels. However, since then the level of greenhouse gases in the atmosphere has risen at a concerning rate. Reference [1] has explained that the CO_2 levels have increased by about 40% with a 54% increase from 1990-2011 alone. Human activity involving the burning of fossil fuel is likely responsible for rising emissions [1, 2].

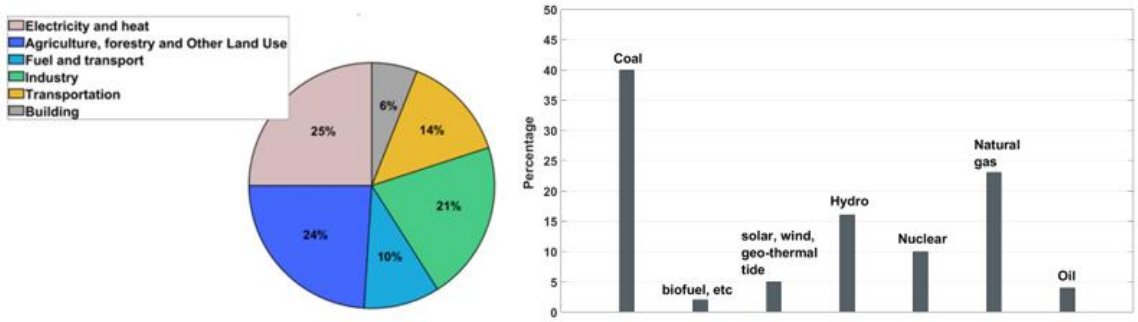

Figure 1 Emissions from different sectors and percentage contribution of different sources of electricity [1-3]

Production of heat and electricity can lead to increase in emissions as shown in Figure 1. Countries around the planet rely on coal and natural gas for heat and electricity. Reference [1] has discussed that about 70% of the electricity used are based on fossil fuel, of which 40% is accounted for from coal [3] and that development and implementation of policies that encourage improvement in energy efficiency through measures such as reduction in demand or power consumption could be encouraged as mitigation strategies [4]. In this context, a well-known concept of "conservation voltage reduction", that takes advantage of the physical relationship between voltage and demand could be a method that can be adopted [1, 5] and is discussed in this thesis.

2.2 Utility challenges and other issues

Although utilities have tried to understand the cost and benefits of conservation voltage reduction (CVR), the practice has limited adoption. From the utility standpoint, they face a variety of challenges including the ability to accurately quantify the savings that can be achieved and the associated costs with the implementation, including forgone revenue that adds to skepticism. Neither do utilities share with each other information about the best practices that they adopt for voltage regulation. References suggest that most of the load pockets where CVR is implemented are in Pacific Northwest, California, Northeast and Southeast USA[6]. The average CVR factor based on these implementations is 0.8.

The effects of CVR may be understood on the customer side of the meter. Existing published research studies have largely discussed utility projects and there is a gap in terms of quantifying the CVR factor, specifically for industrial and commercial loads. Industrial

plants have continuous process changes, that happen throughout the day that lead to load changes making CVR factor assessment challenging. Existing published research studies seem to have not discussed or analyzed the underpinning physical principle of how the reduction in power may be realized and being able to precisely understand the correlation between voltage and demand.

This research takes a detailed look at the approaches to extract CVR factor and the effects of voltage management. While this may be possible, there are other important challenges that need to be addressed. Industrial plants generally operate at higher than nominal voltages mainly because of the voltage sag issue that may be prevalent.

2.3 Voltage sag issue

Existing systems for voltage management seem to overlook the voltage sag issue. The most typical system is based on three-phase transformers with electromechanical tap changers that may have sluggish response. With the lack of dynamic response capability, there is a possibility to expose the system to even lower voltages bringing processes to a halt.

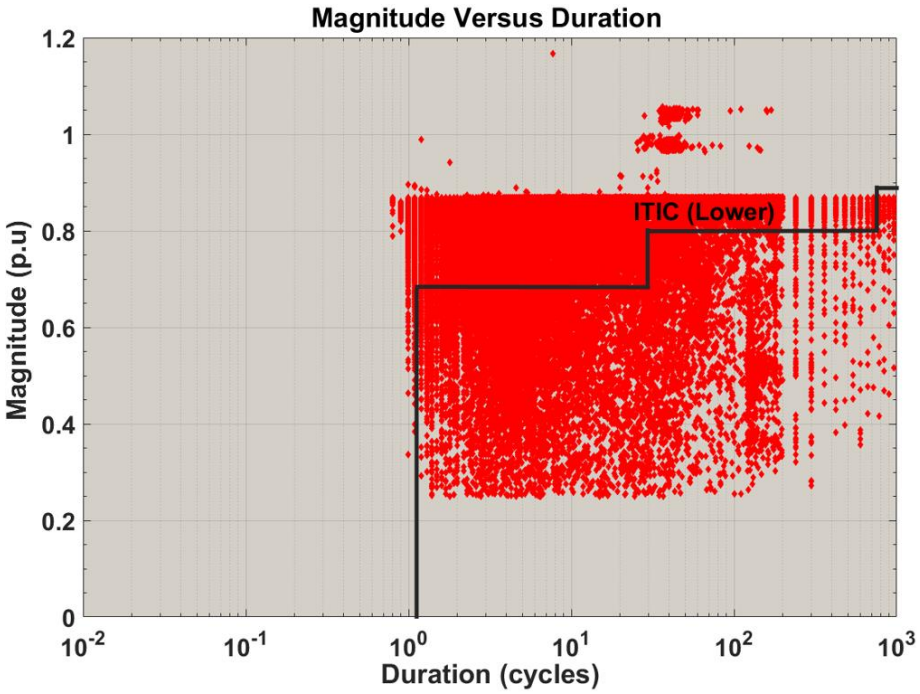

Figure 2 Voltage sag events across continental United States

Figure 2 shows one year of voltage sag events recorded by over 1800 sensors across the continental United States systematically extracted from i-Grid. More than 55,000 events are shown and a significant portion of these seem to fall outside of the ITIC limits [7] and may lead to process interruptions. Reducing voltage magnitude may increase the susceptibility of the plant to voltage sags. Additionally, the following chart shows typical voltage sag recorded by one sensor – showing a large number of events falling outside the limits.

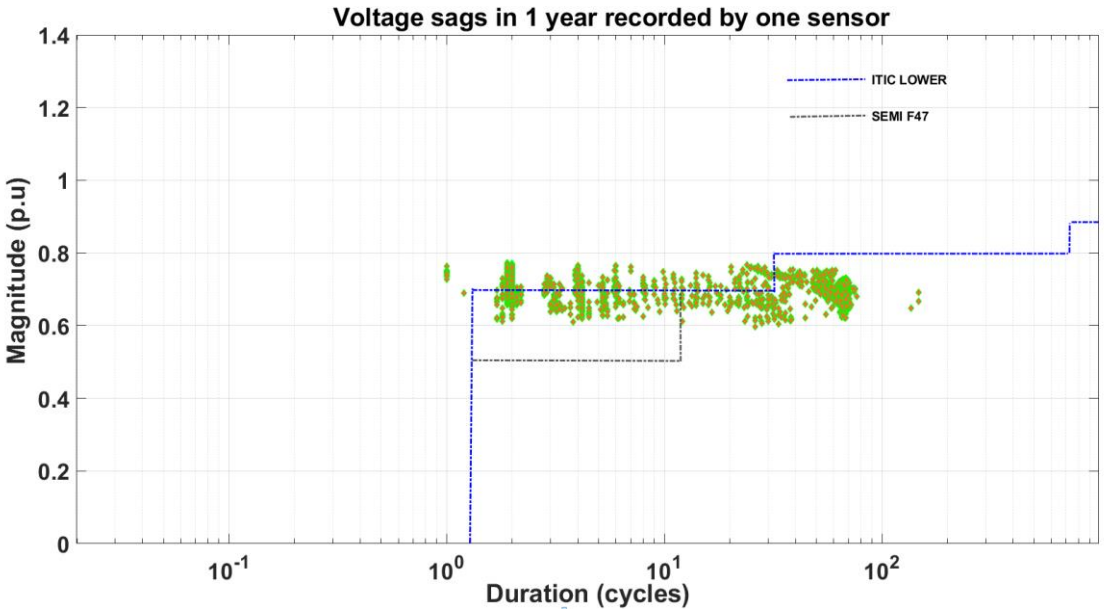

Figure 3 Voltage sag events recorded by one sensor

showing ITIC violations

2.4 Fault current handling capability

Fault current handling capability is another critical aspect for a device used for voltage management. A series connected device would need to manage fault current of tens of thousands of amperes, prevalent in industrial plants. With mechanical forces that accompany the fault, there is a need for the solution to be robust to handle the forces. Solutions based on three phase transformers may lack the capability to handle fault current experiencing structural damage. Leveraging the use of bypass and breakers may add to cost and complexity of implementation. Being able to understand and quantifying the forces under fault, would result in robust build of the solution.

2.5 Efficiency

Efficiency is another critical aspect for a device that is used for voltage management. With existing solutions, losses can potentially limit device performance. For example, if losses account for 2% in a power converter-based solution, the performance may be affected due to low efficiency. Hence, there is a need to investigate the design of a system for voltage management in industrial plants, addressing the constraints that have been discussed. Since industrial plants are designed to operate within the ANSI class A limits, significant violation from the band is not allowed. This further necessitates precise control.

CHAPTER 3. LITERATURE SURVEY

Voltage reduction could trigger a reduction in demand, although the extent to which reduction in voltage can be achieved depends on operating conditions. Sen et al. [8] and Ballanti [5] have discussed that the principle of CVR originated as a means to address an emergency situation.

3.1 Background

Conservation voltage reduction is a well-known practice of having the distribution system loads operate at lower end of the accepted limits based on the standard ANSI C84.1. By reducing voltage, CVR may lead to reduction in power, losses and provide energy savings while having the lowest customer voltage level consistent with the ANSI limits. CVR is a term familiar with the utilities and some references have pointed out that utilities may not be keen to pursue CVR because of the fear of reduction in revenue [9]. Loads are generally designed for optimal performance as the voltage varies within a voltage band as summarized in Table 1 [10].

3.1.1 Voltage Control and tolerance limits

Based on Class A limits, voltage changes at the customer end should be infrequent, and is expected to be within a ± 5% tolerance band. The Range B tolerance band is a bit more spread out. In the following table, service voltage is where the user and the electric systems of the utility are connected. Utilization voltage is at the terminals of the loads or equipment.

Table 1 Steady state voltage regulation standards

Nominal Voltage (V)	Service voltage (±5%)	Utilization voltage (+6% to -13%)	NEMA (V) (±10%)	Nameplate Voltage for Motors (V)
120	114 to 126	104.4 to 127.2	103.5 to 126.5	115
208	198 to 218	181 to 220.5	180 to 220	200
240	228 to 256	208.9 to 254.4	207 to 253	230
277	263 to 291	241 to 293.6		
480	456 to 504	417.6 to 508.8	414 to 506	460

3.1.2 CVR factor

The metric used to quantify the effects of conservation voltage reduction is called CVR factor. As documented in the literature, the CVR factor of resistive loads is 2, for constant current loads the CVR factor is 1 and for constant power loads, CVR factor is 0. A system consists of a mix of these loads that change continuously, leading to changes in CVR factor

$$CVR\ Factor = \frac{Percentage\ change\ in\ power}{Percentage\ change\ in\ voltage} = \frac{\Delta P\ \%}{\Delta V\ \%} \quad (1)$$

Figure 4 and Figure 5 show the conceptual representation of CVR, based on a MATLAB simulation showing change in power consumption as the voltage changed from 500 V to 460 V for a 50 kW constant current and constant impedance load.

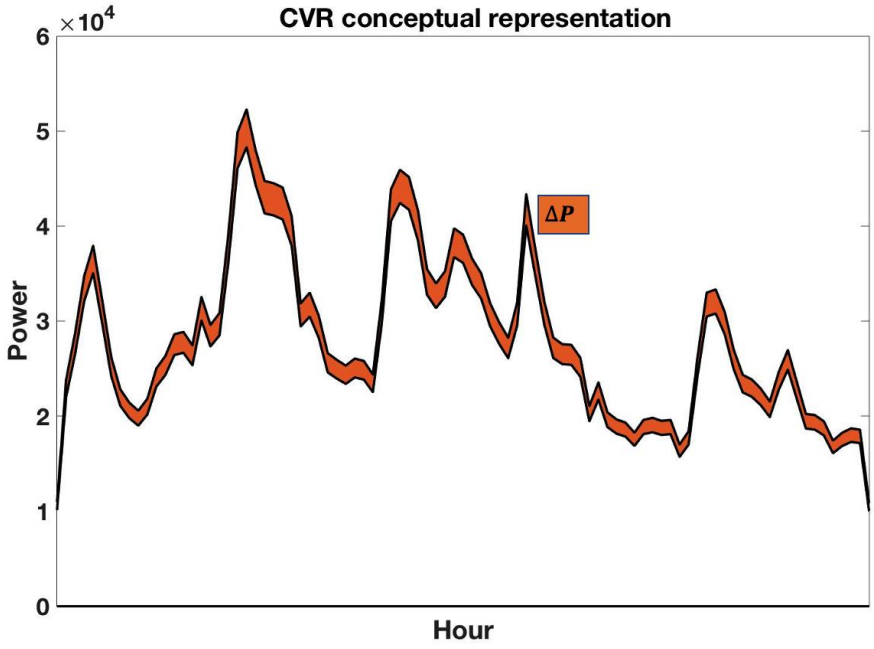

Figure 4 Change in power consumption of a 50 KW constant current load for a voltage change from 500 V to 460 V.

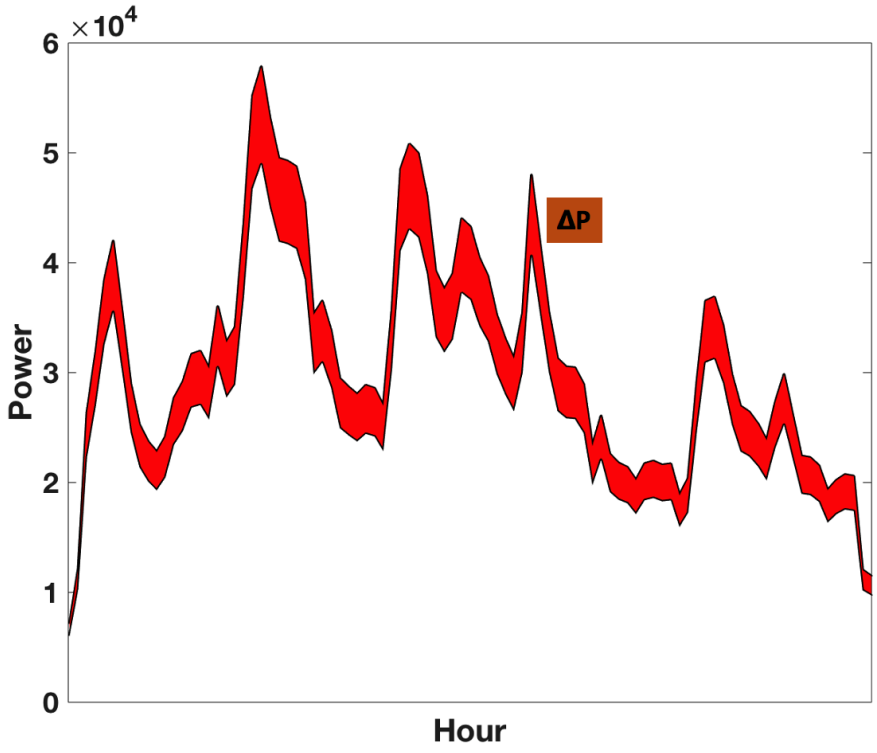

Figure 5 Change in power consumption of a 50 KW constant impedance load for a voltage change from 500 to 460 V

3.1.3 CVR projects

While reviewing literature, it was observed that a handful of CVR projects at the distribution feeder level have been published - some of them in the 1980s and 1990s. A credible research work that explains the effects of CVR in industrial systems seems to be missing.

3.1.3.1 CVR factor reported in literature

Reference [11] has discussed some of the early CVR projects. American Electric Power [12], Bonneville Power Administration [13] , Southern California Edison [14], BC Hydro [15], SMUD [16] are some entities that have reported CVR factor shown in Figure 6. Efforts are being made in the industry and academia to understand CVR due to the

increasing awareness about depleting non-renewable resources, stringent environmental protection requirements and incorporating smart grid infrastructure in distribution systems.

One of the earliest research studies on the impact of reduced voltage on the operation and efficiency of major loads is presented in reference [17]. However, impacts of slip and saturation with industrial loads have not been discussed. Reference [9] discusses of a potential concern that utilities might have with regard to reduction in revenue as a result of CVR.

The following chart (Figure 6) summarizes CVR factor results reported by different entities and the references have been cited subsequently. There have been challenges to widespread adoption. The technical barriers seem to be mainly due to lack of coordination between existing devices to reduce voltage effectively [11], challenges around assessment of CVR effects and being able to understand the underpinning physical principles, which this work tries to investigate.

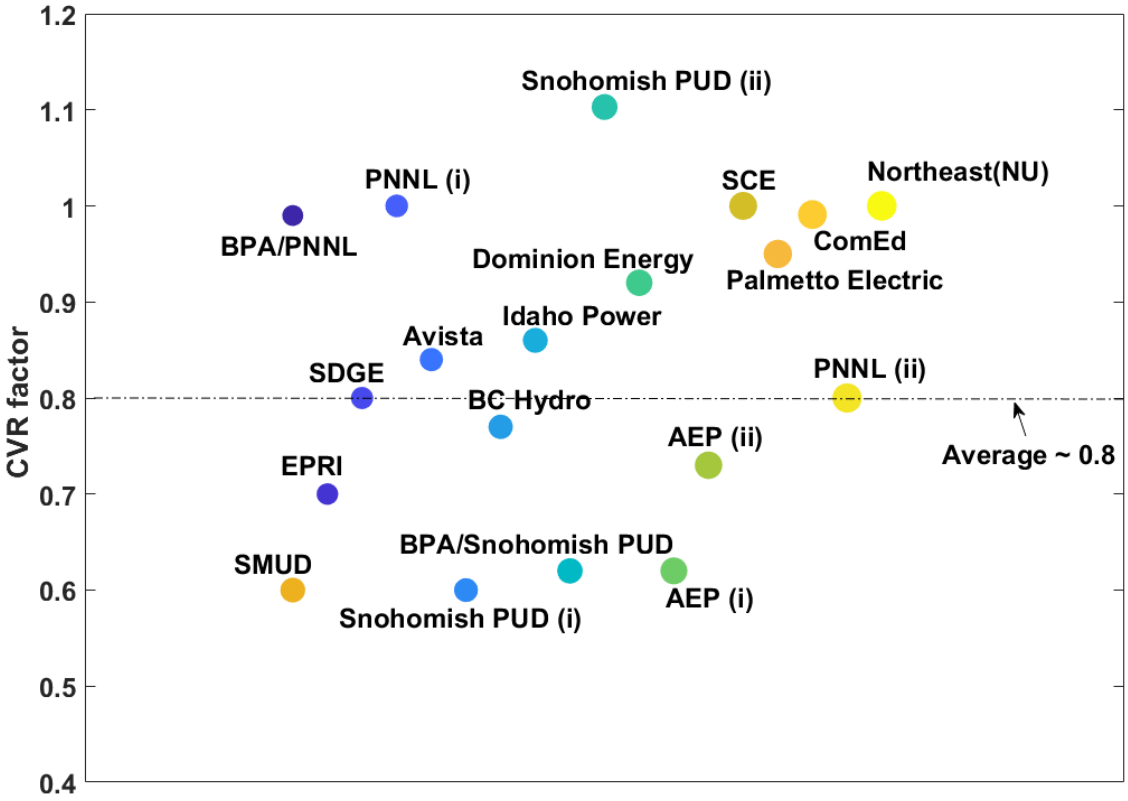

Figure 6 Summary of CVR factors based on projects by various entities

The techniques adopted by utilities seem to leverage existing volt/var control and distribution automation systems. In low and medium voltage power distribution systems there are a few ways voltage is controlled typically [5, 18]. Transformer tap changers, voltage regulating transformers, line drop compensators and switched capacitors have been discussed in literature.

3.1.3.2 Typical approaches for voltage management

Load tap changers (LTC) are devices that are used to change the voltage in discrete steps. They can be classified as on-load tap changers (OLTC) and off-load tap changers. The off-load tap changer is located on the low voltage side of the distribution transformer whereas an OLTC is typically located on the low current winding. The former is used when

an interruption in power can be tolerated and reference [1] has discussed that these have been the typical tap changing devices used in European-style distribution systems for economic reasons. In an OLTC, the transformer may not be de-energized during a tap change from one tap setting to the other and for a short period of time, a large amount of current could cause thermal stress on the taps as they are shorted. In order to minimize the short circuit current, the taps are located on the low current side in an OLTC. A photograph of an OLTC is shown in Figure 7. Electromechanical tap changers are sluggish devices and require regular maintenance due to wear and tear. Figure 8 shows the schematic of a tap changer that shows a tap selector to change from the initial to final tap positions.

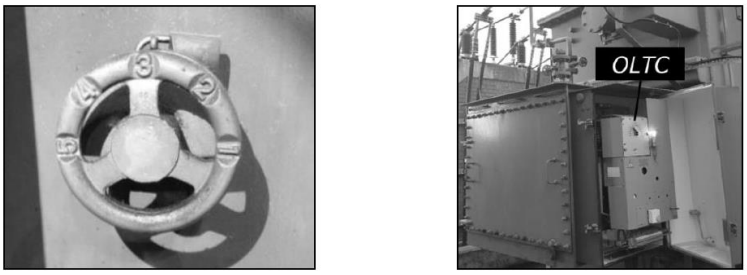

Figure 7 Photograph of an OLTC [5]

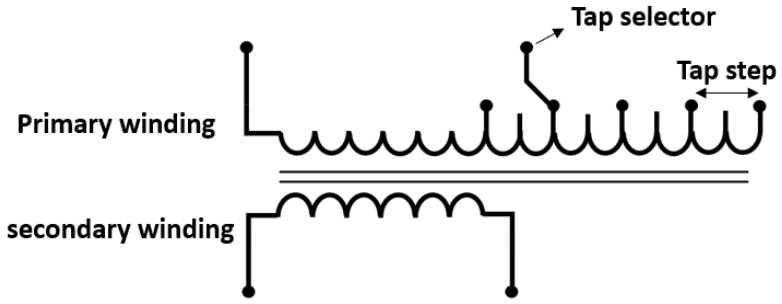

Figure 8 Schematic of a tap changer [5]

Capacitors provide voltage boost and generally flatten the voltage profile along the circuit [19] by supplying leading reactive power. These may be used together with voltage

regulators to manage customer voltage. By flattening the voltage profile, it may be possible to achieve deeper voltage reduction. [19]. A photograph of a capacitor bank is shown in Figure 9.

Figure 9 Capacitor Bank [5]

Capacitors are switched in or out with circuit breakers or switches, that may have a response time of ~100 ms. Capacitors may be used for steady state studies (CVR) and may be ineffective under low voltage conditions to provide sufficient voltage support [1].

Voltage regulators and line drop compensation methods are the other typical implementation by utilities. Voltage regulators are auto transformers with automatically adjusting taps [19]. Line drop compensation (LDC) augments load tap changers and voltage regulating transformers. LDC uses an internal model of the distribution line impedance, where R and X values could be adjusted to achieve required compensation [19]

3.1.3.3 A brief discussion of CVR projects

The project by Idaho Power is discussed in references [8, 20]. A reduction in voltage of 3% yielded a demand reduction of up to 2.6 % and a CVR factor of 0.86 is reported. Reference [21] has discussed the work by Palmetto Electric Coop presented at the REPC'13 conference. Energy savings of 3.3% is discussed. Reference [22] discusses

a CVR project based on one year of field trial utilizing a day on and day off approach with an average CVR factor of 0.7. Reference [23] discusses the impacts of CVR based on feedback from AMI infrastructure by Dominion Virginia Power based on load tap changers.

References [24, 25] discuss the work by Pacific Northwest National Laboratory based on modeling studies to understand the impacts of CVR in a software called GridLAB-D [26]. References [27, 28] discuss results of CVR tests at Snohomish PUD (NW Utilities). CVR tests were performed on an alternating 24-hour cycle of normal voltage and reduced voltage. The circuits utilized line drop compensators based on current sensing at the substation. The CVR factor based on tests by Northeast Utilities is discussed in reference [29]. Reference [30] discusses the work by Commonwealth Edison. Reference [31] discusses CVR tests performed by San Diego Gas & Electric Company. Reference [32] discuss the work by Avista Utility to understand the impacts of CVR using smart metering infrastructure. Recently there have not been many projects.

3.1.4 Associated issues

Voltage variation is not desirable due to unnecessary process changes that may be induced. Voltage changes could occur locally due to cycling of loads, could occur due to energizing or de-energizing of adjacent loads as well as actions impacting a larger part of the utility system as the electric problems are resolved. Optimal voltage levels shall ensure loads can deliver adequate performance. Undesirable voltage might affect process speed and could lead to process interruptions as well as shorten life of equipment. [33]

Voltage sags may lead to loss of productivity in industrial plants and a device for voltage management should address voltage sag issue. A solution to address voltage sag [34, 35] is shown in Figure 10. Most of these are short duration events (1-6 cycles) represented in Figure 11, corresponding to the clearing time of upstream utility protective equipment such as fuses, breakers etc.

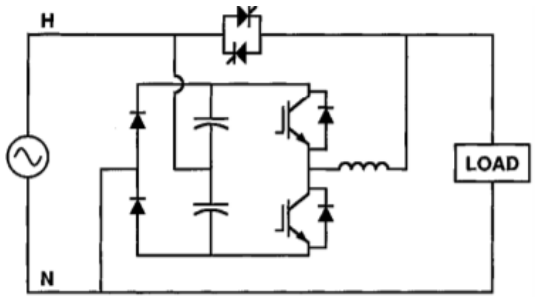

Figure 10 Dynamic sag corrector [35]

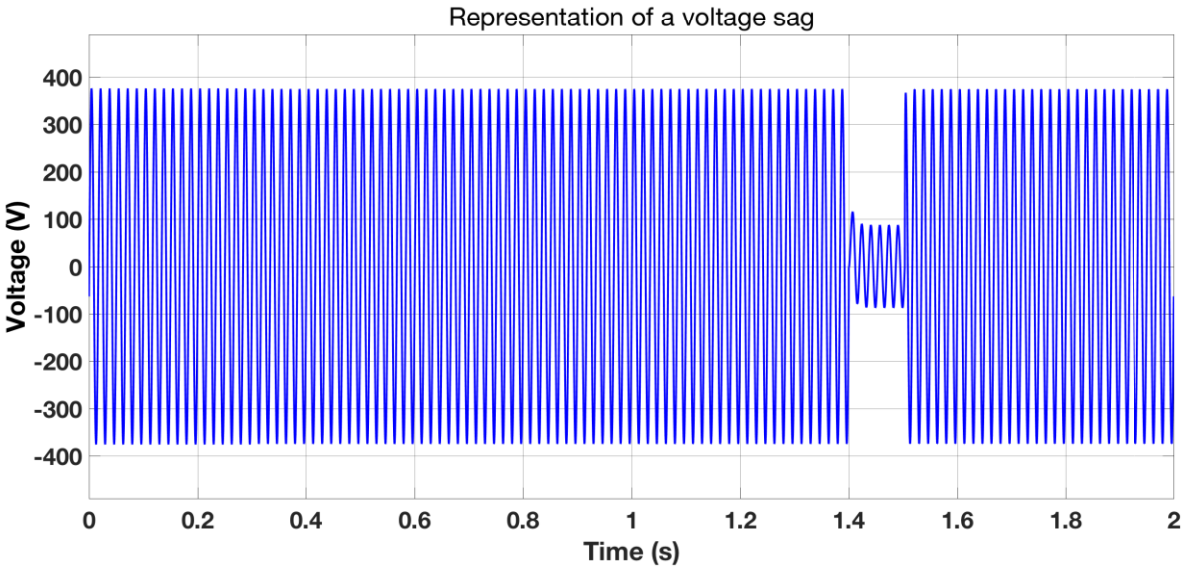

Figure 11 Representation of a voltage sag event caused by a single line to ground fault simulated in MATLAB

Typically to tackle the sag problem, industrial plants operate at higher than nominal voltage levels.

With some of the existing systems, there may be considerable amount of losses or these systems may have limited capability to handle a fault, necessitating the use of bypass and breakers as well as sluggish response.

3.1.5 Assessment of effects of conservation voltage reduction

Analyzing the effect of CVR requires accurate modeling of the load and being able to validate the model through experiments. Review of literature showed that there is a gap in terms of accurately quantifying CVR effect or validating the underpinning physical relationship between voltage and demand. This thesis tries to address this gap, with industrial systems as the targeted loads. CVR assessment methods discussed in literature are usually component-based or comparison-based approaches.

3.1.5.1 Synthesis (component) based approaches

Component-based approach is based on building up the load model from its fundamental building blocks [36, 37]. The load for different categories such as residential, or commercial loads are classified based on a survey and modeled as building blocks such as lighting loads, space heating, cooking range, elevators, refrigerators, and air conditioning loads. A mathematical function relates voltage and power based on experiments performed on individual loads (quadratic or exponential function). From the mathematical function, the CVR factor could be obtained. The disadvantage of this modeling approach is the difficulty involved in applying such an approach for large

systems such as industrial plants. Process variability in an industrial plant that happens throughout the day leads to changes in load and such a dynamic behavior should be properly understood. [30, 38] have used synthesis-based approach to estimate CVR factor. The load share of each equipment is obtained such that the total energy consumption E_{total} is computed as given by Equation (2)

$$E_{total} = \sum_{j} E_j(V)\, S_j \tag{2}$$

Where E_j represents the energy consumption of the equipment j

S_j represents load share of the appliance j.

Synthesis based approach assumes that appliances in real applications behave and are operated the same way as they are tested in lab environments without accounting for the varying nature of processes. In addition, it may be difficult to accurately obtain the load share of different appliances precisely to predict the CVR factor of the system.

3.1.5.2 Comparison based approach.

There are two kinds of comparison methods. First approach is based on measuring the CVR effects on two feeders with similar load mix and configurations as well as that are in close locations. Voltage reduction is applied to one feeder and nominal voltage is applied to the second similar feeder, at the same time.

The other approach is to apply voltage reduction to a test feeder on day one and on another day, nominal voltage is applied to the feeder. Based on the measurements from the

two tests, the CVR factor can be calculated. The challenge with this approach is that the impact of weather changes and measurement noises that might blur the effect of CVR. Reference [28] has discussed this methodology to estimate CVR effects at Snohomish PUD on an altering normal voltage day and reduced voltage day. The CVR tests started in colder season and compensation for the weather changes is discussed. The CVR test day was paired with a colder non-test day and a warmer non-test day and the weighted average of the two was used to extract CVR factor. Reference [11] has discussed that comparing a test day and a non-test day when some factors including weather, load conditions might have changed needs to be properly justified.

3.1.5.3 Regression based approach

Another technique employed to extract CVR factor is based on a regression-based approach, in which measurements of reduced voltage and load are used. In regression-based methods, loads are modeled as a function of their impact factors (Example: Temperature). Models for the normal-voltage load levels are identified using linear regression, and their outputs are compared with the measured reduced-voltage load to calculate the CVR factor [11]. The procedure assumes a linear model for load with a linear dependence on temperature, voltage, and other factors. Multivariate regression may be used to detect sensitivities of load to the impact factors. Such a model may be formulated as given by Equation (3) [11]

$$L = \alpha_0 + \alpha_1 T + \alpha_2 \Delta V + \varepsilon \quad (3)$$

Where L represents normal voltage load, ΔV represents the measured depth of voltage reduction, α_0 is the basic load component, α_1 is the temperature dependence component, α_2 captures voltage dependence and ε represents errors. α_2 is used for CVR factor calculation [11].

3.1.5.4 Simulation based methods

Simulation methods are based on system modeling and power flow calculation. This method simulates what the load consumption is without voltage reduction. Power flow is run based on measured operation data and weather information. The difference between power flow results and measured load consumption is used to calculate CVR factor. The challenge with this approach is to have accurate and detailed models and it may be difficult to build models for all existing and emerging load components.

CVR factor may vary with time and the model should be dynamic to account for changes in feeder and load behavior [11, 24]. References [39, 40] have discussed a simulation based approach to estimate the effects of voltage reduction on Taipower feeder. Reference [24] has employed a mostly simulation-based approach to understand the effects of CVR with an open source software GridLAB-D. If the models are detailed and accurate, simulation-based approaches may be used to understand CVR effects. Reference [41] has discussed a simulation-based approach to find that load to voltage sensitivity of a feeder with a high penetration of distributed generation may vary with time. Existing simulation-based approaches seem to be component based and this may make it too difficult to accurately understand a large system such as an industrial plant, where there are continuous changes in load due to process variations that occur throughout the day. Being able to

validate the model with real measurements and experiments, provides a more reliable means to understand effects of CVR.

3.1.5.5 Load model

Two broad modeling approaches employed within the framework of CVR assessment are static and dynamic models. Static load models are used to relate voltage and power measurements through a mathematical equation. This could be a ZIP model or an exponential model. Reference [42] has discussed that if the objective pursued is to understand the impact of small changes in voltage on load, such as defining the sensitivity of load to voltage change, static models may be used.

Representing the load as a polynomial function leads to traditional ZIP load models, where the load is modeled as a combination of constant power, constant current and constant impedance loads. Figure 12 represents a ZIP model.

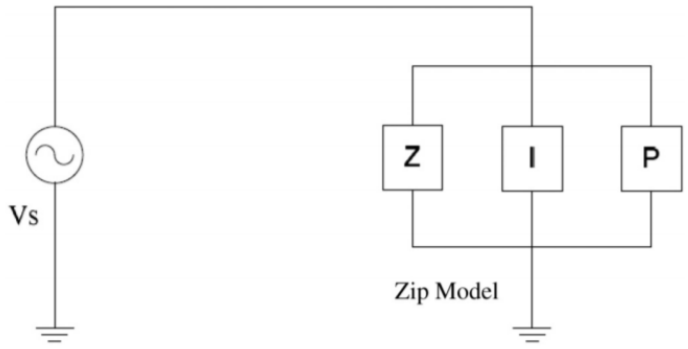

Figure 12 Load represented as a 'ZIP' model

Sum of constant impedance, constant current and constant power components equal 1. Reference [36] has provided ZIP load parameters extracted from some end user loads. Equation (4) shows the voltage power relationship based on a ZIP model [43].

$$\frac{P}{P_{nom}} = a_o + a_1\left(\frac{V}{V_{nom}}\right) + a_2\left(\frac{V}{V_{nom}}\right)^2 \quad (4)$$

a_o captures the constant power behavior of the load

a_1 captures the constant current behavior of the load

a_2 captures the constant impedance behavior of the load

P represents the power measured at applied voltage V

P_{nom} represents the nominal power at nominal voltage V_{nom}

The constituent load components in a ZIP model are the constant power load component, constant current load component and constant impedance load component. Constant power component has a constant amount of power independent of the supplied voltage to the load. In general, electronic converters, power electronic drives as well as power supplies are examples of constant power load [5]. Constant current component captures linear relationship between voltage and power, an example of such a constant current load is a lighting load (CFL) [5]. A constant impedance component captures the quadratic relation exists between power and voltage. Examples of such a load type are resistors, heaters etc., Equation (5) yields the CVR factor based on ZIP model

$$CVR_f \stackrel{\text{def}}{=} \frac{dP}{dV} = 2a_2 + a_1 \quad (5)$$

$$a_2 + a_1 + a_o = 1 \quad (6)$$

The second model discussed in the literature is the exponential model that relates the power and voltage by an exponential function given by Equation (7). This model has fewer terms. Qualitatively both ZIP and exponential models are similar and have been extensively applied in literature. [36, 42].

$$\frac{P}{P_n} = \left(\frac{V}{V_n}\right)^{a_p} \tag{7}$$

$$a_p \approx \left(\frac{P - P_n}{P + P_n}\right)\left(\frac{V + V_n}{V - V_n}\right) \tag{8}$$

a_p is the exponent that yields the sensitivity of demand due to changes in voltage, given by Equation (8). The following table shows for representative scenarios a comparison between coefficients based on ZIP model and Exponential Model

Table 2 Coefficients to relate ZIP model and Exponential Model

Exponential Model (a_p)	Constant Impedance Component (a_2)	Constant Current Component (a_1)
1.7	0.65	0.4
1.7	0.55	0.6
1.5	0.55	0.4
1.5	0.5	0.5

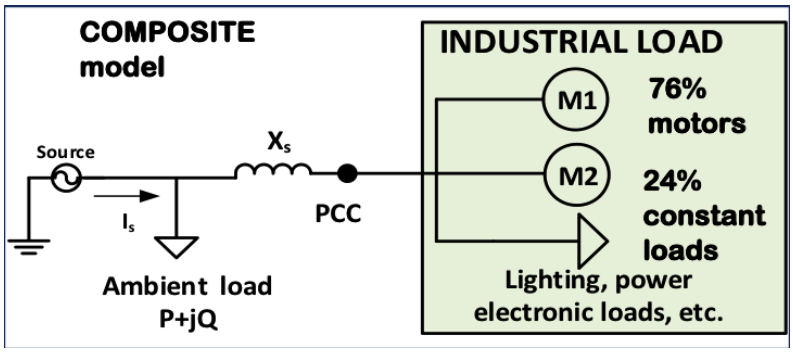

Figure 13 Composite load model with motor loads and constant loads

The ZIP model equation for reactive power is given by Equation (9)

$$\frac{Q}{Q_{nom}} = K_{zq} + K_{iq}\left(\frac{V}{V_{nom}}\right) + K_q\left(\frac{V}{V_{nom}}\right)^2 \tag{9}$$

K_q captures the constant power behavior for reactive power

K_{iq} captures the constant current behavior for reactive power

K_{zq} captures the constant impedance behavior for reactive power

Q represents the reactive power measured at applied voltage V

Q_{nom} represents the nominal reactive power at nominal voltage V_{nom}

The exponential model for reactive power is given by Equation (10)

$$\frac{Q}{Q_n} = \left(\frac{V}{V_n}\right)^{n_q} \tag{10}$$

n_q is the exponent that yields the sensitivity of reactive power change to changes in voltage [44].

The third type of load model that is discussed in literature is a composite model that captures the dynamic behavior of certain kinds of loads. These have been discussed in references [45, 46]. Instead of having purely constant loads (ZIP), these use motors in combination. With this model, the unique characteristics of specific loads could be studied. Reference [45] has suggested a dynamic model that might include motors that constitute 76% of the total load and static load that accounts for 24% to model an industrial plant applied in this research. As authors have shown in [47] the impact of voltage change for a motor load depends on the type of load fed by the motor. An analysis corresponding to quadratic torque load, linear torque and constant torque load fed by an induction motor showed the nonlinearity in the type of load can give savings in demand as discussed in subsequent sections.

This research has applied an experimentally validated approach to extract CVR factor. Detailed simulation and experiments were performed to understand the feasibility before applying the technique. In this regard, there is a need to accurately assess process variations that occur throughout the day that may lead to load changes. Being able to understand and properly discriminate real voltage changes from the entire measurements of voltage and power is extremely important and challenging to be able to accurately extract CVR factor. The subsequent chapter discusses extraction of CVR factor in a plant.

CHAPTER 4. EXTRACTION OF CVR FACTOR IN A PLANT

Motor loads are the dominant loads in industrial environment. Applications of such motors used are discussed in [17, 42]. Induction motors are typically line connected, operating at poor power factor. With resistive loads, there is direct reduction in power due to reduction in voltage. However, with motor loads the mechanism of reduction in power is unclear. Slip, type of load and saturation are three main factors affecting motor CVR factor. An analysis was done between three types of loads (square law torque, linear torque and constant torque load) fed by line connected induction motors and it was observed that a change in voltage led to most demand savings in a quadratic torque load as compared to linear torque and constant torque load shown in Figure 15

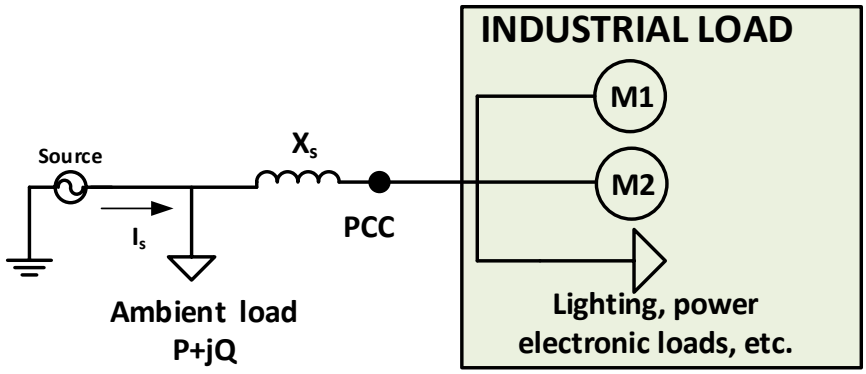

Figure 14 Schematic of a representative industrial load.

A typical industrial plant has a mix of loads – motors (mud pump process, industrial mixers), resistive loads (lighting, heating), constant power loads (electronic loads, drives). The CVR_f for the whole plant depends on the ratio of different loads, which are continuously changing during the day, The CVR_f for resistive loads is well known to be

2.0 and for constant power loads it is zero. The CVR_f for motor loads in not well-known. One of the few research studies on the impact of reduced voltage on the operation and efficiency of major loads is presented in [17]. Other research studies have discussed that lightly loaded induction motors provide higher CVR factor. [19]

Figure 15 shows the effect of slip, where a change in voltage from 500 to 460 V led to most demand savings in a quadratic torque load as compared to linear torque or constant torque load.

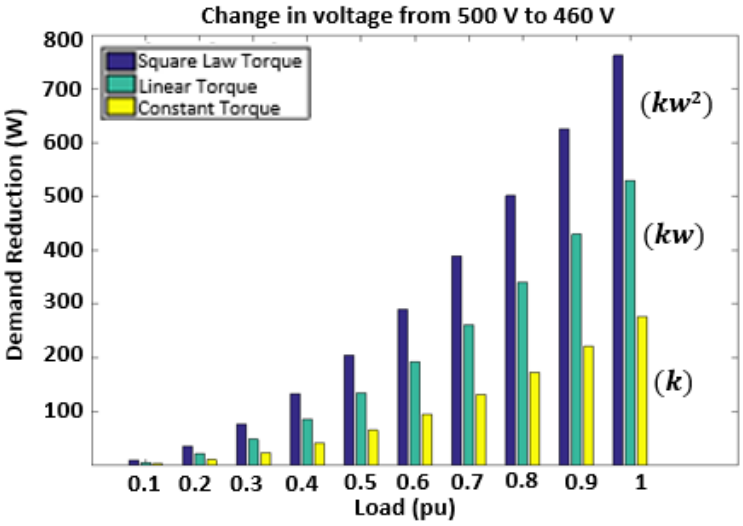

Figure 15 Comparison of various types of loads

Early experimental results with a variac in a lab environment showed that lightly loaded induction motors have higher CVR factor – with the highest CVR factor at conditions of no load ($CVR_f = 2.8$) and reduces as the loading levels increased. However, in an industrial plant, process changes lead to continuous changes in load making it difficult to predict the impact of voltage change on power consumption.

It is hence important to understand the level of demand/energy savings and productivity improvement that can be realized using voltage management at an industrial plant. While the contribution of one load (resistor, lighting loads [5]) or a partially loaded motor may be a small number, if the same principle is applied to several of these loads in a plant, the CVR factor of a plant may be extracted.

4.1 Existing approaches to extract CVR factor

A schematic of a plant is shown in Figure 14, it can be seen that at a plant level there can be numerous process changes leading to continuous changes in load. Current approaches seem to have not looked the physics of the relationship between voltage and demand, tending to overlook the changing nature of the industrial processes that might make CVR factor extraction challenging.

4.2 Challenges with CVR assessment methods

Approaches discussed in [10, 11, 24, 48] could applied to voltage and power measurements at the customer point of common coupling (PCC). The challenge with these techniques relies on being able to extract useful information from multiple data points. There are mainly two scenarios where voltage and power change simultaneously.

4.2.1 Load induced voltage change

First, in an industrial plant, there is intrinsic process variability that happens all through the day leading to changing load levels. The load change will result in a change in voltage because of the change in voltage drops across feeder and transformer impedances.

4.2.2 Voltage induced load change

In the second scenario, the voltage change because of tap changer variations or changes in ambient load on the feeder will cause a change in load power. Only the second scenario is useful in extracting CVR factor. The challenge lies in extracting data corresponding to the second scenario from multiple data points. Please note that the two scenarios are coupled in nature and this could lead a small error in the CVR factor measurements.

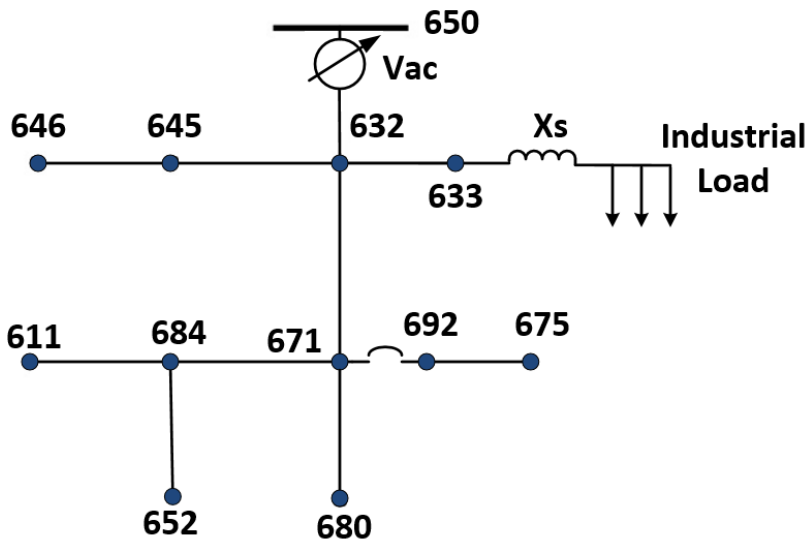

Figure 16 IEEE 13 bus system with industrial load

4.3 Characterizing Volt-power relationship

To better understand the two scenarios, explained above, detailed simulations and experiments were performed. A simulation based on an IEEE 13 bus system was modeled shown in Figure 16. The industrial load was modeled as a mix of motor loads and static loads [45]. The motor impedances are changing based on the prescribed torque speed

relationship and the behavior of industrial load is adequately modeled. In addition, an experiment was conducted on a real motor load. The objective of either of these was to convincingly differentiate load induced voltage changes and voltage induced load changes.

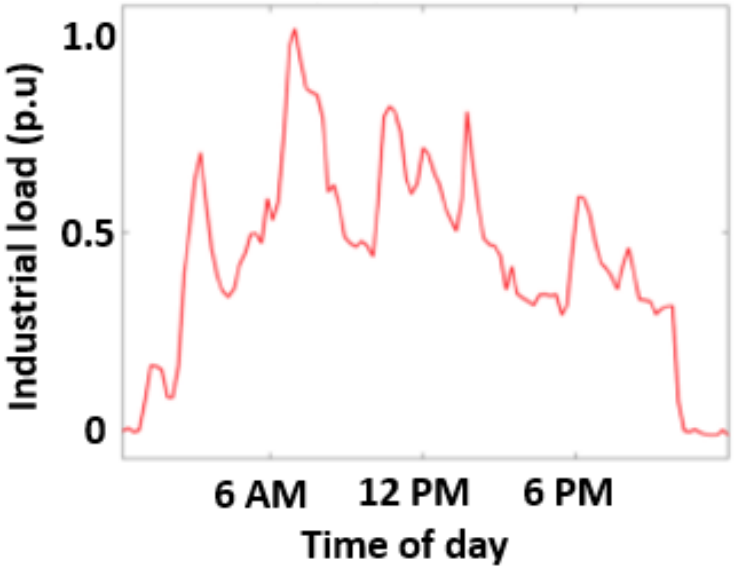

Figure 17 Prescribed profile for the industrial load

4.3.1 Simulation results

To emulate the first scenario, the voltage at the source was kept constant and the load was varied continuously for the industrial load. A stochastic load profile was modeled such that the individual loads summed up to meet the total load. At the transformer output, the ratio of changes in power versus changes in voltage were studied. The results are shown in 29 (b). The changes in voltage observed at the point of common coupling due to real changes in load on the plant side have a negative correlation.

To emulate the second case, the voltage was changed at the source with a stochastic voltage profile and the load was fixed at a variety of different conditions. Starting at 480

V that is the nominal voltage for the induction motor, the voltage was changed in 0.5 % increments and the corresponding changes in power were continuously observed at PCC. The results for this scenario are shown in 29 (a). It was interesting to observe that source led changes in power were positive in correlation.

4.3.2 'Clamp-on' voltage injection apparatus

The paper [47] has discussed an approach for estimating CVR_f at the plant level using standard power meter data. From the above simulations, it can be seen that voltage changes at the plant entrance can be due to changes in load which cause a change in voltage, or a change in line voltage that causes change in power consumption.

The former phenomenon occurs more frequently and at first glance it seems challenging to separate the two types of phenomenon. It is seen that plotting percent change in power versus percent change in voltage for all phenomenon shows opposite slopes and provides a method for discriminating between the two distinct types of phenomenon.

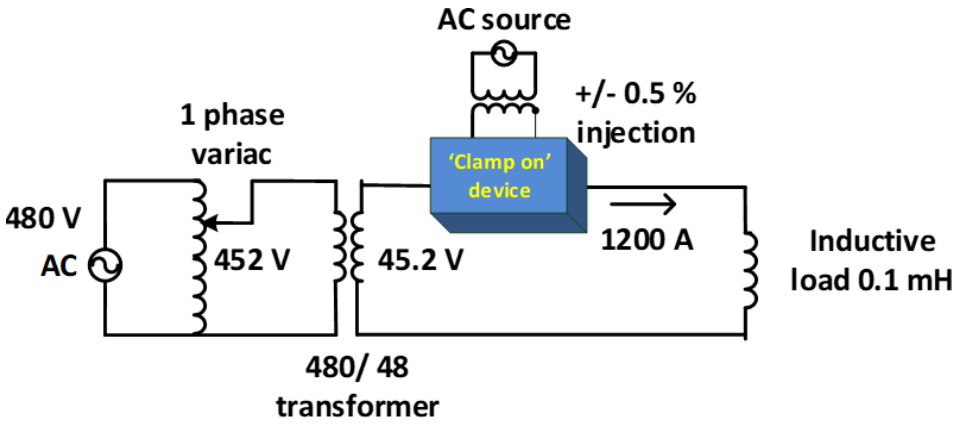

Figure 18 Schematic of 'Clamp-on' voltage injection device

To ensure that the methodology provides accurate assessment of CVR_f, a lab experiment was initiated, where CVR_f was measured for an induction machine load using a 'clamp-on voltage injection' (COVI) apparatus that was developed shown in Figure 19. Voltage could be injected into the operating machine to measure change in power, allowing an estimation of CVR_f. Similarly, load levels were changed continuously for the motor, and resulting voltage changes were measured. This allowed us to validate the discrimination methodology that was used to estimate CVR_f for the actual industrial plant.

The COVI device works by injecting a small (0.5%-1%) voltage in series with the line voltage and measuring the corresponding change in power. The major advantage of such a device is such that it can be used without distrubing the existing electrical connections. The device can be simply clamped onto the main power cable feeding the whole plant. The COVI device consists of a single turn transformer and an SCR based electronic circuit to control the voltage injection. The transformer will be using the electrical cables in the industrial plants as the single turn primary. The number of secondary turns are selected based on desired voltage injection.

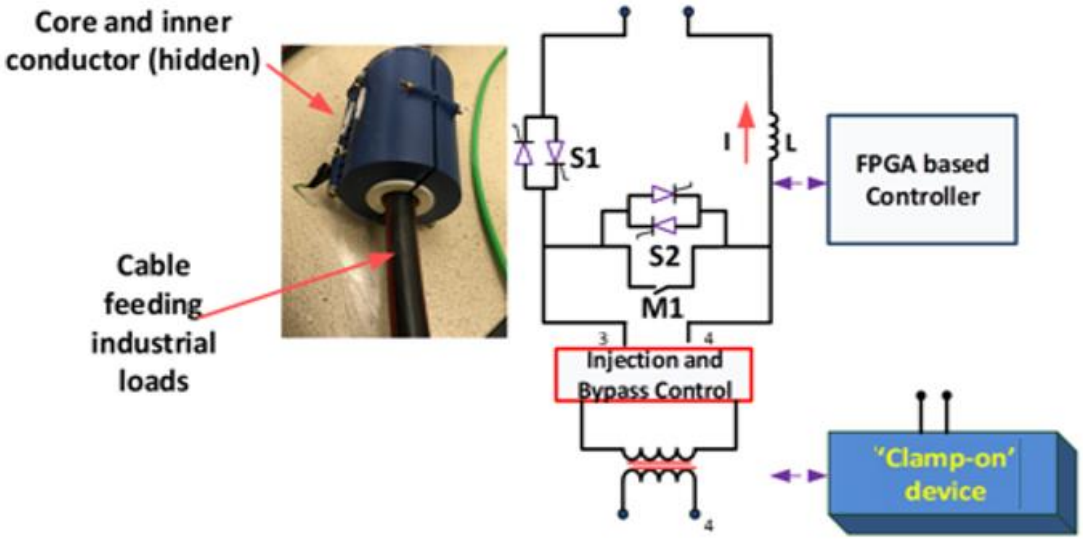

Figure 19 'Clamp-on' voltage injection device

The transformer secondary is connected to the plant voltage through a power electronic control circuit as shown in Figure 19. The power electronic control circuit will allow operating the device in the following modes: ±n % injection mode and bypass mode (0 V injection), where 'n' depends on transformer turns ratio. It consists of two AC switches, implemented using anti-parallel SCRs (S1 and S2) and one normally-closed (NC) mechnical switch (M1).

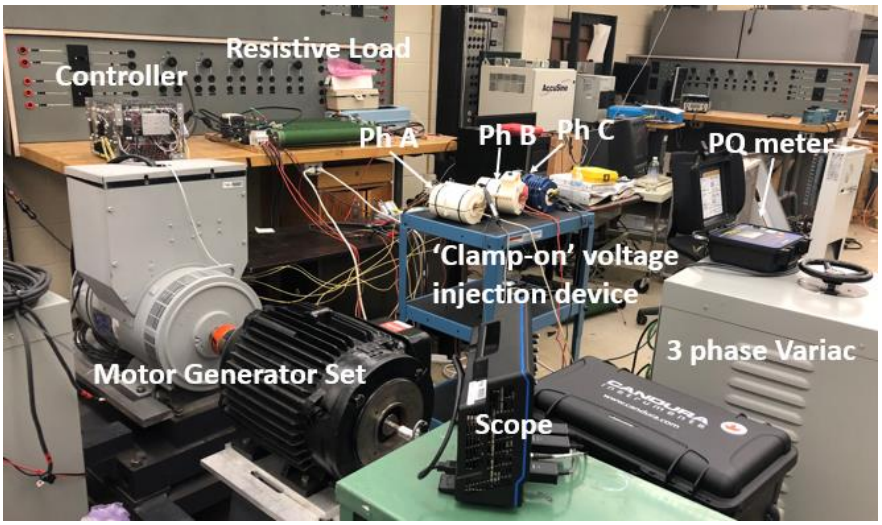

Figure 20 Photograph of test setup with 'Clamp-on' device

When voltage injection is needed, switch S_1 is turned on and switches S_2 & M_1 are kept open. For 0 V injection mode (bypass mode), switch S_1 is open and switch S_2 is closed. Switch M_1 along with switch S_2 also acts a fail-normal switch. In case of a fault on the electronic control circuit, M_1 switch goes to its natural state, which is normally-closed, to bypass the COVI device and thus not impacting the plant operations.

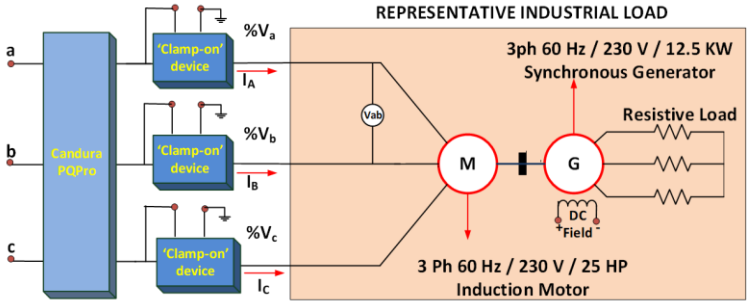

Figure 21 Schematic of test up with 'clamp-on' device

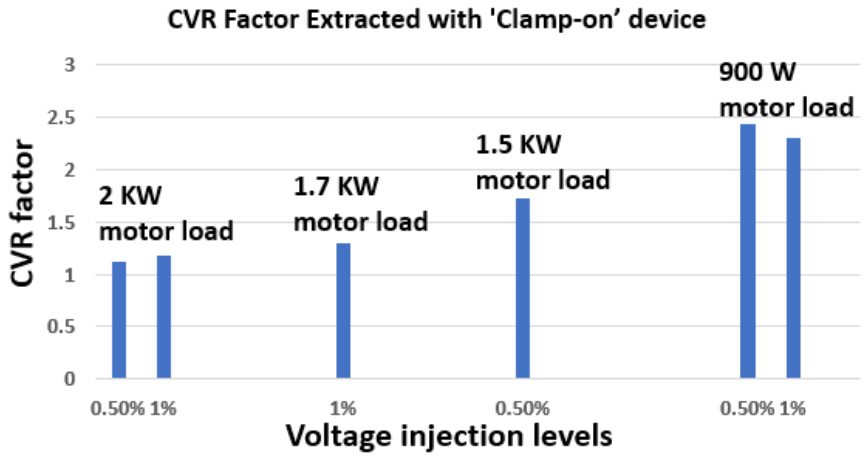

Figure 22 CVR factor extracted with 'clamp-on' device

For the clamp-on device, a pulse train would enable the device to toggle between 'inject' mode and 'bypass mode' with a set duty-cycle as well as suitable injection level and the CVR factor would be recorded using a power quality meter

4.3.3 CVR factor with 'Clamp-on' device

Figure 22 shows CVR factor of an induction motor – extracted with the device. It shows that CVR factor is higher at lightly loaded conditions and decreases as the load levels increase. The combined benefits come from reduction in power and improvement in power factor. More explanation about the test setup have been discussed in subsequent section.

Table 3 Components of 208 V 1200 V clamp on device

Item	Part no.	Ratings
Cores	Custom	ID: 5 cm, OD: 12.8 cm, Length: 17.8 cm
Turns ratio	-	1:200
Secondary winding	-	20 AWG magnet wire
SCRs (S1 and S2)	MCC56-12io1B - IXYS	60 A, latching current: 0.5 A
NC switch (M1)	T9AP5D52-24	20 A
Controller	FPGA - Altera Cyclone IV	-
Measuring device	Candura PQPro	120 – 600V, up to 3000 A

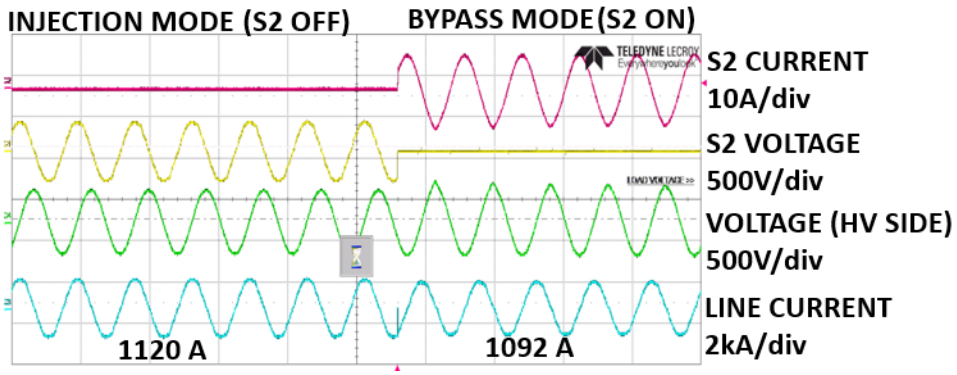

Figure 23 Experimental results with 'Clamp-on' device at 1100 A

4.4 Experimental results of COVI device operating at 1100 A

The unit was tested on a 1200 A circuit (Figure 18). A 0.5 % voltage was injected to observe the change in the current. The results at 1120 A are shown in Figure 23. These experiments have shown that the COVI prototype can be used to measure CVR factor of any plant up to 0.5 MW (208 V, 1200A)

The capability of COVI device to measure CVR factor was tested on an induction motor. The circuit schematic of test setup is shown in Figure 21. The test setup consists of

a 3-phase 230 V source feeding a motor-generator set. The generator is acting as a load for the motor and can be controlled to emulate different loading levels. The COVI device is clamped-on across the three cables feeding the motor.

The design of the 1200 A COVI device has been modified to be able to test on a 3-ph 230 V 25 HP motor. The waveforms have been shown to differentiate by-pass mode (Figure 24) and injection modes (Figure 25). The CVR factors at different loading levels and at different injections are shown in Figure 22. As discussed in the earlier sections, the CVR factor is higher (2.4 at 900 W) at lower loads than at higher loading level (1.2 at 2.0 kW).

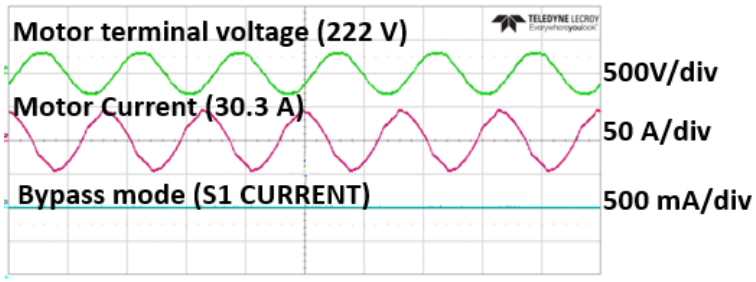

Figure 24 'Bypass mode' waveforms using 'Clamp-on' device

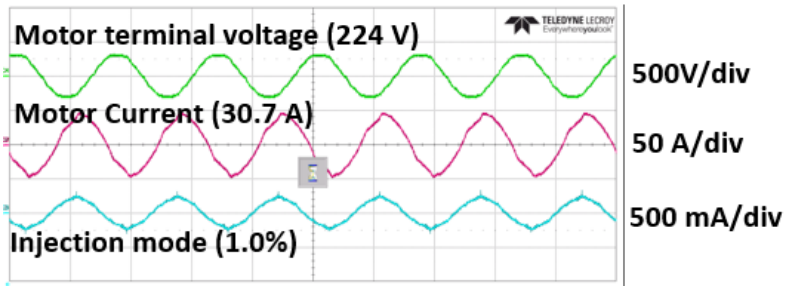

Figure 25 'Injection mode' waveform using 'Clamp-on' device

The experimental results have shown that the proposed COVI device provides a convenient way to identify CVR factor.

4.5 Data analytics method to extract CVR factor

Figure 26 shows voltage and power data from an industrial plant over 25 days. Figure 27 shows the sequence of steps leading to the calculation of CVR factor. Figure 28 shows the estimated CVR_f for the industrial plant, as it changes during the day [24]. Voltage and power measurement data that has been obtained from an actual process plant is shown. The data is measured at the point of common coupling recorded every few seconds. The plant has a nominal load of 50 kW at a nominal voltage of 600 V. All the available data is plotted in Figure 26.

Each pair of successive data points were used to calculate ΔP and ΔV. For each event, that involves two samples, the pre-event sample could be the nominal value. With this information, normalized changes in power $\Delta P\ (p.u)$ and normalized changes in voltage $\Delta V(p.u)$ are calculated. The overall trend from several hundred thousand data points seemed to have a negative correlation, which implies most of the changes are of scenario 1- load induced voltage changes. Being an industrial process plant, numerous load changes are expected. The observation made in the previous section will be used to extract CVR factor from this dataset. It is expected that the CVR factor would change throughout the day due to changing mix of loads

4.6 Estimation of CVR factor levels from field data

The following algorithm is used to determine the CVR factor:

The first step is to apply filter to obtain those successive data points where change in voltage is 0.5% or greater.

The second step in the event screening process involves isolating the changes in voltage (ΔV) caused by changes in load from the changes in power (ΔP) caused by real voltage changes. As described earlier, these useful events are seen with a mostly positive correlation between ΔP and ΔV. In other words, extract data with the following correlation (Equation 11)

$$sign(\Delta P) == sign(\Delta V) \tag{11}$$

The third step involves allocating data into hourly bins for each day of the week. It is based on the observation that for this process plant, the load at a certain hour on each day is very similar. Weekend power levels were low.

Use equation (1) to calculate CVR factor at each hour. An average of this value can be used to calculate the overall CVR factor for the plant.

The raw data is shown in Figure 27 (a). The data after applying filter in step 1 and filter in step 2 is shown in Figure 27 (b) and Figure 27 (c). The data that has been allocated into hourly bins. At certain hours of the day there were no data points and such time periods have been skipped. The CVR factor calculated based on the overall trend is 1.1. Figure 28. shows the value changes during the day.

Further analysis was done to understand the savings throughout the year based on reasonable assumptions as discussed in Table 23. The average CVR factor at each hour of the day is used to be able to understand the level of expected savings and average CVR factor in one year.

4.7 Challenges with this approach

The first challenge with this approach is to obtain data with high solution for a long period. The second challenge is that even with high-resolution data, the useful data points may be of no significant number. In the example case, out of a dataset consisting of 137,500 points, only 230 data points were found to be useful for CVR factor extraction. In addition, since the negative correlation is neglected, which has information about the relationship between load and voltage, the CVR factor calculated with this approach is slightly inaccurate

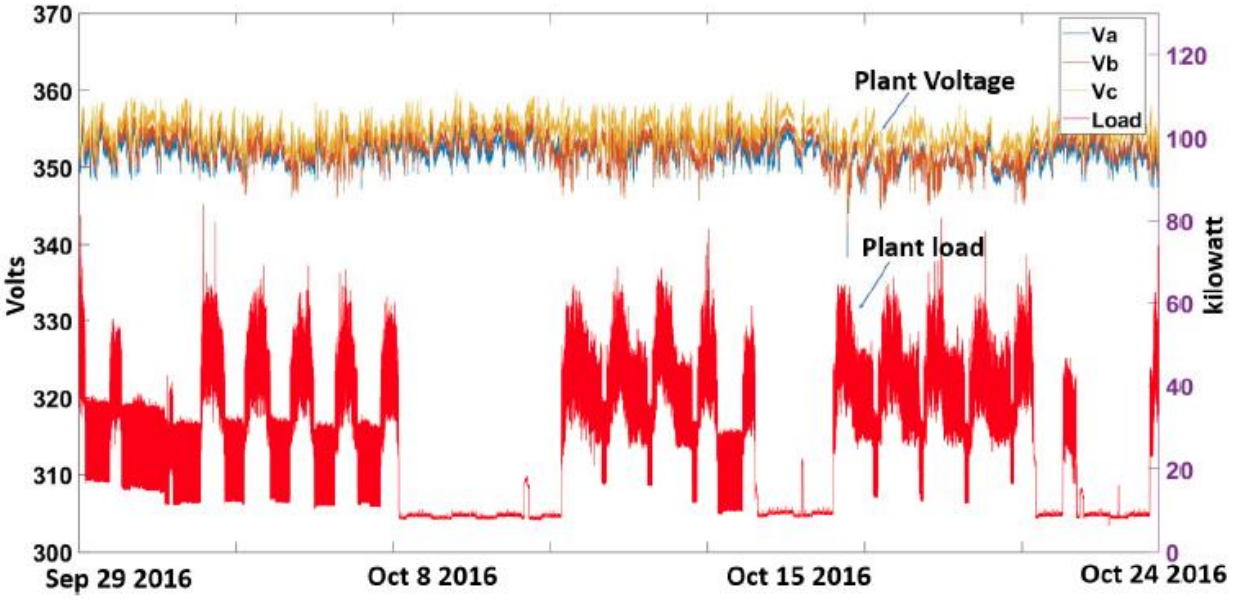

Figure 26 Industrial plant data over the period of 25 days

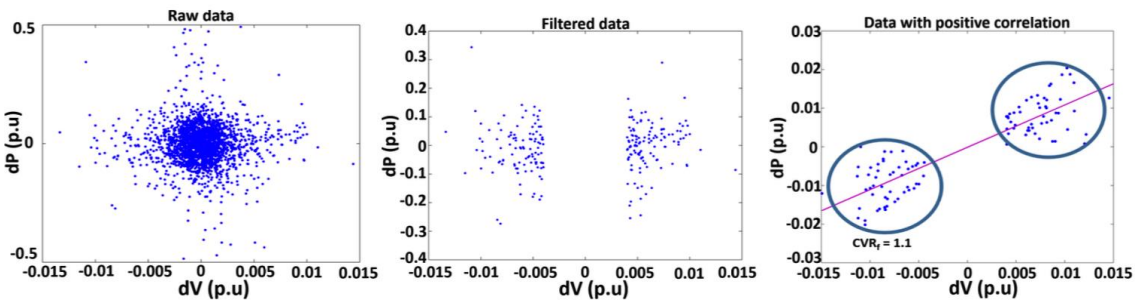

Figure 27 Sequence of steps leading to CVR factor calculation

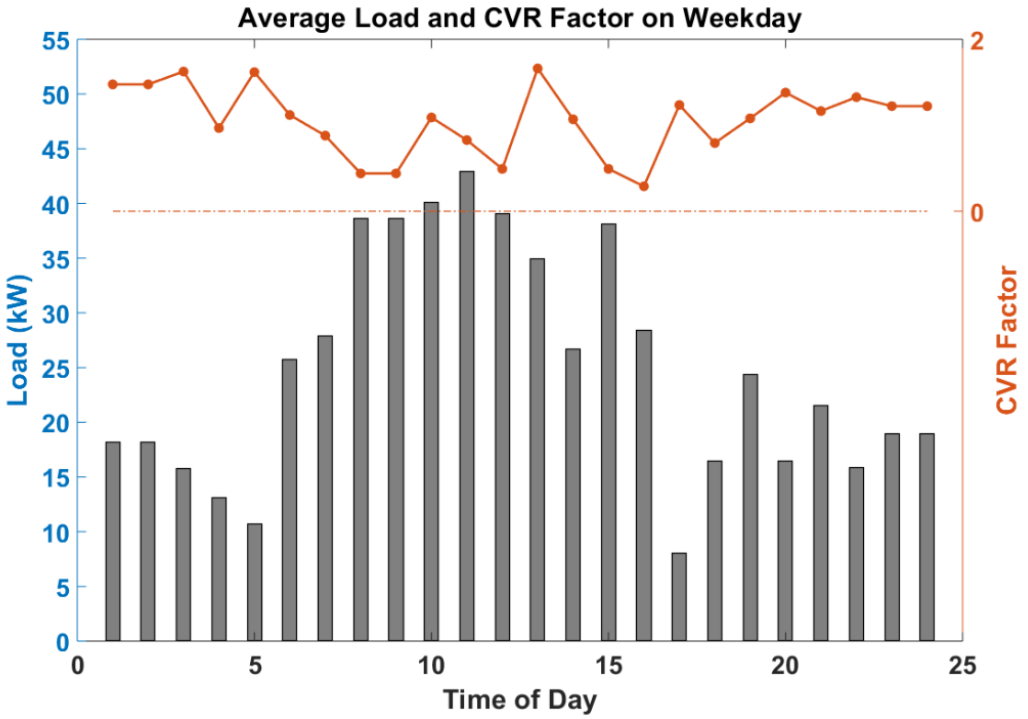

Figure 28 Hourly CVR factor

For an industrial plant, having an average CVR factor of 1.0, with a 6% voltage change, yields a 6% reduction in energy consumption. The annual savings for a 1 MW industrial plant is discussed in [47] and is promising.

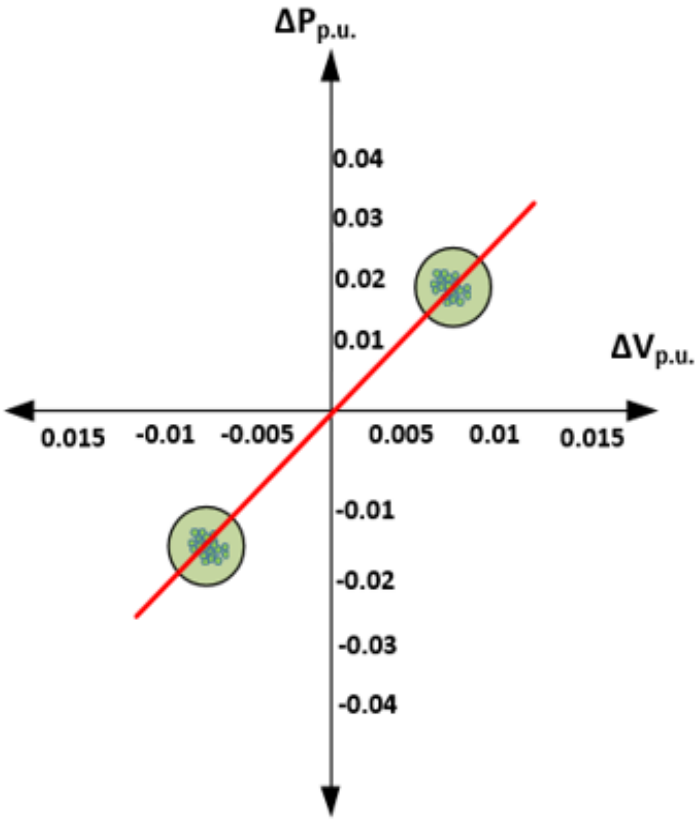
ΔP p.u.
0.04
0.03
0.02
0.01
ΔV p.u.
0.015
-0.01
-0.005
0.005
0.01
0.015
-0.01
-0.02
-0.03
-0.04

(a)

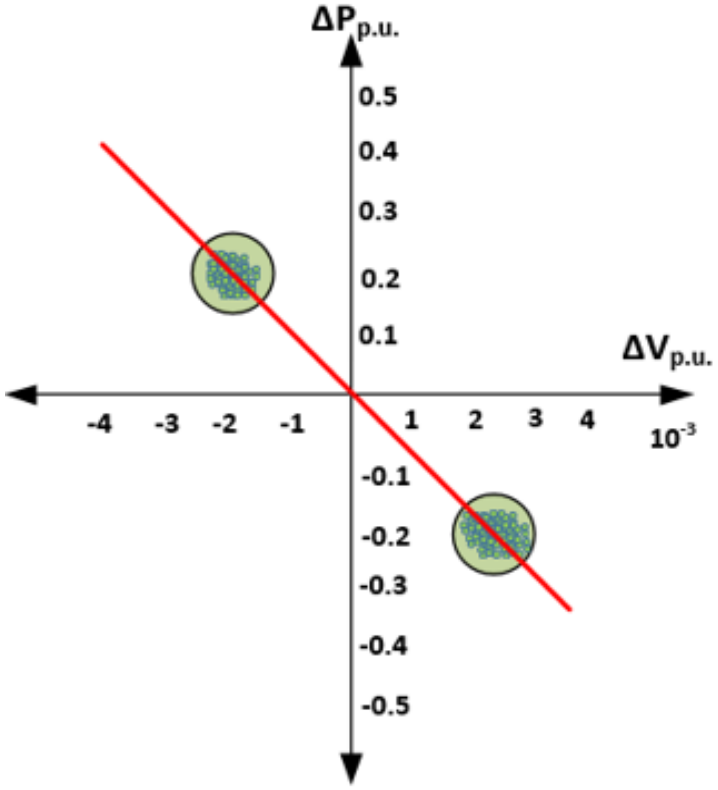

(b)

Figure 29 Correlation of voltage and power with voltage induced load change (a) and load induced voltage change (b)

Table 4 Calculation of average CVR factor

Attribute	Value
Total Demand on a weekday	597.5 kW
Total demand saved on a weekday	28.66 kW
Demand savings during 5 weekdays	143.31 kW
Demand savings in 1 year	7452.06 kW
Percentage demand saving in 1 day	4.79%
CVR Factor for a 5% voltage change	0.95

4.8 Improvement to the CVR factor extraction methodology

The average CVR factor at each hour of the day is used to be able to understand the level of expected savings, summarized based on the plant load at each hour. The data measured at the moment of voltage change is used for CVR factor calculation. In addition, we can understand standard deviation and spread to consider voltage changes and impact on CVR factor. The method does not necessitate intentional voltage reduction known as a stage tests to cause a change in power [49].

The voltage and load changes that occur naturally in the system and other external conditions are used in CVR factor calculation. The method is applied to data from an industrial plant. Results show that the CVR factor depends on the type of load and seasonal changes – for example, a higher CVR factor could be due to the predominance of heating loads in winter and a lower CVR factor could be due to the predominance of constant power loads such as LCD monitors, lighting loads such as LED, etc that may have a slightly negative or close to zero CVR factor. The voltage can be reduced by reducing bus voltage through tap changes. If bus voltage reduces, the voltage dependent component of power

also decreases. The principle of CVR is used traditionally by utilities as a means to reduce demand. Data from PNNL and other studies have reported that the average CVR factor across the country is 0.8. CVR effects depend on specific factors, including voltage dependency of customer loads.

The schematic of the industrial plant is shown in Figure 14 where measurements of voltage and power could be obtained from the customer point of common coupling. The motivation here is to understand the problem of coupling between the voltage changes and load changes and to understand if we can improve the CVR factor extraction process and accuracy. The method to estimate CVR factors using voltage and power measurement data from an industrial plant was discussed earlier. The percentages of voltage and load changes are calculated from data obtained at the point of change due to external conditions such as tap changing events.

The ratio of the voltage change percentage and load change percentage is calculated to estimate CVR factors. In addition, the distribution of CVR factor as shown in Figure 129 can be calculated to understand load variations, that are reflected in the calculation of the load change percentage to estimate CVR factors. The average of the CVR factors obtained by filtering the voltage and load changes and the estimated CVR factors are used to calculate the representative CVR factor of a plant. In industrial systems, loads are always subject to change. To quantitatively identify the effects of voltage reduction, the reduction of power with respect to voltage changes needs to be estimated. The CVR factor is defined as the percentage of load change with respect to the percentage of voltage change.

An important aspect in this regard is that the changes in load naturally occur in a plant and these are coupled with voltage changes. From the measurements of voltage and power, we are unable to tell if the changes in voltage led to changes in power or if the changes in power occurred due to changes in process in the industrial plant. The tap changing events may occur 10 times a day and "useful" or "good" data points in this regard, can be obtained corresponding to the number of tap changing events. From the dataset, we may see a voltage variation by one tap changing event of the order of 0.5%. This event screening directly influences the CVR factor estimation. One has to identify the successive data points where a change in voltage is 0.5% or greater. Each pair of successive data points are used to calculate ΔP and ΔV. For each event, that involves two samples, the pre-event sample could be the nominal value. With this information, normalized changes in power $\Delta P\ (p.u)$ and normalized changes in voltage $\Delta V(p.u)$ are calculated. Appropriate event screening is important. The CVR factor is calculated only in those valid cases, that satisfy the algorithm:

1) Due to voltage changes caused by external conditions (tap changes, external load change), voltage and load changes occur. Under normal conditions, one would expect to see a decrease in voltage leading to a decrease in power – or an increase in power due to an increase in voltage based on a reasonable assumption that the mix of loads in a plant change due to process changes. It was observed that in some cases, the direction of load change was opposite to that of voltage change and thus the calculated CVR factor (ratio of normalized changes in power and normalized changes in voltage) was negative. In those cases, it may be that the natural increase in load due to process change that has occurred is more dominant than the decrease

in load caused by a voltage reduction. So, the events are screened to account for the normalized voltage change and normalized power change that were in the same direction to calculate the CVR factor

$$\Delta V > 0, \Delta P > 0 \quad \text{or } \Delta V < 0\ , \Delta P < 0 \tag{12}$$

2) With the voltage changes of the order of 0.5% or 1%, that is called a "good" event, due to external conditions, the load changes that can occur from the measured voltage changes are limited. Hence "*a very large percentage change in power and a small percentage in voltage calculated from the measured data are excluded*." [49]

$$0.2\% < \Delta P\ \% < 2.0\% \tag{13}$$

$$\Delta V\ \% > 0.5\% \tag{14}$$

Reasonable values could be a CVR factor between [0, 2], which can be argued with the predominance of constant power loads such as a heavily loaded motor or other loads like LCD monitors, LED lamps, that could lead to lower CVR factor and with the dominance of resistive loads, we may see a higher CVR factor. This criterion is chosen based on the intuition and engineering judgment; it can be applied to different system with minor modifications.

3) The challenge with this approach is to obtain data with high resolution for a long period. The second challenge is that even with high-resolution data, the useful data

points may be of no significant number. We could fine-tune the parameters to improve the accuracy of the CVR factor estimation. For example, depending on the number of tap positions, the voltage change between successive data points, could be slightly different. The following chart shows the spread of voltage reduction from the measurement dataset.

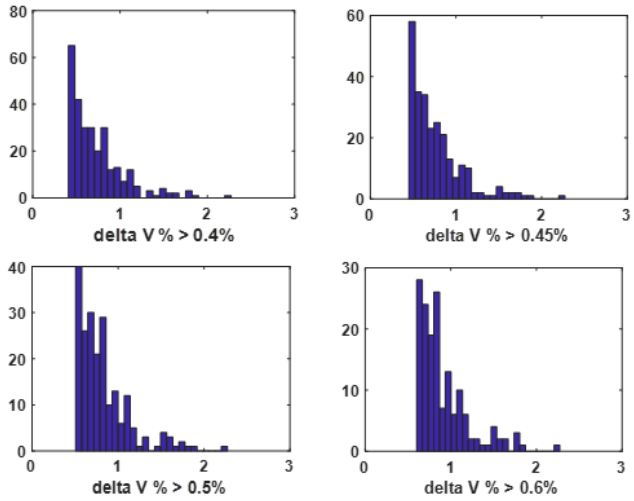

Figure 30 Distribution of voltage changes and number of data points

$$Delta\ V\ >\ 0.4\%\ -\ 283\ data\ points$$

$$Delta\ V\ >\ 0.45\ \%\ 256\ data\ points$$

$$Delta\ V\ >\ 0.5\%\ 210\ data\ points.$$

$$Delta\ V\ >\ 0.6\ \%\ 158\ data\ points.$$

This could be a means to get more data points to refine the algorithm.

4) Filtering out outliers and bad data could further improve the accuracy of the algorithm.

Translating, organizing, and filtering data is critical in the CVR factor extraction process. The data was extracted in .csv format where different useful parameters are listed

(Voltage, Current, Power etc.). The file can be accessed from within the Matlab interface. A procedure was coded to automate the CVR factor extraction by reading and storing the file in workspace. A visualization app is developed that takes a .csv or a .xls file as input and shows voltage, power (or other useful data) along with the CVR factor of the plant shown in Figure 31.

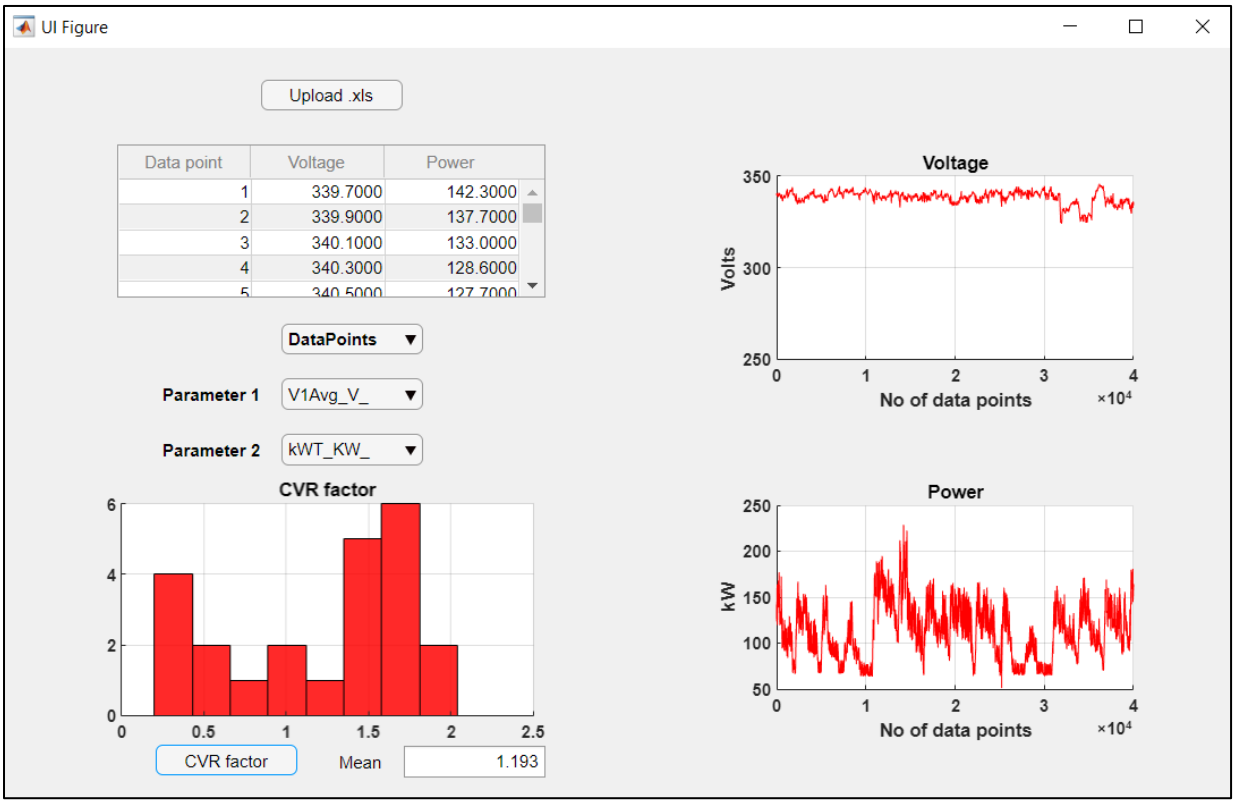

Figure 31 Visualization tool for CVR factor extraction

This paper presented methods to evaluate conservation voltage reduction (CVR) factor of an industrial plant, which can help determine the degree of energy savings that can be realized by operating the plant at lower than nominal voltages. An induction motor, the predominant load in industrial environments, is analyzed.

Subsequently, two methods are presented to determine the CVR factor of an industrial plant. It was experimentally shown that the voltage-power correlation is of opposite polarity for a load-induced voltage change and voltage-induced power change. This observation has been used to develop a data analytics technique to extract CVR factor from voltage and power data of any plant. The technique has been applied to data collected from a real process plant and it was shown that the average CVR factor is 1.1. A second method to extract CVR factor using ‘clamp-on’ voltage injection (COVI) device is also presented. It was shown that the COVI device can be simply clamped onto the main power cables of the plant and a 0.5-1% voltage can be injected to observe the power change, and hence extract the CVR factor [47].

CHAPTER 5. REQUIREMENTS OF A DEVICE FOR VOLTAGE MANAGEMENT

The results thus far lay the foundation for the proposed research discussed in this section. With the mix of loads that change throughout the day, CVR factor of an industrial plant changes. A method to extract CVR factor of a plant was discussed and the approach was validated through simulation and experiments that showed voltage changes caused by changes in load have a negative correlation and load changes caused by changes in voltage have a positive correlation.

A device for harsh industrial environments has to meet some requirements that have been discussed in this chapter. They are dynamic control – voltage sags, fail normal capability, fault current handling capability, efficiency, and thermal management.

5.1 Dynamic Control – Voltage Sags

The semiconductor industry, in standard SEMI F47, and the Information Technology Industry Council (ITIC, formerly CBEMA) [7] both recognize the susceptibility of equipment to voltage sags, and the related costs to the end-user and have published recommended input voltage magnitude/duration curves that such equipment should tolerate. Even a 250 ms voltage sag, might be able to lead to significant interruption to processes and loss of productivity. Furthermore, the current inrush caused by a voltage sag could cause damage to the equipment. In addition, significant positive and negative torque transients might potentially damage shafts in motor loads. Reducing voltage

magnitude to implement CVR may further increase the susceptibility of the plant to voltage sags exacerbating these issues.

Figure 2 shows data from 2018 systematically obtained from [7] demonstrating the preponderance of voltage sags in industrial plants recorded by over 1800 sensors in the continental United States. More than 55000 events are shown and a significant amount of them seems to violate the ITIC limits causing potential process interruptions. The device should have a dynamic capability to move from voltage reduction mode to zero-injection mode to avoid increasing the susceptibility of the plant to voltage sags. If the device can boost the voltage at the time of the sags, it would be even better. Hence, a CVR implementation device should have a dynamic response capability to achieve reduction in potential process interruption.

5.2 Fail-Normal Capability

Fail-normal capability would imply the ability of the device to isolate itself safely under fault conditions without impacting plant operations. Adding bypass and breaker on the primary side can add to the complexity of implementation. Simulation and experimental results in the subsequent section discuss fail- normal operation.

5.3 Fault Current Handling Capability

The device used to implement conservation voltage reduction may be exposed to fault current in industrial plants. The system should be robust to handle mechanical forces under fault conditions. Pure power converter-based voltage controllers or transformer-based solutions lack the capability to handle fault currents and the resulting forces. Figure

58 shows simulation results of a protection and coordination study in Easy Power software that showed a delay of 3 cycles for a breaker to operate and in this duration while the breaker clears the fault, the series-connected solution used to implement voltage control could be exposed to 17000 A of fault current in this specific case. Forces occur during the initial peak and the system must be robust to handle such forces. Conventional transformer-based systems or power converter-based systems may lack the ability to handle the forces and may have a structural impact due to fault.

5.4 Efficiency

For a device to implement conservation voltage reduction, the device losses should be extremely low, so the benefits could be fully realized. Fully rated power converter-based solutions may experience considerable amount of losses if operated continuously.

5.5 Thermal Management

The other important requirement is the management of thermal issues and to safely operate in harsh conditions. The device should have the capability to ensure excessive heat doesn't cause impact to the conductors by affecting the insulation. The subsequent sections elaborate on the CVR implementation device and experimental results that support that it meets all the important considerations discussed in this section.

The thesis discusses the use of coaxial winding transformers for managing voltage in industrial plants.

5.6 Choice of topology

The thesis proposes the use of a device with winding conductors in coaxial arrangement, with both windings surrounded by a magnetic core for voltage management in industrial plants. This is referred to as coaxial winding transformer (CWT), the distributed current on the outside conductor coaxially surrounds the current on the inside conductor [50].

The schematic of the CWT is shown in Figure 32 which has a coaxial arrangement on both outgoing and return conductors which is in form equivalent to two elongated current transformers placed side-by-side [51] [50]. The device concepts discussed here are analogous to a current transformer for instrument except the core is beyond the linear region and the power transfer level is several orders of magnitude larger [50]. Saturation could be very important as part of protection. For clarity and in light of the voltage management application which this thesis focuses on, the outer conductor is considered to be the primary winding and the inner conductor is taken as the secondary winding as labeled in Figure 32. Other applications with roles of primary and secondary reversed could be possible and illustratively either winding could be used as primary [50].

The device current is parallel with the cylindrical axis and the magnetic flux path encircles the cylindrical axis. Conversely in a solenoid the current path encircles the cylindrical axis. [50]

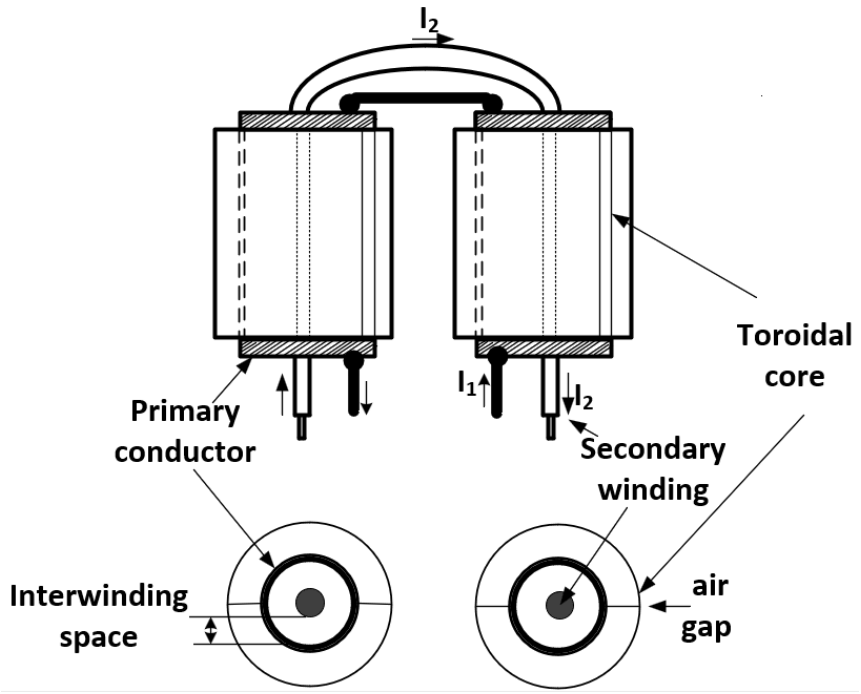

Figure 32 Schematic of a CWT [52]

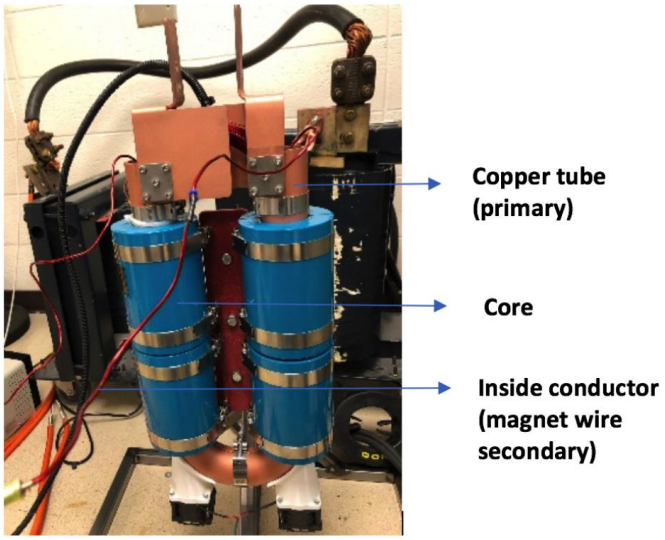

Figure 33 Photograph of lab prototype

5.7 Salient features of a CWT

The leakage field in the device does not enter the core and is well contained in the interwinding space. This is based on the ampere's law which states that the magnetic field intensity hence the magnetic flux is zero in areas enclosing the zero-net current.

*"*The *net current outside the outer of the two coaxial conductors carrying equal and opposite currents is zero so the magnetic field in that region is zero in the ideal case"[50]* The leakage field remains in the annular region between the primary and the inside conductor and within the conductor themselves and as previously mentioned, doesn't penetrate the core material. *"These features can be used advantageously and is the fundamental basis for device scalability"[50]* supporting the use in voltage management applications at high power levels without having to change the fundamental topology.

The relationship of the magnetic field path to the orientation of a cylindrical conductor, which is the primary winding of the device is important [50]. The magnetic field in a circular coaxial arrangement is parallel to the conductor surface that leads to avoiding other issues surrounding eddy current heating on conductor surface caused by a portion of the magnetic field impinging on the conductor in the direction perpendicular to the surface.

The other feature of the device is that very low leakage inductance is possible. This means very little energy is stored in the leakage magnetic field. Since the leakage magnetic field primarily exists in the gap between the primary and secondary, called the interwinding space, the length of the circular path may be designed sensibly [50].

More importantly the device has a cylindrical symmetric structure made out of copper tubes or cylinders. This simple cylindrical geometry assists with ruggedness and gives the opportunity for cooling inside the inner conductor with fans and is a shape readily with copper manufacturers as well as silicon steel toroidal cores.

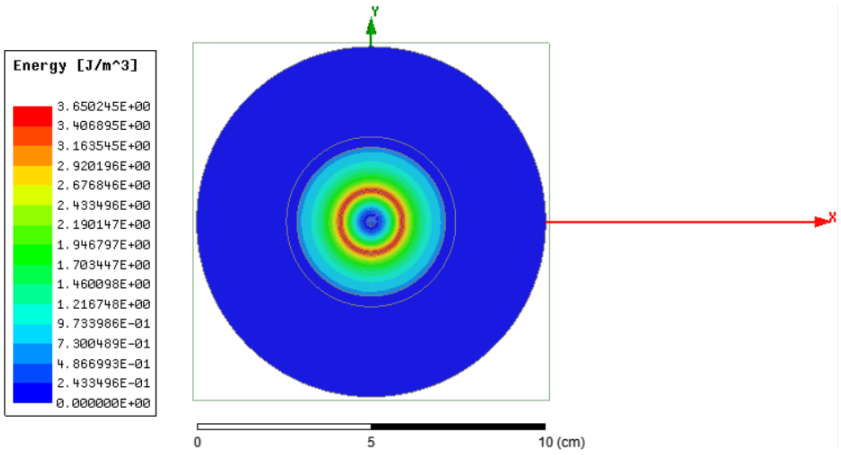

Figure 34 Simulation of leakage energy in a coaxial transformer

The ability to operate over an extended power range with a simple topology at up to 610 A without cooling and up to 2500 A continuously at 2 MW with forced air cooling is verified experimentally. This device for voltage management called SIVOM takes advantage of the inherently available interwinding space, providing for the development of a new topology and concept. The detailed results of the device built around CWT for industrial and utility applications have been elaborated, as part of which thermal characterization studies were done for both.

Results for both utility and industrial applications have been discussed. A power rating of 2 MW was chosen to match the capacity of industrial plants and the device is suitable for sustained operation. The highest rating achieved through laboratory testing and modeling was continuous operation of up to 2500 A (2 MW) and short-term overload

capability of up to 3000 A for 5 minutes for industrial applications. A prototype for utility applications at 2000 A (1.66 MVA) prototype for continuous operation was also tested to understand the feasibility of the universal wide concept of SIVOM.

Design and understanding of the 2 MW unit for voltage management in high power applications is an important objective of the research. Experimental results have been discussed to validate detailed simulation studies. Simulation and experimental data were projected and applied to the lab prototype to understand the suitability for both utility and industrial applications and predicting performance with respect to fault current, thermal behavior, simplicity of control and being able to understand robustness to harsh real-world conditions. Subsequently losses and thermal characterization studies with fans for industrial applications and oil for utility applications is discussed.

CHAPTER 6. DEVICE FOR VOLTAGE MANAGEMENT

6.1 Problem statement

There is a strong need to provide dynamic control of AC line voltage at low voltage (120-600 V) and high-power levels (1000- 5000 A) to make industrial and commercial facilities more energy efficient through conservation voltage reduction (CVR) and utilities for meshed grids improve the overall system performance by reducing losses and improve the efficiency.

In addition, low voltage high power meshed distribution networks such as Con Edison, New York known for high resiliency, suffer poor control of the network specially during system changes that lead to transformer overloads. Current solutions to these conditions, are expensive including upgrades of existing 1 MVA transformers. These hyper dense meshed grids are exposed to fault conditions of 50,000 A that lead to destructive harsh mechanical forces which the solution must withstand. The other significant challenge associated is the limited space constraint and the solution must be retrofit existing vault which is challenging. It is thus critical the solution must be unique to address all of these issues.

The concept of Stacked isolated voltage optimization module (SIVOM) introduced by Prof. Divan binds the pieces together discussed in previous sections within the theme of the thesis: which is about '*Improving energy efficiency in industrial and commercial plants through dynamic voltage management'*

6.2 SIVOM - principle

The Static Isolated Voltage Optimization Modules (SIVOM) solution consists of a number of identical voltage injection modules stacked in series to control the resulting output voltage. A circuit schematic of a SIVOM module is shown in Figure 36. It consists of a single turn coaxial winding transformer (CWT) and an SCR (silicon-controlled rectifier) based power electronics circuit to control voltage injection.

The primary of the CWT, which is single turn, is connected in series with the plant distribution. The secondary is connected to a voltage source through a SCR based circuit. CWT is selected to handle large fault currents in the range of tens of kilo Amperes. Using an enclosed geometry, shown in Figure 37, where an inner winding is contained inside a copper tube (primary winding), minimizes the leakage inductance, as well as mechanical forces on the windings when fault currents are flowing [53]. With a conventional transformer based system that typical voltage management solutions are based on, uncontrolled leakage fields can be particularly troubling and lead to excessive losses. Having both the windings with equal and opposite ampere turns, one nested within the other, in the form of natural path of the leakage field automatically precludes by ampere's law any external magnetic field [50]. Hence configuring the core material external to the coaxial conductors, eliminates the leakage field from the core material [50]. The leakage inductance of the device was characterized to be 400 nH as shown below

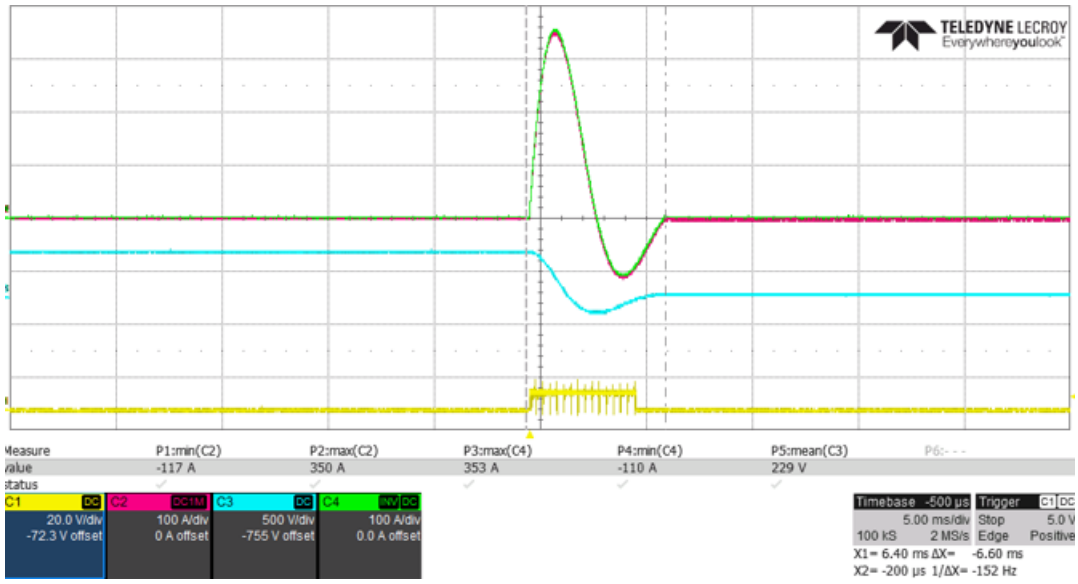

Figure 35 Extraction of leakage inductance at 17500 A

$$F = \frac{1}{2\pi\sqrt{L_{lk}C}}, \ \mathrm{T} = 6.6 \text{ ms} \tag{15}$$

$$L_{lk} = \frac{1}{(2\pi F)^2 C} : if\ T = 6.6\ ms,\ C = 1.1\ mF,\ L = 400\ nH \tag{16}$$

The SCR based circuit can inject voltage in buck mode (negative injection for CVR implementation), boost mode (positive injection for improving sag susceptibility) and fail-normal mode (0V injection). SCRs provide a sub-cycle response between various operating modes and are robust. A normally closed relay is connected to ensure fail-normal operation even with the loss of control power supply and to protect against fault currents.

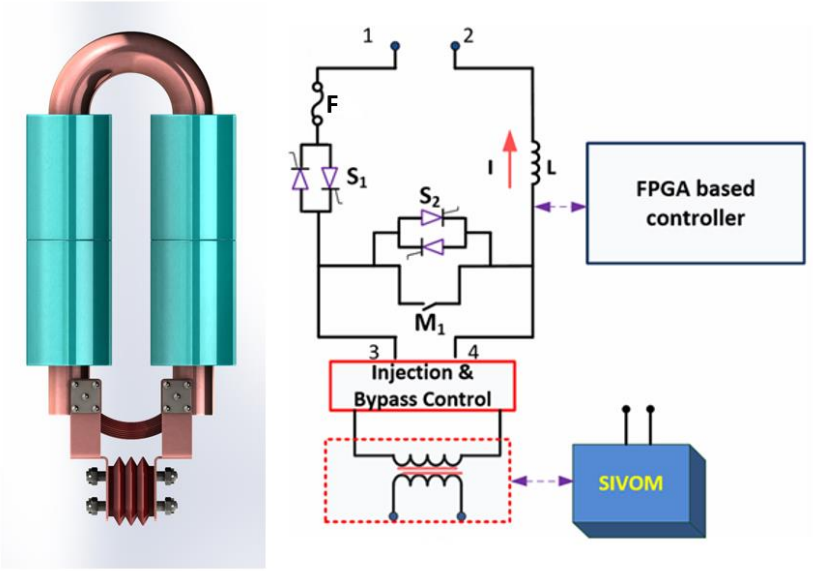

Figure 36 Single phase SIVOM unit

Each SIVOM device can be designed to provide +/- 2 % (depending on the design) injection and a multiple of these devices can be connected in series to achieve even higher voltages. The switching sequence from bypass to injection starts with turning on S2. As soon as S2 starts conducting current, M1 could be turned off. For injecting a voltage S2 is turned off and S1 is turned on depending on the polarity of voltage and current. To transition to bypass mode, S1 is turned off and S2 is turned on. As soon as S2 is turned on, the relay (M1) could be turned on.

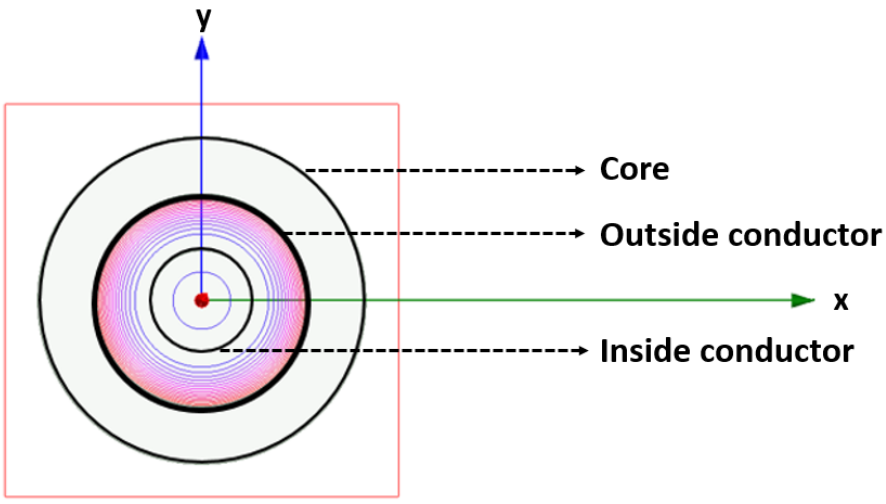

Figure 37 Flux plot of a CWT obtained when the inside and outside conductor carried current equal in magnitude and opposite in direction

6.3 SIVOM design for industrial applications (480 V/ 2500 A)

Each SIVOM module can change the voltage by around 1.5% to 2% based on the design. With three modules in series the plant voltage can be changed by about 6%. A positive injection of 6% may improve sag susceptibility by up to 80% in some plants and negative injection to reduce voltage. This could be achieved in steps as needed. Hence for the initial lab prototype a design corresponding to 2% injection was chosen. A multiple of these can be used to achieve higher voltages.

To achieve 2% injection, the module needs to be designed with 1:50 turns. The inside conductor, which is considered to be the secondary winding, has 50 turns and is connected to the plant voltage (277 V (L-N)). The primary winding, which is a single turn copper tube, needs to handle 2500 A. The design of the core is first discussed.

The relation between primary voltage RMS and peak flux density is given by

$$V_{rms} = 4K_w N f B_m A_c \ (V) \tag{17}$$

where A_c is the core flux area cross section (m^2), B_m is the peak flux density (T), f is the excitation frequency (Hz), N is the number of turns on the primary, K_w = 1.11 for sinusoidal voltage

$$A_c = \frac{V_{rms}}{4.44 N f B_m} = \frac{5.54}{4.44 * 60 * 1.3} = 0.01599\ m^2 \tag{18}$$

Knowing A_c, the length of the core is calculated as [51]

$$l_{core} = \ 0.62\ m \tag{19}$$

l_{core} is the length of the core. The selected core has a peak flux density of 1.3 T. The core volume was calculated to be 3987.15 cm^3 and the weight of the core material was calculated to be 30.9 kg. The core has a height of 15.5 cm– two of these on each side are used. The selected core has an outer diameter of 10.47 cm and an inner diameter of 5.38 cm.

The current density of the copper tube (copper 101 alloy) was chosen to be $250 \frac{A}{cm^2}$. The copper tube cross-sectional area can be computed as

$$A_{tube} = \frac{I_p}{J_p}\ cm^2 = \frac{2500}{250} = 10\ cm^2 \tag{20}$$

The outer diameter of the copper tube is limited by the inner diameter of the selected core. With the cross-sectional area and the outer diameter known, the thickness of the

copper tube can be chosen. The resistivity of the copper 101 alloy is $0.0171 * 10^{-6} \Omega m$. For the copper tube, the length was calculated to be 100 cm. The inner radius of the copper tube should be sufficient to fit over 50 turns of the inside conductor. The inside conductor chosen is a 10 AWG wire and has an area of $5.26\, mm^2$. The resistivity of the inside conductor is $2\, \frac{m\Omega}{m}$. The converter employs SCRs rated at 60 A and 1200 V. SCRs have been chosen as they are robust. The secondary winding of the device is connected to the plant voltage through the control circuit. A normally closed relay (M1) is connected in parallel with the thyristor S2. In the event of a fault in the device, M1 goes to its natural state (normally closed) – thereby safely isolating the device without impacting plant operations. A fuse is connected for additional protection.

6.4 **Switching sequence for control**

The state machine block is a powerful tool to control and model a system behavior. The simulation of the control used in SIVOM device was performed in Plecs software using the voltage and current sensor readings as input and obtain control commands and next states as output using state machine block.

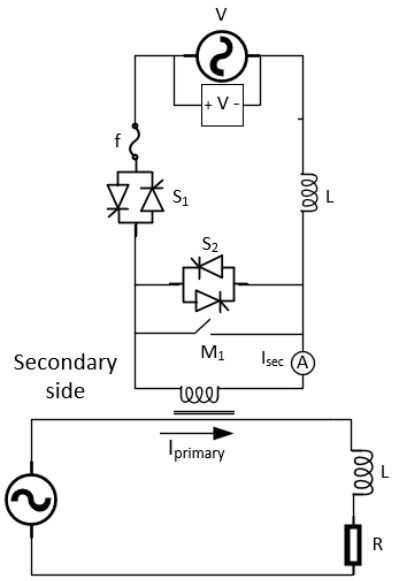

Figure 38 Schematic of the SIVOM control used in simulation

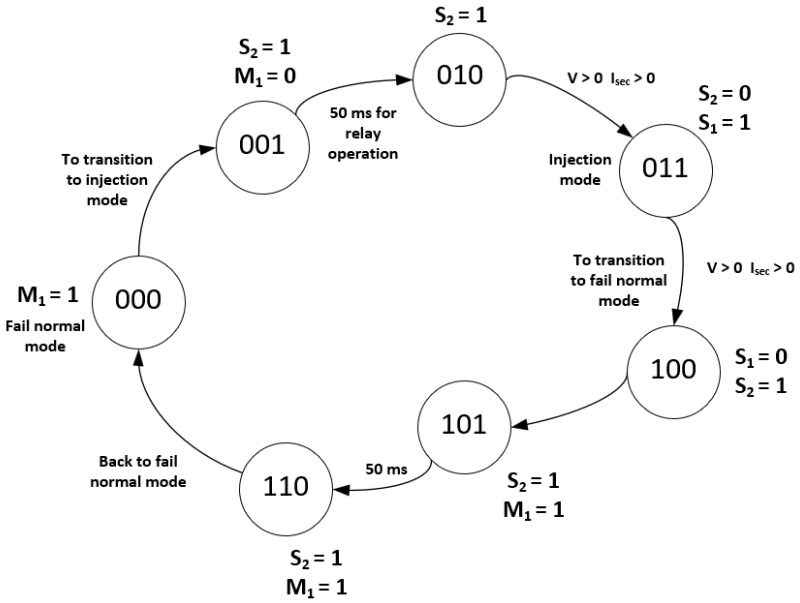

Figure 39 State machine showing the transition between injection and bypass mode

This switching sequence has been used to verify the operation through simulation and experiments.

6.5 Simulation results

For simulation, a few different cases have been shown. For the first case, the load on primary side was R = 0.04 ohm L = 0.1 mH, the current on the primary side was initially set at 364 A.

- Vsec = 100 V (-2 V injected on the primary side) at 364 A

The voltage on the secondary side was set at 100 V and this corresponds to -2 V injection on the primary side with 50 turns (2%) on the secondary winding. A change in current from 364 A to 327 A was observed for -2 V injection.

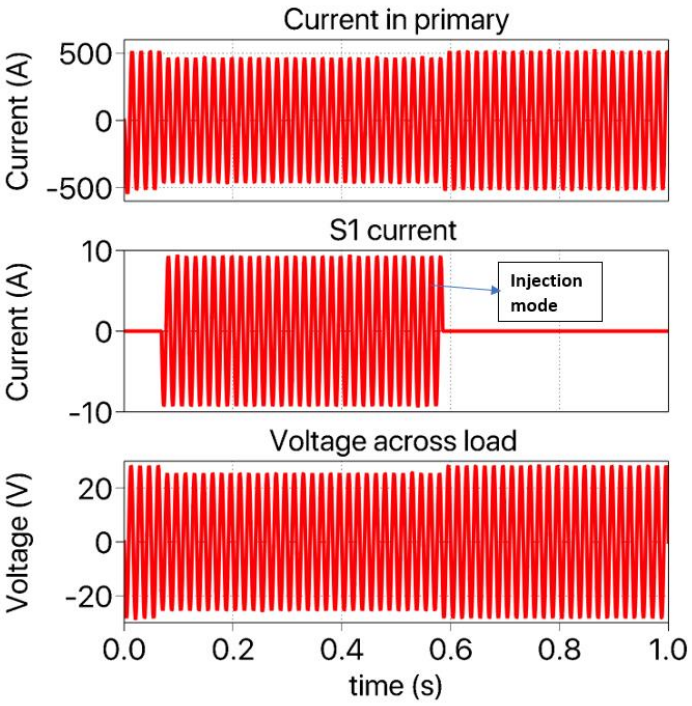

Figure 40 Simulation results at 364 A for -2 V injection

- Vsec = 150V (-3 V injected on the primary side) at 364 A

The voltage on the secondary side was set at 150 V and this corresponds to 3 V injection on the primary side with 50 turns (2%) on the secondary winding. A change in current from 364 A to 309 A was observed for -3 V injection

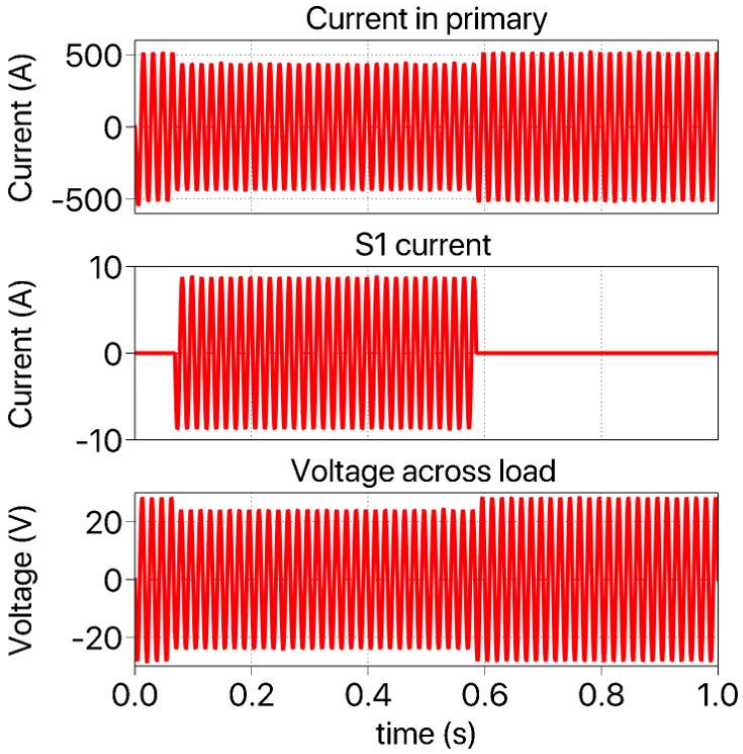

Figure 41 Simulation results with 364 A for -3 V injection

- Vsec = 200 V (-4 V injected on the primary side) at 364 A

The voltage on the secondary side was set at 200 V and this corresponds to 4 V injection on the primary side with 50 turns (2%) on the secondary winding. A change in current from 364 A to 291 A was observed for -4 V injection.

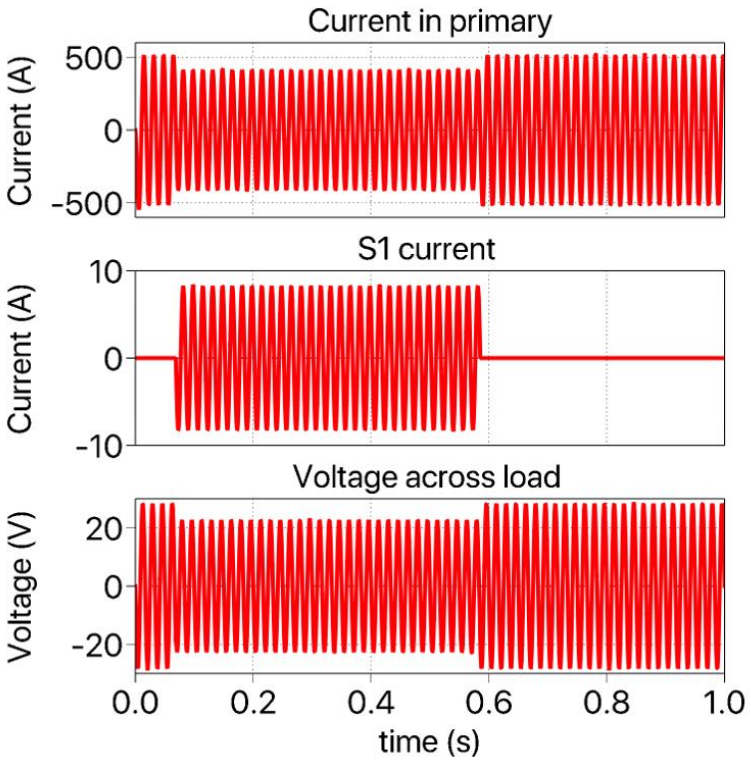

Figure 42 Simulation results with 364 A for -4 V injection

For the second scenario, the load on primary side was R = 0.04 ohm L = 0.1 mH, the load current on the primary side was increased to 546 A and the simulations were repeated for different injection levels.

- Vsec = 100 V (-2 V injected on the primary side) at 546 A

The voltage on the secondary side was set at 100 V and this corresponds to 2 V injection on the primary side with 50 turns (2%) on the secondary winding. A change in current from 546 A to 509 A was observed.

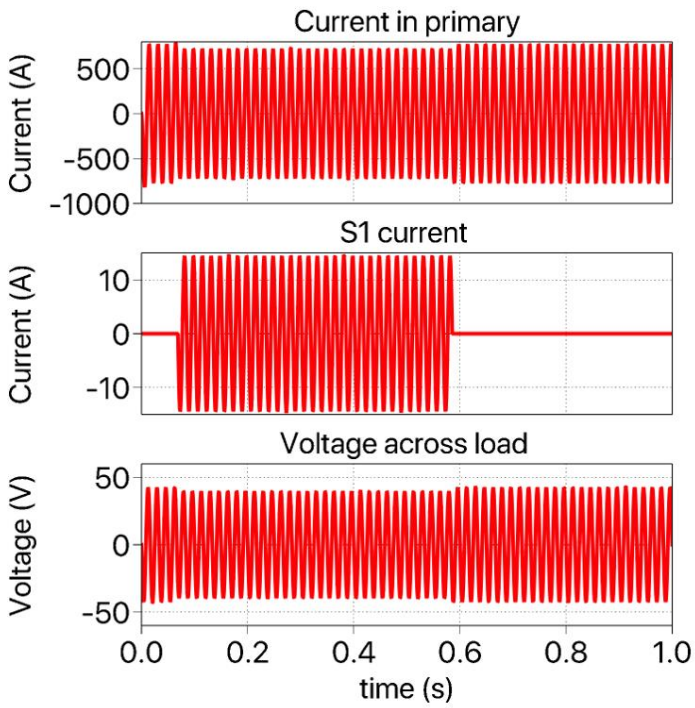

Figure 43 Simulation results at 546 A for -2 V injection

- Vsec = 150 V (-3 V injected on the primary side) at 546 A

The voltage on the secondary side was set at 150 V and this corresponds to 3 V injection on the primary side with 50 turns (2%) on the secondary winding. A change in current from 546 A to 491.2 A was observed

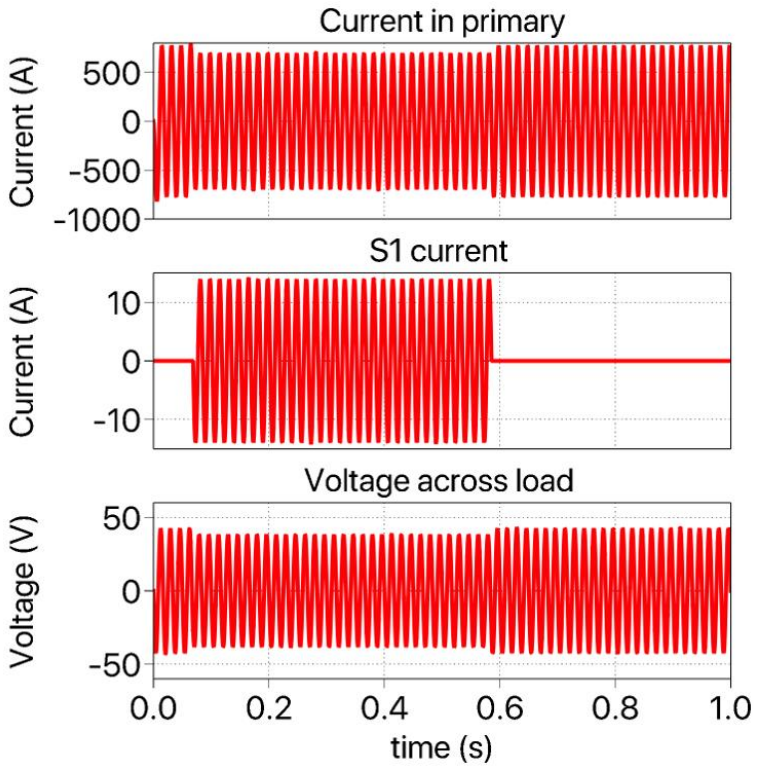

Figure 44 Simulation results at 546 A for -3 V injection

- Vsec = 250 V (-5 V injected on the primary side) at 546 A

The voltage on the secondary side was set at 250 V and this corresponds to 5 V injection on the primary side with 50 turns (2%) on the secondary winding. A change in current from 546 A to 454.2 A was observed

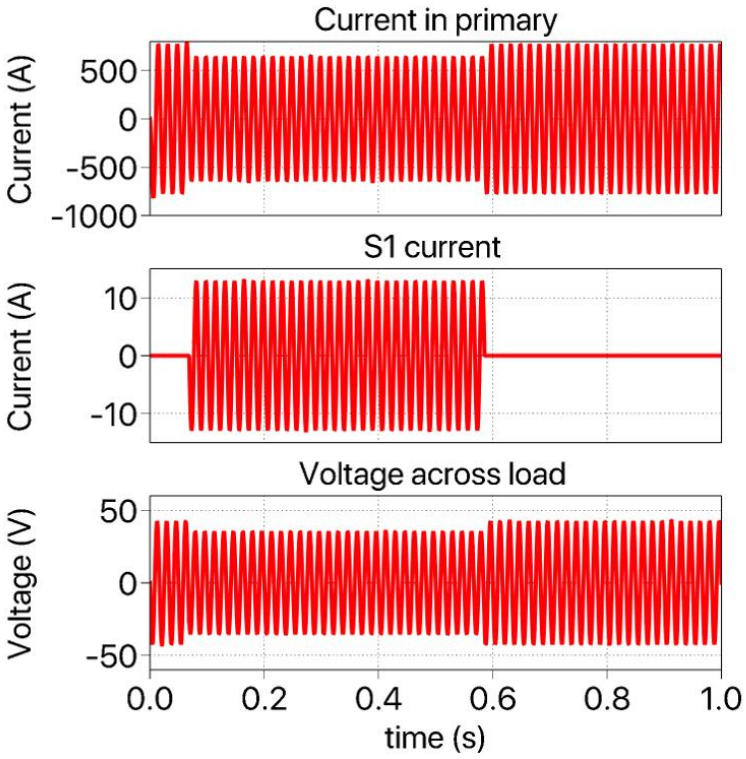

Figure 45 Simulation results at 546 A for -5 V injection

For the third scenario, the load combination was changed by changing the resistor from 0.02 ohm to 0.04 ohm in steps of 0.005 ohm, and the inductor was fixed at 0.1 mH.

- Vsec = 200 V (-5 V injected on the primary side) at 702 A

For this scenario, the resistance was set at 0.02 Ohm and inductance was set at 0.1 mH. A change in current from 702.5 A to 608.9 A was observed with the voltage on secondary side at 200 V (-4 injected on the primary side)

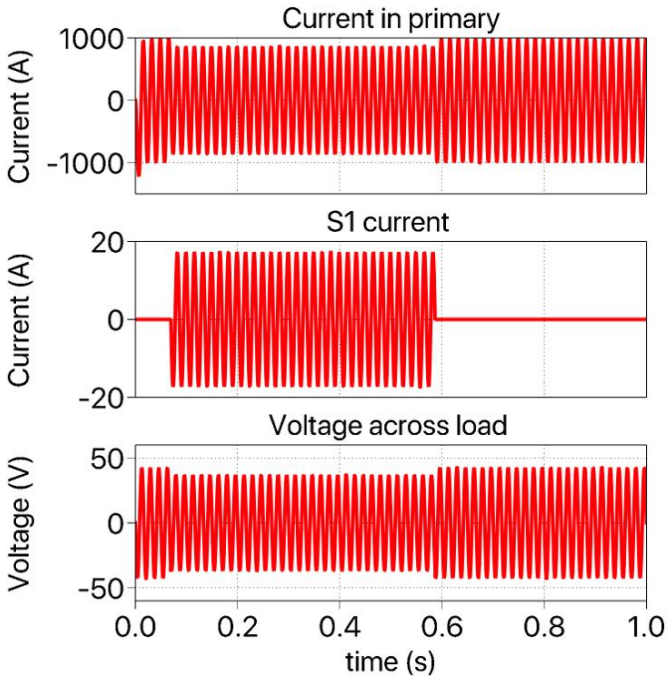

Figure 46 Simulation results at 702 A for -4 V injection

- Vsec = 200 V (-4 V injected on the primary side) at 662.9 A

For this scenario, the resistance was set at 0.025 Ohm and inductance was set at 0.1 mH. A change in current from 662. 9 A to 574 was observed with the voltage on secondary side was 200 V (-4 injected on the primary side)

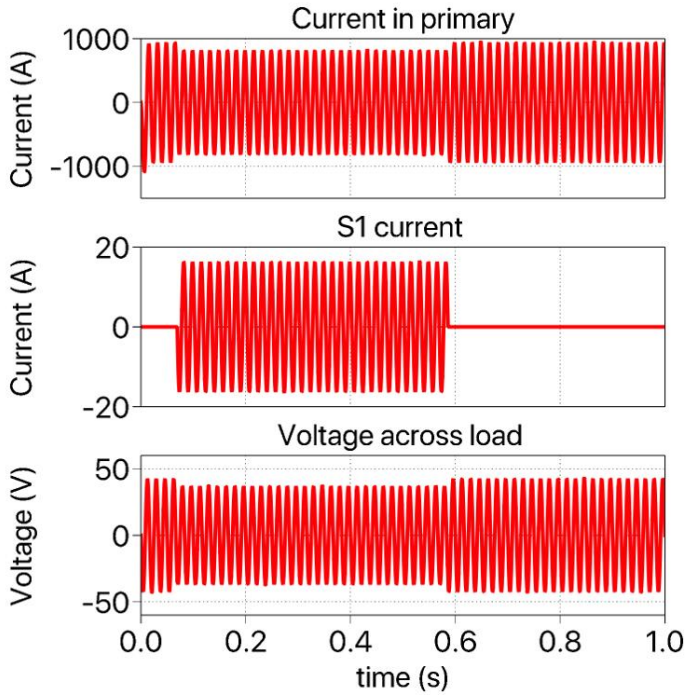

Figure 47 Simulation results at 662. 9 A for -4 V injection

- Vsec = 200 V (-4 V injected on the primary side) at 622.55 A

For this scenario, the resistance was set at 0.03 Ohm and inductance was set at 0.1 mH. A change in current from 622.55 A to 539.5 A was observed with the voltage on secondary side was 200 V (-4 injected on the primary side)

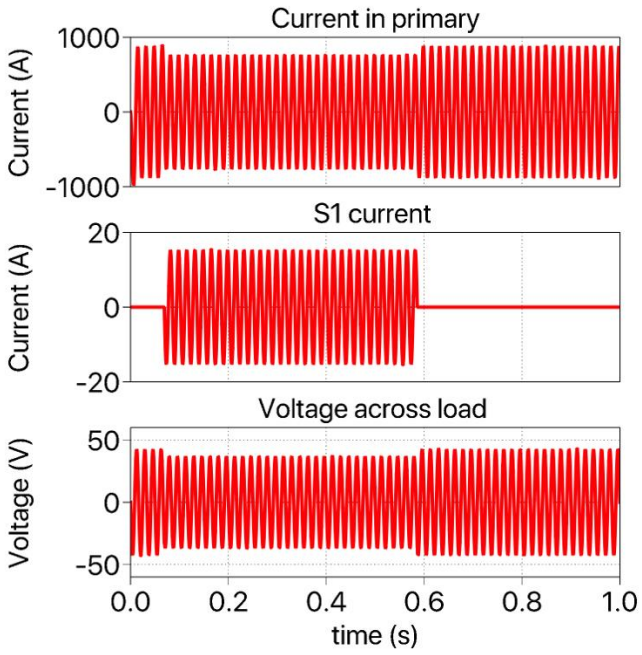

Figure 48 Simulation results at 622.55 A for -4 V injection

- Vsec = 200 V (-4 V injected on the primary side) at 583 A

For this scenario, the resistance was set at 0.035 Ohm and inductance was set at 0.1 mH. A change in current from 583 A to 505.2 A was observed with the voltage on secondary side was 200 V (-4 injected on the primary side)

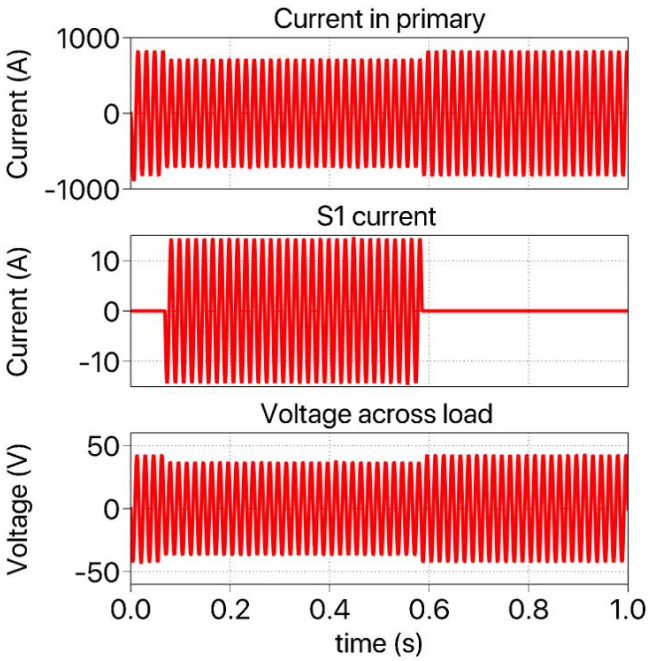

Figure 49 Simulation results at 583 A for -4 V injection

- Vsec = 200 V (-4 V injected on the primary side) at 546 A

For this scenario, the resistance was set at 0.04 Ohm and inductance was set at 0.1 mH. A change in current from 546 A to 472.96 A was observed with the voltage on secondary side was 200 V (-4 injected on the primary side)

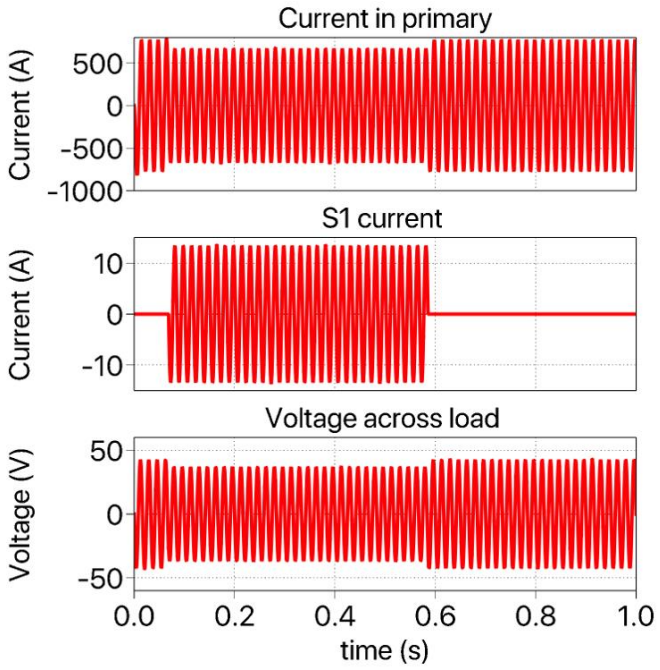

Figure 50 Simulation results at 546 A for -4 V injection

For the scenario 4, the resistive load was fixed at 0.04 ohm and the inductive load was changed in small steps.

- Vsec = 200 V (-4 V injected on the primary side) at 545 A

For this scenario, the resistance was set at 0.04 Ohm and inductance was set at 0.1 mH. A change in current from 545 A to 472 A was observed with the voltage on secondary side was 200 V (-4 injected on the primary side)

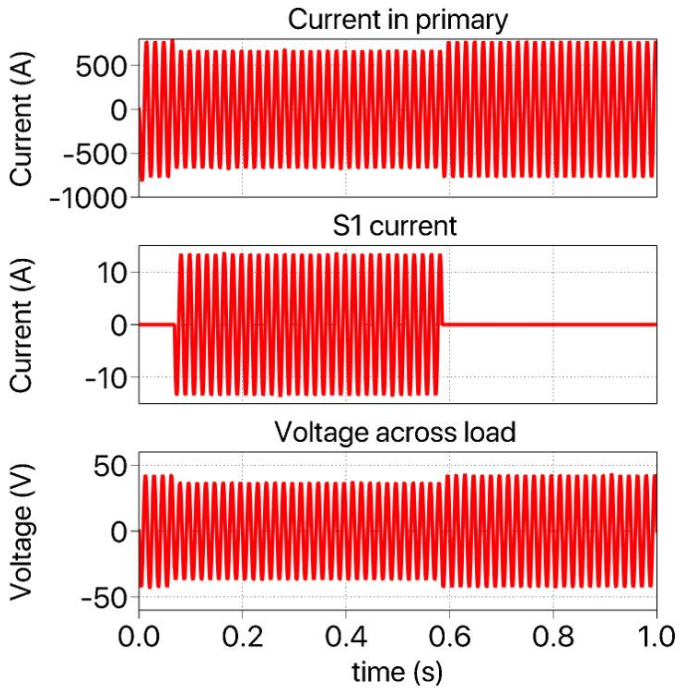

Figure 51 Simulation results at 545 A for -4 V injection

- Vsec = 200 V (-4 V injected on the primary side) at 351.3 A

For this scenario, the resistance was set at 0.04 Ohm and inductance was set at 0.2 mH. A change in current from 351.3 A to 304 A was observed with the voltage on secondary side was 200 V (-4 injected on the primary side)

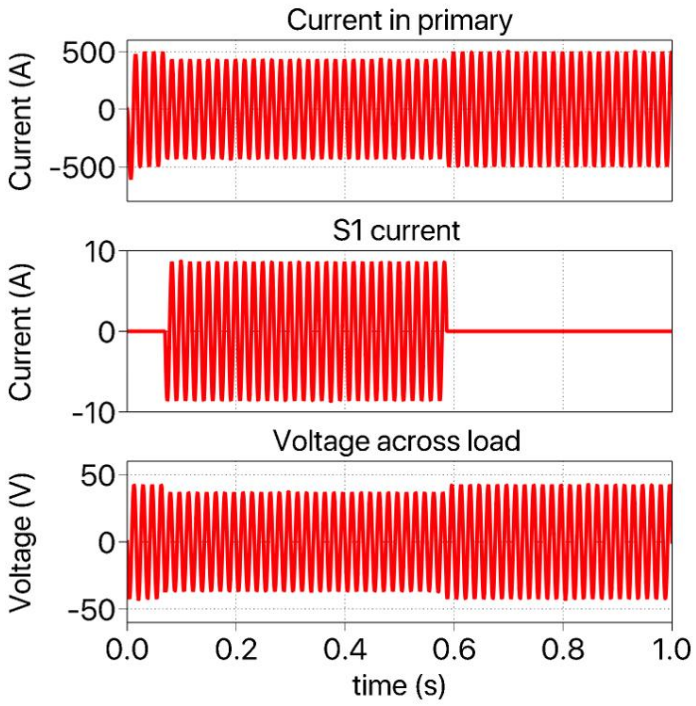

Figure 52 Simulation results at 351.3 A for -4 V injection

- Vsec = 200 V (-4 V injected on the primary side) at 432.98 A

For this scenario, the resistance was set at 0.04 Ohm and inductance was set at 0.15 mH. A change in current from 432.98 A to 375.4 A was observed with the voltage on secondary side was 200 V (-4 injected on the primary side)

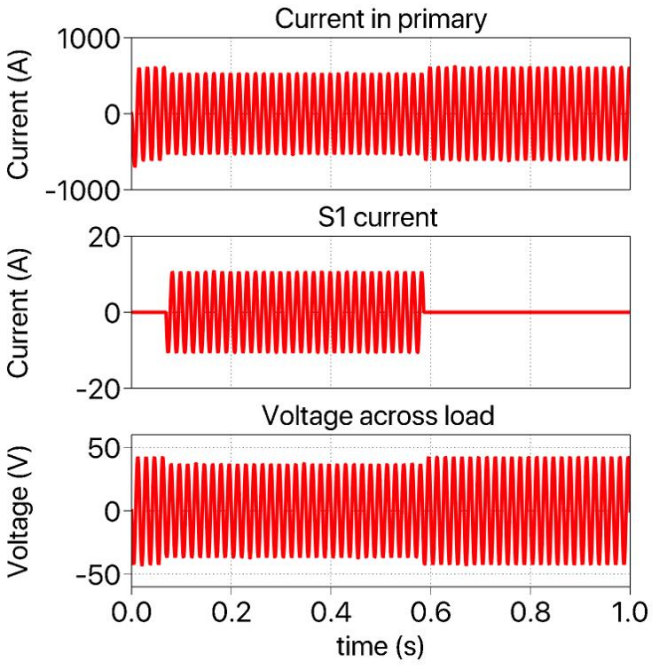

Figure 53 Simulation results at 432.98 A for -4 V injection

6.6 Bypass arrangement under Reverse power flow and abnormal conditions

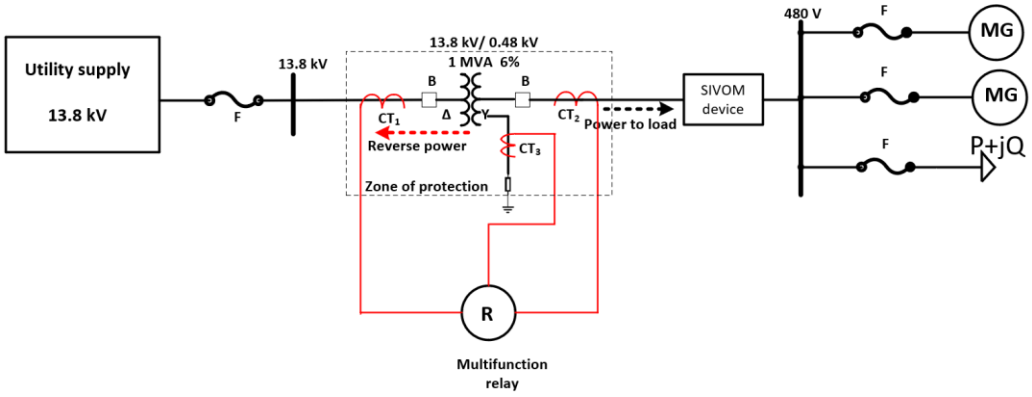

Figure 54 Multifunction relays in a power system

A multifunction relay is shown in Figure 54 that may have a combination of protective functions. A differential element (87T Transformer differential) works by the sum of currents going out of a transformer compared with the current going into the

transformer and a safe condition is when the differential is zero in the zone of protection. In the event of an abnormality, the differential relay is activated to send a trip signal to the upstream breaker. A directional power element (ANSI device no. 32) in a relay is used in combination for protective purposes. It is used to detect if there is an abnormality in the power direction.

A reverse power relay is typically used with regenerative loads. In the event of an abnormality, the generator may begin to function as a motor, and this could cause damage to the prime mover. Since these are long lead items, regenerative loads are typically provided with necessary protective mechanism. A directional element in a multifunction relay serves to trip the breaker to prevent reverse power.

The SIVOM device has injection mode and fail normal modes of operation. In the event of a fault or other abnormality in a system, the fail normal bypass arrangement in the device through the use of normally closed relays on the secondary side may be used to ensure the device shall safely isolate itself without causing impact to plant operation.

6.7 Functional Test results at different current levels

The switching sequence shown in the previous section is implemented in an FPGA and the device performance was experimentally verified. The ability of the device to inject or bypass a voltage has been performed in controlled lab conditions. The test setup consists of a system with a voltage source connected to a single phase variac, a step-down transformer (480V/48V), a load to demonstrate the change in current caused by change in voltage. The device was tested across different current levels and test results at 1000 A

have been shown in Figure 55. Results showed that the current changes from 1000 A to 970 A due to voltage change for a -1 V injection

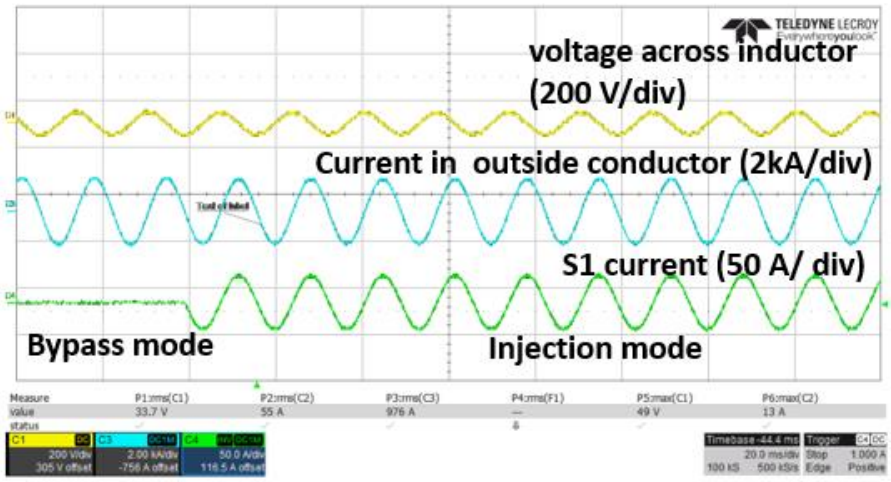

Figure 55 Experimental results of functionality

6.8 Dynamic Response Capability

As previously mentioned, sag susceptibility is the major reason for industrial plants to be hesitant to implement conservation voltage reduction. The typical approach to implement conservation voltage reduction seems to be based on three-phase transformers [54, 55]. The use of electromechanical tap changers to provide fixed voltage reduction may expose the system to lower voltages in the event of a voltage sag. Experimental results to understand the dynamic response in Figure 56, show that a change in voltage of 2.8 V to transition from zero voltage injection mode to voltage boost mode can be achieved with a response time of less than one cycle. Similar response can be achieved for the transition from voltage reduction mode to fail-normal mode. For the device to transition from voltage

reduction mode to voltage boost mode, it would go through the fail-normal mode, which may be achieved with a response time of less than 50 ms.

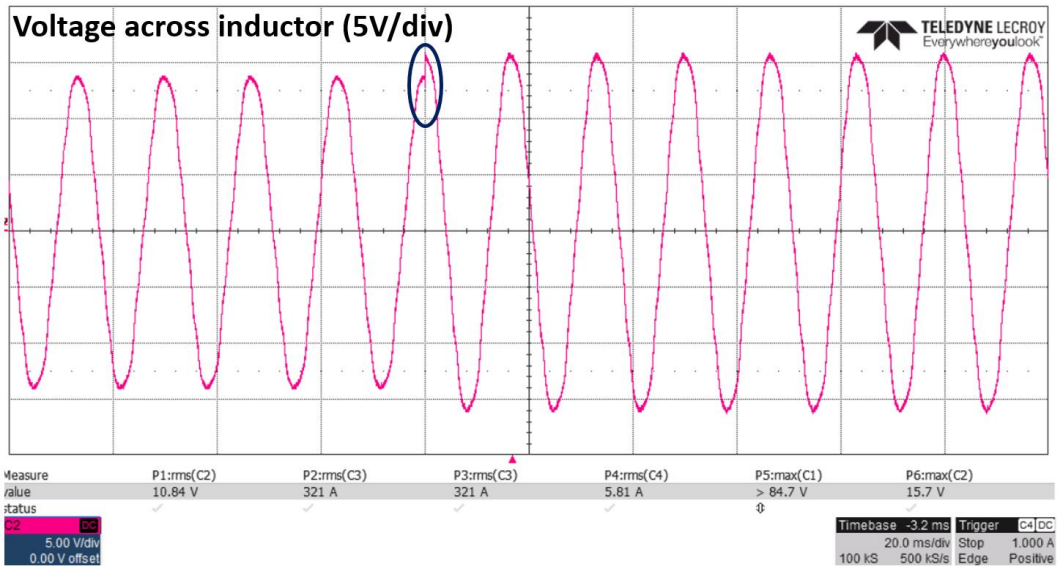

Figure 56 Voltage across inductive load showing change in voltage

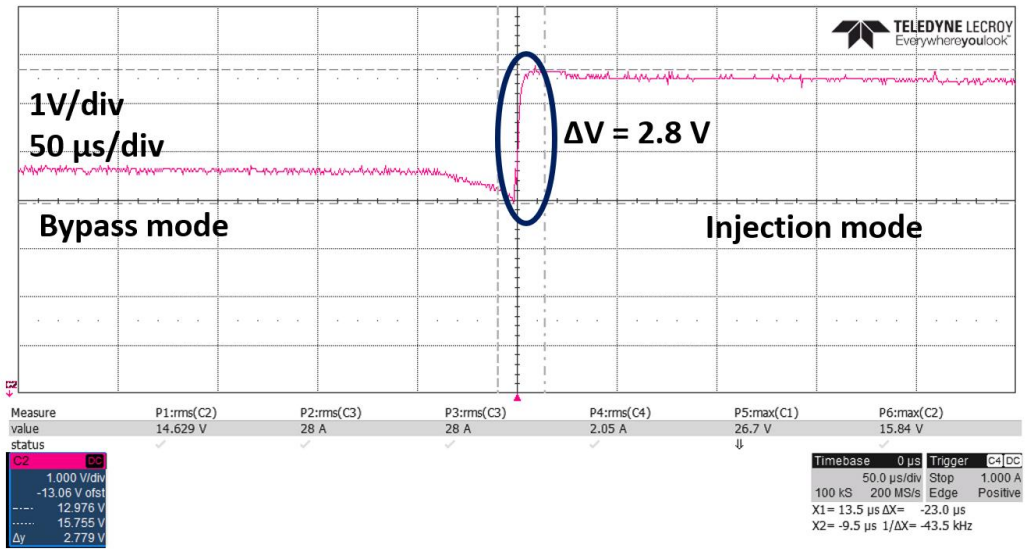

Figure 57 Voltage across inductor zoomed in to understand dynamic response

6.9 Fault current handling capability

Fault current protection and coordination is another important requirement for a device used to implement behind-the-meter conservation voltage reduction. A protection and coordination study was done to understand the delay while coordination occurs between upstream and downstream devices in a system discussed in Figure 58. The study suggested that the breaker closest to the fault might trip in 3 cycles and during this time interval, the device may be exposed to high current magnitudes. Forces occur during the initial peak. In the event of a fault, the device should be able to withstand the harsh mechanical forces.

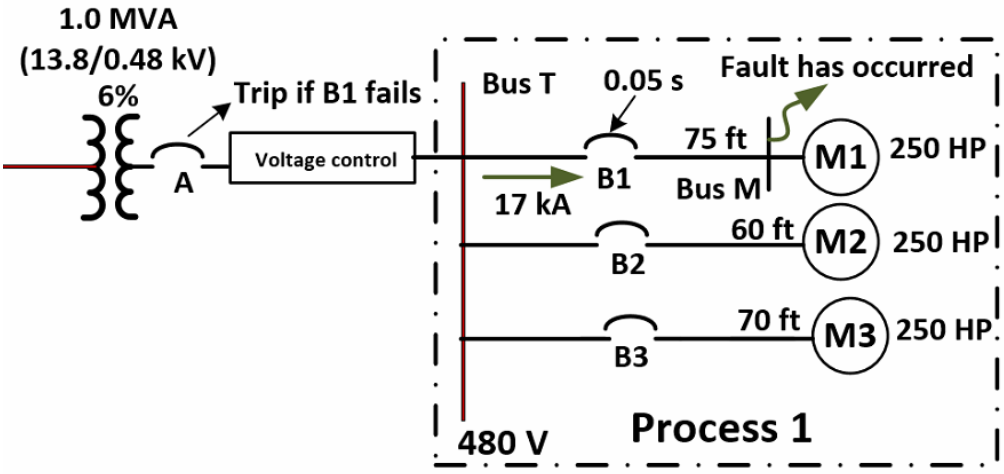

Figure 58 Protection and coordination study showing a fault at a bus

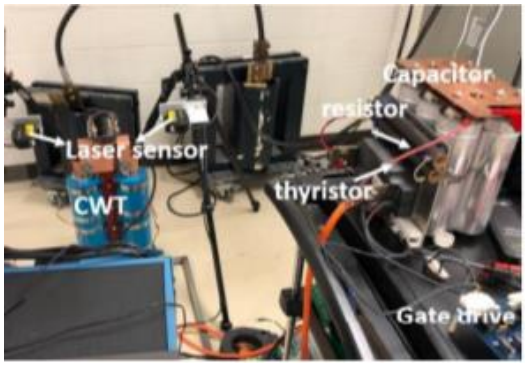

Figure 59 Test setup to understand forces under fault conditions

6.9.1 *Forces mechanism*

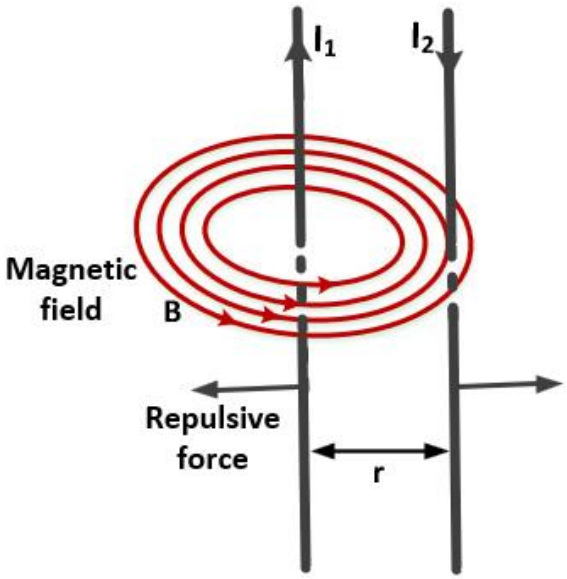

Figure 60 Representation of forces in two conductors

If two parallel conductors are carrying electric current, magnitude of forces with which they are acting on each other are equal and the following equation is applied

$$F = \frac{\mu_o \, I_1 I_2}{2\pi \, r} l \tag{21}$$

If the currents ($I_1 \; and \; I_2$) flow in the same direction, the conductors will attract and if the currents flow in the opposite direction, the conductors repel each other. A representative scenario of two conductors next to each other was simulated in Ansys Maxwell, where the conductors were 1.5 cm apart and exposed to 100 A. The Lorentz force was found to be 984 μN.

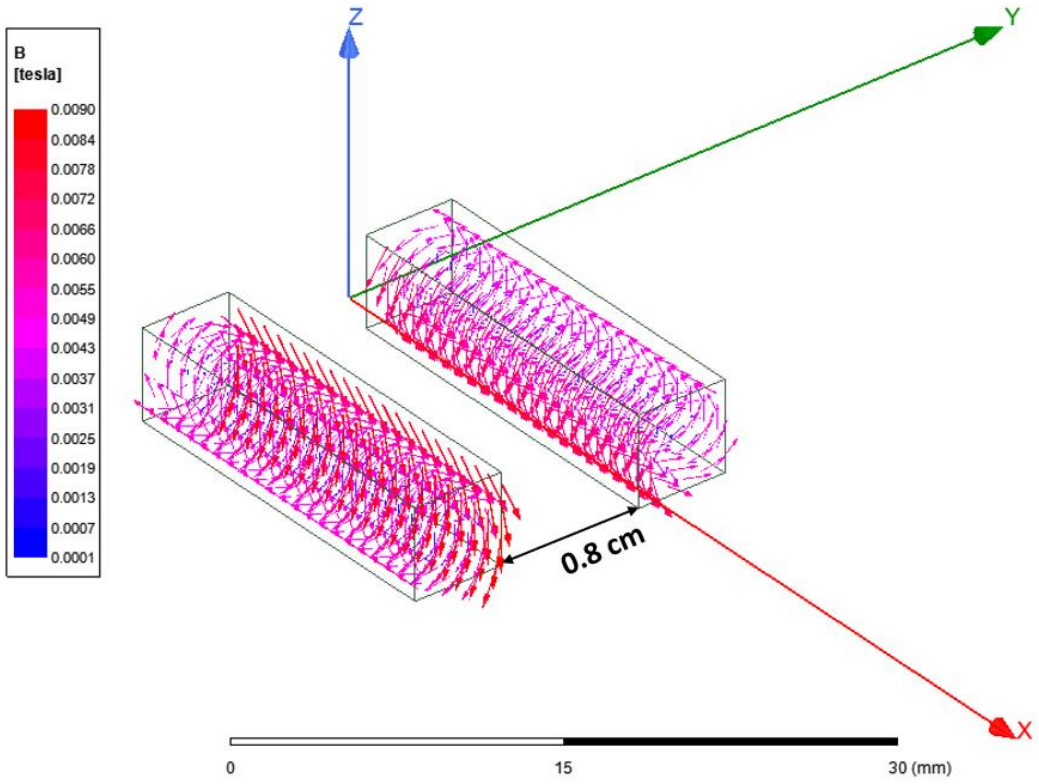

Figure 61 Simulation of magnetic flux density

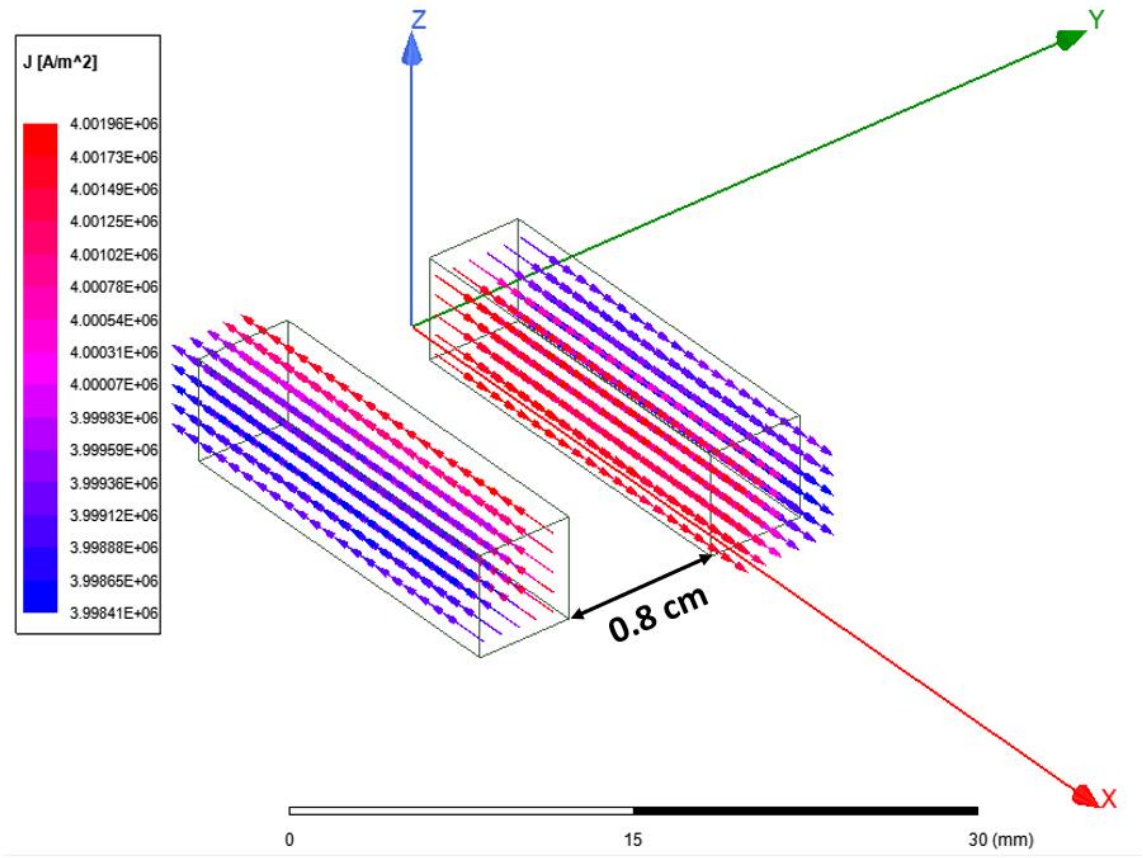

Figure 62 Simulation of current density

The distance between the two conductors was reduced to 0.8 cm with the other parameters unchanged. In this scenario, the force was found to be 1.53 mN. As the length (l) of the conductors and currents increase, the force increases and with the increase in the distance (r) between the conductors, the forces decrease. The current density and magnetic field plots are shown above. The simulation results of forces at other current levels have been summarized as below

Table 5 Lorentz forces simulated in Ansys Maxwell

Current (A)	Lorentz force (N) when the conductors are separated by 0.8 cm	Lorentz force (N) when the conductors are separated by 1.5 cm
50 A	381.9 μN	246.25 μN
100 A	1.53 mN	984 μN
250 A	9.54 mN	6.15 mN

6.9.2 *Experimental setup*

In order to test the ability of the device to handle forces under fault conditions, a test setup in the lab was built. The test setup consists of a thyristor-based circuit to charge a capacitor through a resistor and discharge the energy stored in the capacitor to the CVR device. The prototype was tested in controlled lab conditions. With the test setup in the lab, a 10 ms pulse of 530 A was applied on the low current side of the device. This led to 26000 A on the high current side. It was confirmed that the peak forces would not cause significant mechanical strain on the CWT. In order to quantify the forces acting under fault conditions, dynamic displacement of the device terminals on the primary under fault conditions was measured. Using laser interferometer-based displacement sensors and with no other support provided, the movement at the input terminals of the outside conductor was studied. Cables were used to short the terminals.

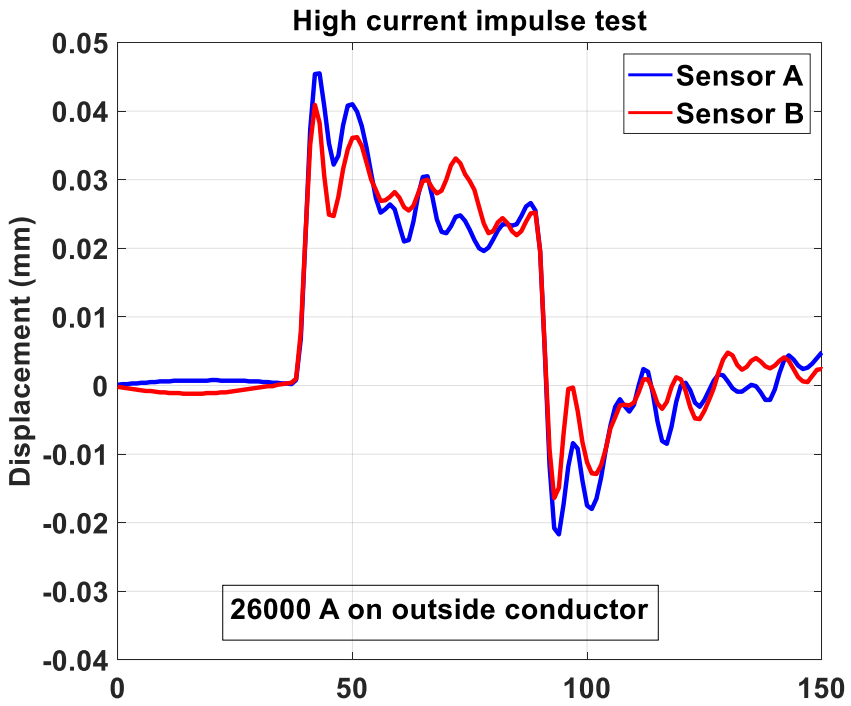

Figure 63 Measured displacement under high current magnitude

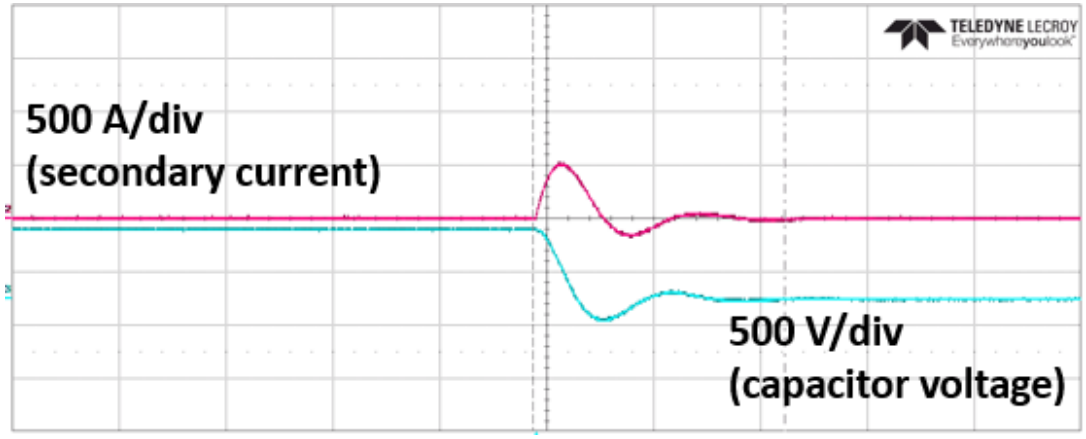

Figure 64 Oscilloscope measurements of capacitor voltage and secondary current

6.9.3 *Experimental results*

An extremely small movement of $\frac{4}{100th}$ of a millimeter was measured between the two terminals of outside conductor. This test was repeated several times for consistency and each time the maximum displacement was very close to 0.04 mm as shown in Figure 63. Since most of the forces act on the system during the first peak, this test gives a good validation to the ability of the device to be robust to handle the force. This contrasts with winding geometries in conventional transformers, where the high stresses can cause damage leading to failure.

The test showed a current of tens of thousands of amperes can flow through primary winding and it can sustain. But an issue with the secondary side or in the event of a failure of operation of relay on the secondary side, the device should not cause impact to plant operations.

Adding a bypass and breaker on the primary side, may add to the cost and complexity of implementation. As previously discussed, the device has been designed for a secondary bypass - the plant operations will not be impacted if there is a fault within the device. But it is important to understand a situation when the secondary bypass does not operate normally. Without a primary bypass and in the event of failure of the protective devices on the secondary side, the plant operation might be impacted. In other words, the device might act like an open transformer, where there will be current flow on one side and voltage is generated on the other side. It might act like high impedance in the circuit and might impact the operation of the industrial plant.

Results of open-circuit test on the secondary winding on the device (schematic : Figure 65) showed the impact of a rare scenario when the winding is disconnected from

source, which may lead to a case of voltage generated on the secondary side as current still flows on the outside conductor. Measurements in the lab at nominal conditions were made and projected to higher current levels. The experiment was performed in steps of 100 A, starting with 100 A up to 900 A. The core temperature was monitored while the experiment was done. It was seen that even at nominal conditions of current, the core is saturated when the secondary side is open circuit.

With more current on the primary, the core may be pushed to higher saturation when the secondary side is open, and the relative permeability of the core may decrease. At tens of kilo ampere, the core may be extremely saturated, and the device could behave close to an air-core transformer with the secondary side open and the core may heat up. The voltage drop due to the resistance of the copper tube and the drop across leakage inductance reflected on the primary side may need to be accounted for.

Simulations in MATLAB were done to obtain voltage on the primary side of the device up to a current of 3000 A. The voltage across primary, secondary and the flux obtained through simulations is shown in Figure 70. Concurrently voltage measurements at up to 900 A were made, as discussed in the previous paragraph (Figure 71, Figure 72). These results were accurately modeled in MATLAB and projected up to fault conditions of 30000 A with an arctangent fit [56, 57]. On the primary side, about 10 V at nominal conditions of 2500 A and 12 V under conditions of fault may be injected if there is an issue on the low current side (secondary) or if the low current side is open.

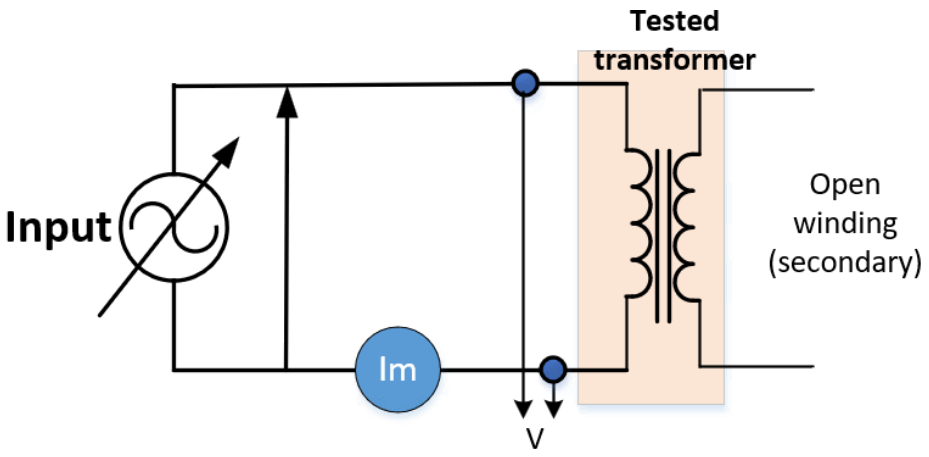

Figure 65 Test setup to understand open circuit situation

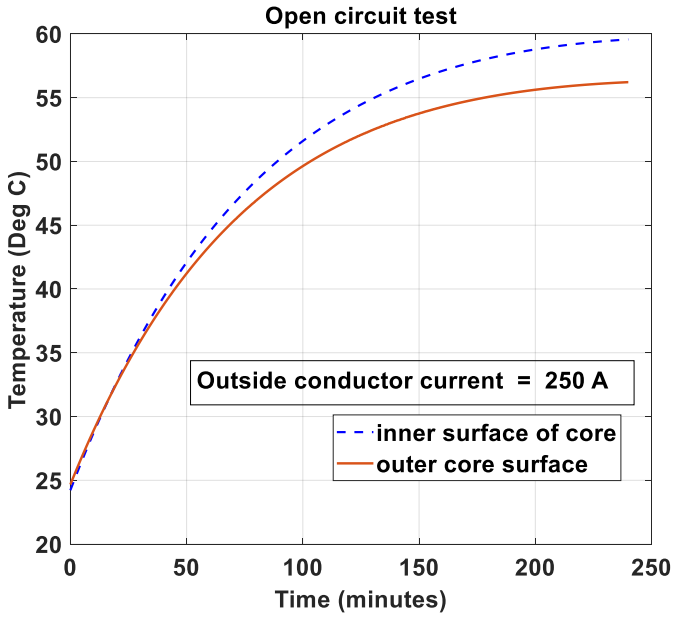

Figure 66 Core temperature without fan at 250 A

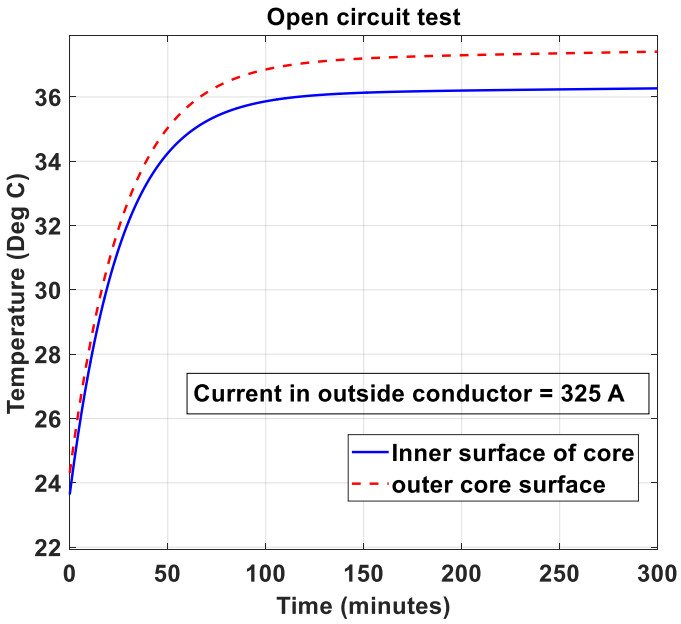

Figure 67 Core temperature with fan at 325 A

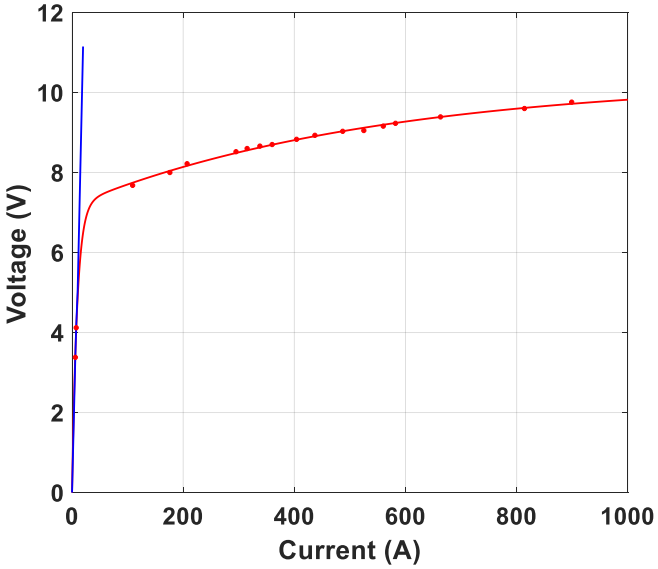

Figure 68 Measured voltage on primary side in the lab

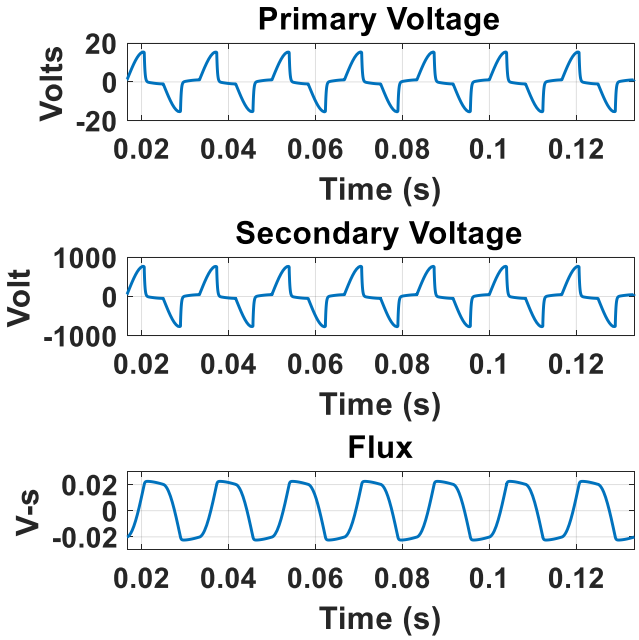

Figure 69 Matlab simulation to obtain voltage across primary at 2000 A

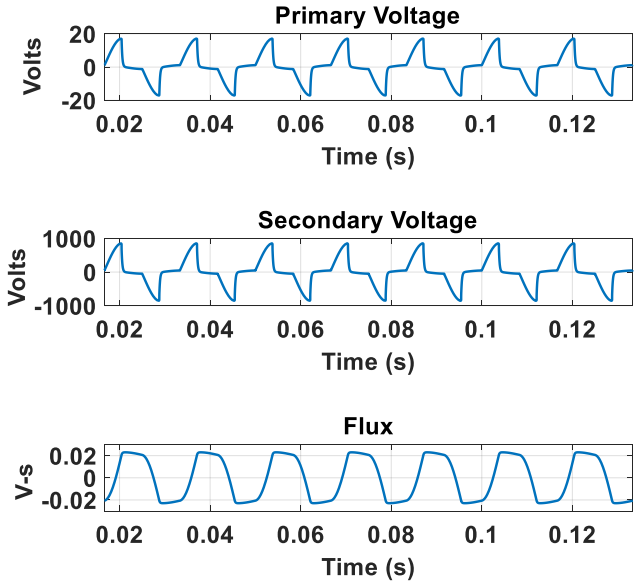

Figure 70 Matlab simulation to obtain voltage across primary at 3000 A

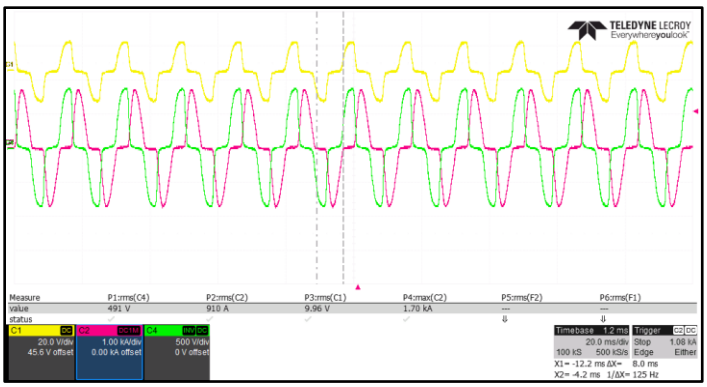

Figure 71 Experimental measurement of voltage across primary at 910 A

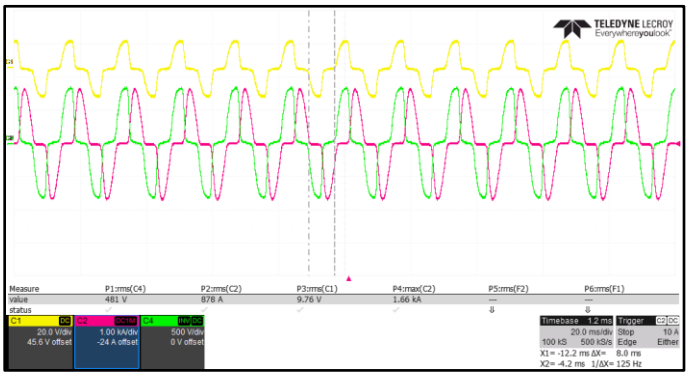

Figure 72 Experimental measurement of voltage across primary at 878 A

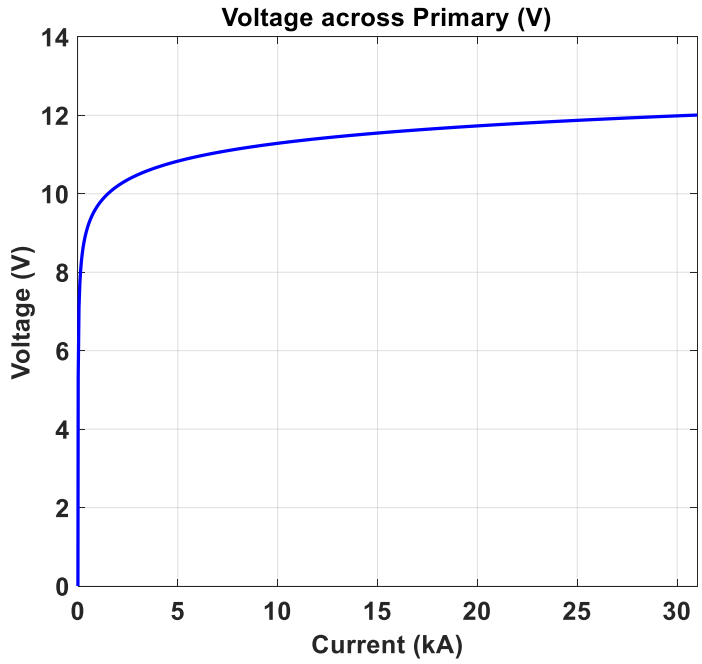

Figure 73 Voltage across device primary obtained using arctangent fit at higher current levels

Measurement of core temperature at different current levels has been shown in Figure 66 and Figure 67, by circulating current on the primary winding and having the high voltage side open. The results show that the fans in the device could assist in cooling the core in an open circuit situation and to able be able to work on the device installed in a system. Saturation leads to minimal impact to plant operations in the event of a fault within the device.

Table 6 Time constant of the core in an open circuit situation

Time constant of the core	
Ambient air	80 minutes
With fans	27 minutes

In addition, it is important to understand the impact of other associated issues such as arc flash with protective devices in the system. A short circuit and arc flash simulation study was conducted shown in Figure 74 in EasyPower software that showed that the protective devices in the power system may need to be properly coordinated along with the potential use of fast arc flash detection systems so as to ensure the incident energy could be minimized for personnel to safely work on them.

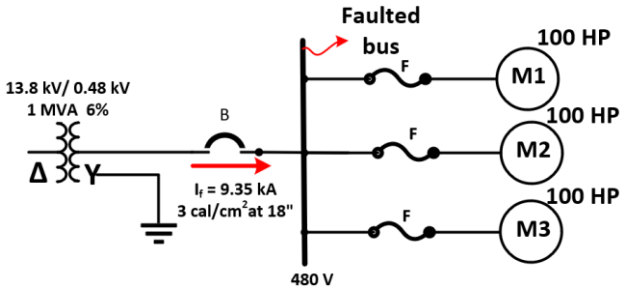

Figure 74 Simulation result of fault at 480 V bus

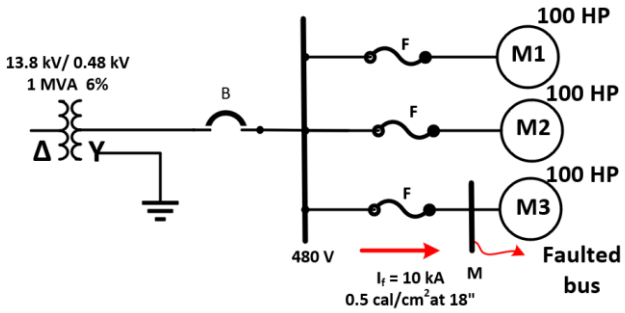

Figure 75 Simulation result of fault at bus M

The simulation results are based on momentary fault currents for half a cycle.

6.10 Efficiency

To be able to realize the maximum benefits of CVR, the device losses should be extremely low. Losses should not negate the savings that can be achieved. Based on the calculations, efficiency of the device was found to be over 99.82%. Theoretical value of the copper loss in the device was calculated as 201 W and core loss was calculated to be 68 W with a specific loss of $2.2\frac{\mathrm{W}}{\mathrm{kg}}$ provided by the manufacturer, as discussed in Table 7. The device was tested at 277 V (L-N) for core loss measurement and 1500 A for copper loss measurement summarized in Table 8.

With the short circuit test, the power consumption that is measured on the power meter includes loss in the copper bar used for shorting. A voltage of 46 mV was measured at the copper bar terminals and this translates to a loss in the copper bar of 70 W at 1500 A. At each square tab at the end turn, a voltage of 3.2 mV was measured, and this corresponds to a power of 4.8 W at 1500 A shown in Figure 76. With four such square tabs, the total loss at the end turns is 19.2 W. Two fans have been used to assist with cooling and this corresponds to a power consumption of 20 W each. The active cooling provides the ability to operate the device at higher current density. The efficiency of the device is well over 99.8%.

Table 7 Theoretical data for the device

Primary winding	Copper 101 Alloy
Secondary winding	10 AWG Magnet wire
Core	Silicon steel
Loss in copper tube	85.39 W
Loss in magnet wire	116 W
Core loss	68 W
SCR loss	45 W (during injection)
Efficiency	> 99.8%

Table 8 Experimental data for the device

3 phase system		277 V (L-N)
Current in primary		1500 A
Frequency		60 Hz
Losses		
Core loss	30 W	
Copper loss	230 W	
Loss in copper bar	70 W	
End turns	19.2 W	
Fan (power)	40 W	

Figure 76 Tabs on end turn where voltage was measured with multimeter

The outer diameter of the copper tube is chosen based on and is approximately equal to the inner diameter of the core. With the existing design, the core loss was calculated to be 68 W. One CWT will provide 2% injection at 1 MW. Energy we are targeting to save = 6%. Efficiency > 99.85% .

6.11 Thermal conditions and overload capability

Experimental measurement of temperature was done to understand the thermal behavior and the overload capability of the SIVOM system. Temperature measurements

starting at 500 A up until 1500 A were obtained until steady state. In this scenario, 30 A was passed through the secondary winding with primary winding shorted. This led to 1500 A on the outside conductor. It was observed that the temperature achieves steady state after two hours of test. Change in temperature from the ambient temperature of 23 deg C was calculated and projected at higher currents with a quadratic fit. With the collected data, the thermal time constant was extracted using MATLAB for the inside conductor. Based on the thermal time constant, continuous operation of up to 2500 A may be possible that could lead to a final temperature of 95 deg C with the fans. This is shown in Figure 78. Similarly, a short-term overloading operation of 3000 A for 5 minutes is permissible, without affecting the enameled wire temperature rating.

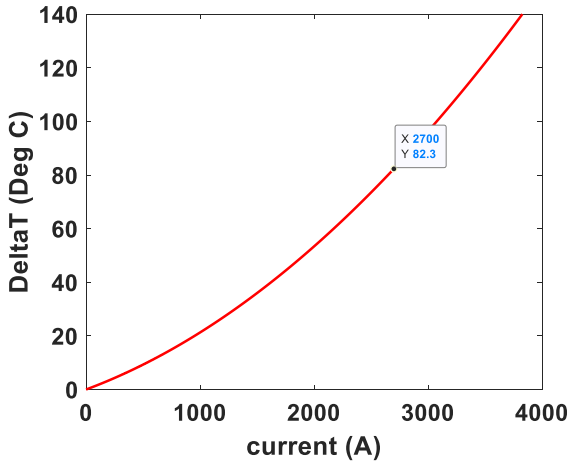

Figure 77 Temperature rise obtained using quadratic fit with 60 CFM fan

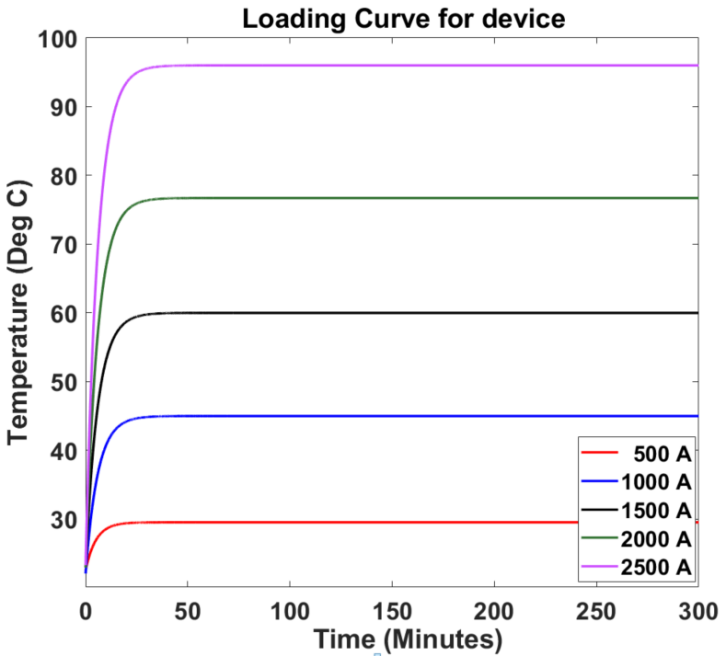

Figure 78 Thermal characterization and loading curve with 60 CFM fan in SIVOM device

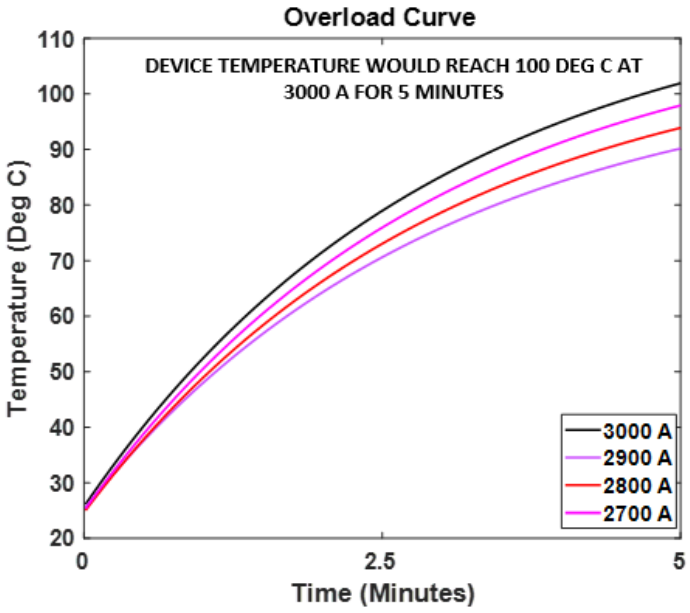

Figure 79 Thermal characterization and overloading curve in SIVOM device with fan at 60 CFM

SIVOM shows a new approach to improving energy efficiency and productivity at industrial plants. The paper discusses important requirements that have been identified and shown to be satisfied by the device. They are dynamic response capability, fail-normal capability, fault current management, efficiency, and thermal management. Experimental verification results of the device have been subsequently discussed. The results show that the device is suitable to implement CVR behind-the-meter. The ability to operate the device without bypass and breaker on the primary side offers a low-cost approach and reduces complexity of implementation.

CHAPTER 7. LOSSES AND PERFORMANCE CHARACTERIZATION

7.1 Problem statement

The power rating of a device is determined by its ability to avoid damaging temperature to insulation material or magnetic core [50]. Since a transformer will be exposed to continuous operation at high current levels, it is essential to verify the performance under these conditions. In addition, losses in the device need to be investigated to make sure the device performance is reasonable. These important aspects are discussed in this chapter.

Experimental results of losses and thermal characterization for power transformers have been discussed pertaining to industrial and utility applications.

A feature of a CWT as previously discussed is that, since the leakage field in the device exists only in the annular region between the two conductors and in any region the coaxial arrangement isn't maintained, the leakage field is prevented from entering the core material. Since the leakage field does not penetrate the core material, the energy stored in the field is lower.

This results in lower conductor losses and elimination of core losses due to leakage field. "*Since there is no leakage flux in the core there is no increase in eddy current and hysteresis losses in the core as the current increases and its consequential leakage field strength increase"* [50]

Investigation of losses as part of optimization could be useful for design improvement. A design optimization based on being able to understand the impact of a copper tube with a smaller diameter and with the same thickness and the associated tradeoffs is shown Figure 80. The weight of the core is given by

$$Weight = \rho_{core}\pi(r_{co}^2 - r_{ci}^2) * 2l_c \tag{22}$$

$$l_c = \frac{core\ length}{2} \tag{23}$$

Where ρ_{core} $is\ the\ density\ of\ the\ core$ $\left(\frac{kg}{m^3}\right)$

r_{co} $is\ the\ core\ outer\ radius\ and\ r_{ci}$ $is\ the\ inner\ radius\ of\ the\ core$

Hence the core volume and core weight along with the core losses could reduce.

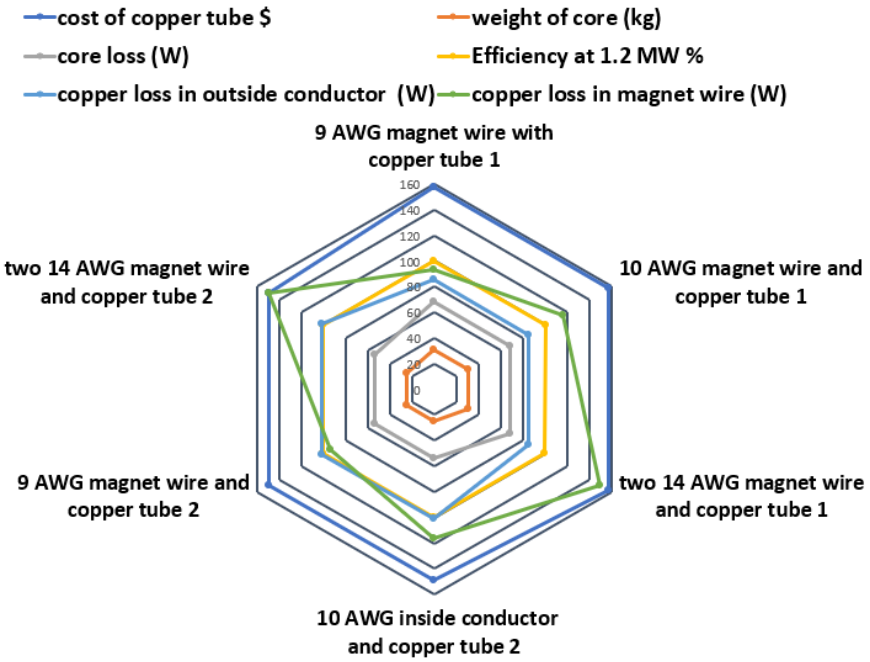

Figure 80 Design comparison and optimization

The dimensions are as follows:

Copper tube 1: OD: 2" and thickness: 0.125", copper tube 2: with diameter 1.5" and thickness 0.125". The analysis showed that the design corresponding to copper tube 1 with a 10 AWG inside conductor (diameter: 0.1019"), with a core that has an ID: 2.125" and OD: 4.125" gives a good performance. The following section based on Keith Klontz's work [50] explains in more detail the effects of changes to other parameters in axial or radial direction. In the above calculation, since the length (l_c) and thickness of the core have been unchanged, A_c is not impacted.

7.2 Sensitivity of parameters

The following equations give a basis for the change in axial or radial dimension of the device. For a change in axial dimension, the old length is l and the new length is Kl. For a change in radial dimension, the old radius is r and the new radius Kr, $Sensitivity\ (r)$ corresponds to a radial dimension change $Sensitivity\ (a)$ corresponds to an axial dimension change [50].

Voltage:

$$V_{rms} = 4K_w N f B_m A_c \ \ (V) \tag{24}$$

where A_c is the core flux area cross section (m^2), B_m is the peak flux density (T), f is the excitation frequency (Hz), N is the number of turns on the primary, K_w = 1.11 for sinusoidal voltage .

Change in radial dimension:

$$A_c \propto K\,(r_{co} - r_{ci}) \tag{25}$$

$$A_c \propto K$$

Where r_{co} is the outer radius of the core, r_{ci} is the inner radius of the core, l_{core} is the core length

$$\therefore V_{rms} \Rightarrow KV_{rms} \quad Sensitivity(\text{r}) = 1$$

Change in axial dimension:

$$A_c \propto l_{core} \propto K$$

$$\therefore V_{rms} \Rightarrow KV_{rms} \quad Sensitivity(\text{a}) = 1$$

Voltage changes if the radial or axial dimension changes [50].

Current capacity (I)

Change in radial dimension:

$$I \propto A_{cu} \text{ per turn} \tag{26}$$

$$thickness\ of\ copper\ tube = \Delta r$$

Outer radius of copper tube = r_{cu-o}

Inner radius of copper tube $r_{cu-i} = r_{cu-o} - \Delta r$

$$I \propto \pi \left(r_{cu-o}^2 - r_{cu-i}^2\right) \tag{27}$$

If the radius of the copper tube changes,

$$\left(r_{cu-o}^2 - r_{cu-i}^2\right) = \left(r_{cu-o} - r_{cu-i}\right)\left(r_{cu-o} + r_{cu-i}\right) \tag{28}$$

$$\therefore \; I \Rightarrow KI, sensitivity(\mathrm{r}) = 1 \quad \text{(if thickness } \left(r_{cu-o} - r_{cu-i}\right) \text{ is constant)}$$

Change in axial dimension:

$$A_{cu} \propto constant \therefore I = constant \tag{29}$$

$$sensitivity(\mathrm{a}) = 0$$

Current capacity is proportional to radial dimension change [50]

Weight:

$$weight \propto \pi r^2 (2l) \tag{30}$$

Change in radial dimension:

$$weight \Rightarrow K^2 * weight,$$

$$Sensitivity\ (\mathrm{r}) = 2$$

Change in axial dimension:

$$weight \Rightarrow K * weight,$$

$$\therefore Sensitivity\ (a) = 1$$

Weight is proportional to radial and axial dimension change.

Losses:

Copper loss:

Change in radial dimension:

$$P_{cu} = I^2R \tag{31}$$

$$R = \rho * \frac{Mean\ length\ per\ turn\ (MLT)}{A_{cu}}$$

$$\therefore R \Rightarrow \frac{R}{k}\ (since\ A_{cu} \propto K)$$

$$P_{cu} \Rightarrow \frac{K^2}{K} P_{cu}$$

$$Sensitivity\ (r) = 1$$

Change in axial dimension:

$$P_{cu} = I^2R \tag{32}$$

$$P_{cu} \propto KP_{cu}$$

$$Sensitivity\ (a)\ =\ 1$$

Losses are proportional to axial and radial dimension changes [50].

Core loss:

Change in radial dimension:

$$P_{core} = B^n * Volume \tag{33}$$

$$V_{rms} = 4K_w N f B_m A_c\ \ (V) \tag{34}$$

$$B^n \propto \left(\frac{V_{rms}}{A_c}\right)^n \tag{35}$$

$$\text{Volume} \propto \pi(r_{co}^2 - r_{ci}^2) l_{core}\ \ \propto \pi(r_{co} - r_{ci})(r_{co} + r_{ci}) l_{core} \tag{36}$$

In general, $P_{core}\ \ \Rightarrow K^2\ P_{core}$

$$Sensitivity\ (r)\ =\ 2;$$

Change in axial dimension:

$$P_{core} = B^n(Volume) \tag{37}$$

$$P_{core} \propto (1)^n(K)\ \ Sensitivity\ (a) = 1$$

Core loss is proportional to axial and radial dimension change [50]

KVA (Pin) :

Change in radial dimension:

$$KVA \propto VI \tag{38}$$

In general, $kVA \propto K * K \Rightarrow K^2(KVA)$

$$Sensitivity \text{ (r)} = 2$$

Change in axial dimension

$$KVA \propto VI$$

$$\therefore kVA \propto K$$

$$Sensitivity \text{ (a)} = 1$$

KVA is proportional to axial and radial dimension changes [50]

Weight density: (ρ_w)

Change in radial dimension

$$\rho_w \propto \frac{P_{in}}{Weight} \tag{39}$$

$$P_{in} \propto K^2 \; and \; Weight \propto K^2$$

$$\therefore \rho_w \; is \; constant$$

$$Sensitivity\ (\mathrm{r}) = 0$$

Change in axial dimension

$$\rho_w \propto \frac{P_{in}}{Weight}$$

$$P_{in} \propto K\ weight\ \propto K,$$

$$Sensitivity\ (\mathrm{a}) = 0$$

Reference [50] suggests weight density does not change based on axial or radial dimension change

Volume density: (ρ_v)

Change in radial dimension

$$\rho_v \propto \frac{P_{in}}{volume} \tag{40}$$

$$P_{in} \propto K^2\ and\ volume\ \propto K^2$$

$$\therefore \rho_v\ is\ constant$$

$$Sensitivity\ (\mathrm{r}) = 0$$

Change in axial dimension

$$\rho_v \propto \frac{P_{in}}{volume}$$

$$P_{in} \propto K\ and\ volume\ \propto K$$

$$Sensitivity\ (a) = 0$$

Volume density does not change based on radial and axial dimension change [50]

Temperature rise:

Change in radial dimension

$$\Delta T \propto \frac{losses}{A_{surf}} \tag{41}$$

$$A_{surf} \propto \pi r^2 + 2\pi r\ (2l_c) \tag{42}$$

In the device under normal operating conditions, copper loss > core loss

$$P_{cu} \propto K\ ;\ A_{surf} \propto K^2$$

$$\therefore \Delta T \Rightarrow \frac{\Delta T}{K}$$

$$Sensitivity\ (r) = -1;$$

Change in axial dimension

$$\Delta T \propto \frac{losses}{A_{surf}} \tag{43}$$

$$P_{cu} \propto K\ ;\ A_{surf} \propto K$$

$$\therefore \Delta T\ is\ constant$$

$$Sensitivity\ (a)\ =\ 0;$$

Change in the radius of the copper tube would affect the temperature rise as the surface area is impacted [50]. A more reasonable understanding and device optimization could be possible through a cooling mechanism that would allow operation of the device at various power levels without having to cause a change in the fundamental topology. A summary of the sensitivity factors is provided below [50]

Table 9 Summary of sensitivity factors in SIVOM device

Parameter	Sensitivity (a)	Sensitivity (r)
Voltage:	1	1
Current capacity (I)	0	1
Weight:	1	2
Copper Loss	1	1
Core loss	1	2
KVA	1	2
Weight density	0	0
Volume density	0	0
Temperature rise	0	-1

The sensitivity factors may be useful for design improvement as part of a future work as well as understand the effects of possible changes to device dimensions.

7.3 Discussion of losses in a CWT

The important sources of heat in the device are copper losses in the primary and secondary and core losses. Copper loss is a function of localized current density and effective conductor resistivity. Under normal operating conditions, the dominant loss component is the copper loss in the device. Under extreme conditions when there is an

open circuit situation on the high voltage winding, the core loss may increase along with heating up of core due to saturation phenomenon as discussed in the previous section. Fans at two locations have been included for sustained operation at high-power levels. Polynomial and exponential models have been used for projection of temperature and extraction of the time constant to provide a reasonable estimate.

7.4 Thermal characterization of the 1.66 MW CWT without fan

Based on second law of thermodynamics, flow of heat is from hot to cold. The device is essentially supported with mounting hardware and held in place with a thermally insulating material (wooden fixture). Hence the dominant heat transfer mechanism is convection from a surface to ambient air.

Heat generated in the transformer must find a way to the ambient for safe operation at high power. The different sources of heat in the device are the primary winding loss, secondary winding loss, core loss and SCR loss. The primary winding and secondary winding loss correspond to the copper loss that is factored in. Except at the end turns, the core surrounds the copper tube. Hence, heat must be transmitted radially through the module from the inside conductor to the core.

Under normal operating conditions, heat is primarily generated by the losses in the primary and secondary winding. At 610 A, a maximum loss of 14.12 W is seen in the copper tube along with 19.5 W of copper loss in the inside conductor (with 50 turns). Core loss would theoretically equal 68 W assuming a specific loss of 2.2 W/kg. Experimental measurement of core loss is shown in Figure 81. Measurement of copper loss was performed at up to 1200 A and a copper bar was used to short the terminals of the outside

conductor. A voltage drop of 40 mV was measured at the copper bar terminals and the loss in the copper bar was 48 W at 1200 A. The core loss at 277 V was measured to be 30 W.

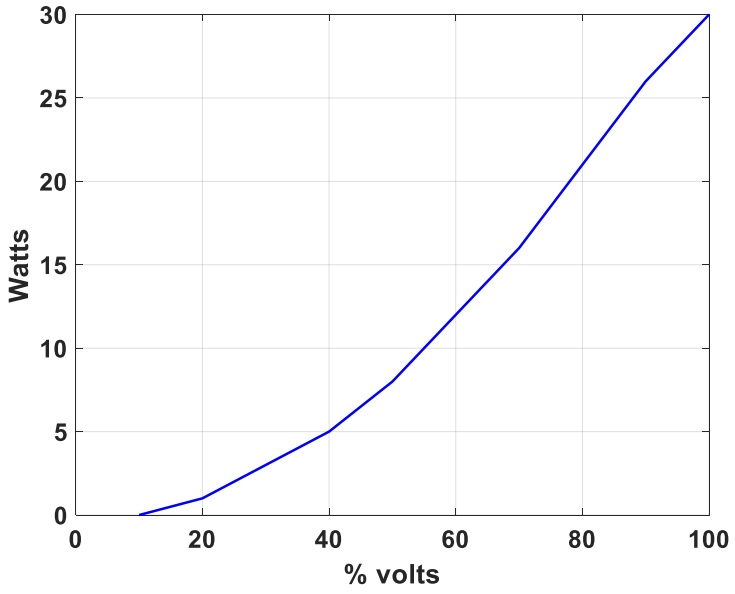

Figure 81 Core loss measurement

A steady state thermal model is discussed below. $Q_{outside\ conductor}$ refers to the copper loss in the primary winding, $Q_{inside\ conductor}$ refers to the losses in the secondary conductor, Q_{core} refers to the core loss.

The temperature gradient between the magnet wire and the copper tube would provide a path for convective transfer of heat. The heat is then transferred radially from the copper tube to the inner core surface through conduction. Heat from the inner core surface is conducted through the body of the core to the outer core surface. From the outer surface of the core, the heat is transferred through convection to ambient air. The cores may be held together through the use of metal clamps, that may provide a path to conduct the heat from the outer surface of the core.

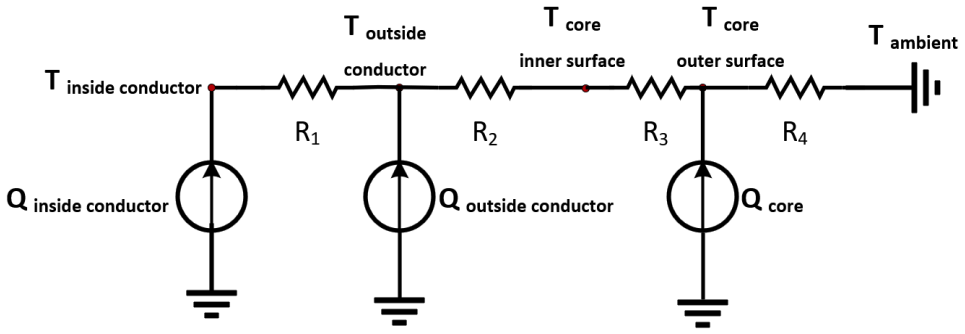

Figure 82 Thermal equivalent circuit under normal operating conditions

The equivalent circuit or the steady state thermal model at the end turn is shown in Figure 83. Since the core is not present at the end turns, majority of the heat transfer will occur radially due to convection from the magnet wire to the copper tube. The heat from the outer surface of the copper tube will then be transferred to the surrounding through convection.

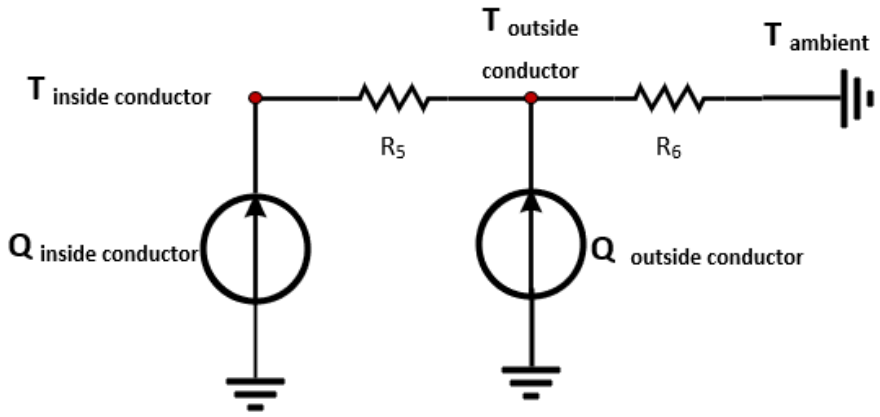

Figure 83 Thermal equivalent circuit under normal operating conditions (end turns)

Table 10 Explanation of notation in thermal equivalent circuit

Notation	Explanation
$T_{inside\ conductor}$	Temperature of secondary winding
$Q_{inside\ conductor}$	Losses in the secondary winding
$T_{outside\ conductor}$	Temperature of the primary winding
$Q_{outside\ conductor}$	Losses in the primary winding
$T_{core\ inner\ surface}$	Temperature of the inner core surface
$T_{core\ outer\ surface}$	Temperature of the outer core surface
Q_{core}	Core loss
$T_{ambient}$	Ambient temperature

The thermal resistance values are discussed in Table 11. Further discussion is provided in Appendix F.

Table 11 Thermal resistances under normal operating conditions

Notation	Mechanism of transfer of heat	Thermal Resistance
R_1	Convective transfer of heat from magnet wire to the copper tube	$R_1 = \frac{1}{\bar{h}\, A_{sec}}$ °C/W
R_2	Conduction from copper tube to inner surface of core	$R_2 = \frac{ln\left(\frac{R_{core\ inner}}{R_{primary\ outer}}\right)}{2\pi\, L_c\, \lambda_{primary}}$ °C/W
R_3	Conduction through the core	$R_3 = \frac{\ln\left(\frac{R_{core\ outer}}{R_{core\ inner}}\right)}{2\pi L_c \lambda_{core}}$ °C/W
R_4	Convection from outer surface of core to the ambient air	$R_4 = \frac{1}{\bar{h}\, A_{core}}$ °C/W

Thermal resistance values under normal operating conditions (end turns) are discussed in Table 12.

Table 12 Thermal resistances under normal operating conditions (end turns)

Notation	Mechanism of heat transfer	Thermal Resistance
R_5	Convective transfer of heat from magnet wire to the copper tube	$R_5 = \frac{1}{\bar{h}A_{sec}} °C/W$
R_6	Convection from outer surface of the copper tube to the ambient air	$R_6 = \frac{1}{\bar{h}A_{primary}} °C/W$

Thermal capacitance is the ability of the body to store thermal energy and is a function of mass density (ρ) (kg/m^3), specific heat (c) ($Jkg^{-1}K^{-1}$) and material's volume (V_m) (m^3). Thermal capacitance is given by

$$C_t = \rho V_m c \tag{44}$$

Copper conductors and core are components whose thermal capacitance may be important. For the materials of interest, the specific heat and mass density are assumed to be the following [50, 58]

Table 13 Specific heat and mass density of some materials

Material	Specific Heat ($Jkg^{-1}K^{-1}$)	Mass density (kg/m^3)
Copper	385	8933
Silicon steel	460	7650

The volume of the core is discussed in chapter 6. Similarly, the volume of the primary conductor may be calculated based on the device dimensions previously discussed. Using equation (44), the thermal capacitance may be determined.

Since the model deals with steady state calculations, capacitances are not discussed in the thermal equivalent circuit [59]. For safety reasons, the transformer may be required to be in an enclosure, that may provide a small additional thermal resistance to the heat flux and possibly raise the operating temperature slightly [59]. The thermal equivalent circuits shown in Figure 82 and Figure 83 are valid and applicable with the exception that the ambient temperature would be replaced by the temperature of the enclosure since transformer is not exposed directly to the surroundings at the ambient temperature.

Figure 84 shows the test schematic for evaluation of thermal performance. The setup is powered through a single phase variac to adjust the voltage. A step-down transformer and an inductive load are connected to the primary winding of the device. The device was exposed to 400 A and 610 A continuously and the temperature of the inside conductor, the thermally limiting component in the device was measured with

thermocouple until the temperature reached steady state. It was observed that the temperature reached the final value after three hours of test as discussed in Figure 85

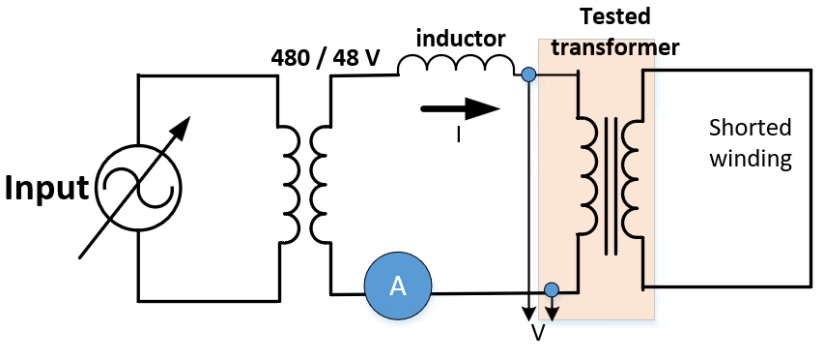

Figure 84 Test setup to device performance under short circuit

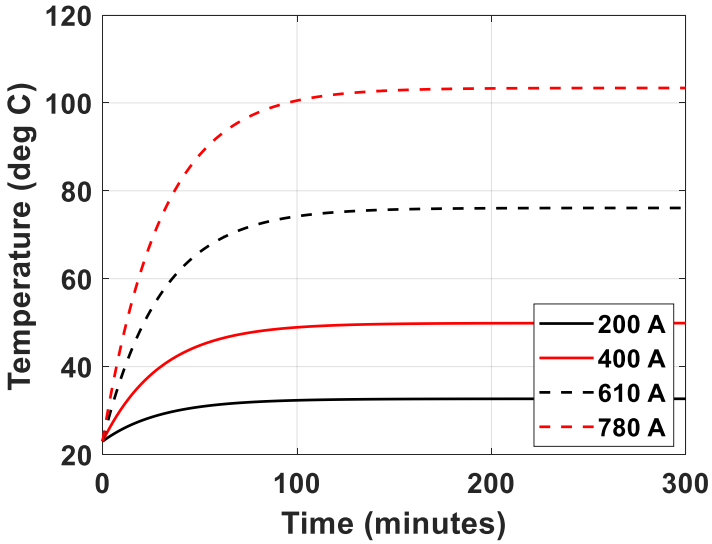

Figure 85 Loading curve of the device at 610 A and 400 A without fan

The time constant was found to be 30 minutes and the temperature reached 76.1 deg Celsius when 610 A was passed through the primary winding for 3 hours with the secondary winding shorted. At the end turn, the temperature was measured to be 75.7 deg

Celsius at 610 A. The thermal resistance and thermal capacitance for the inside conductor were extracted to be 2.359 $℃/W$ and 12.71 $J/℃$ respectively. The slope of the plot between total loss (W) and temperature (deg C) is used to extract the thermal resistance shown in the figure below (obtained using linear regression). Knowing the thermal resistance and the time constant, the thermal capacitance may be obtained.

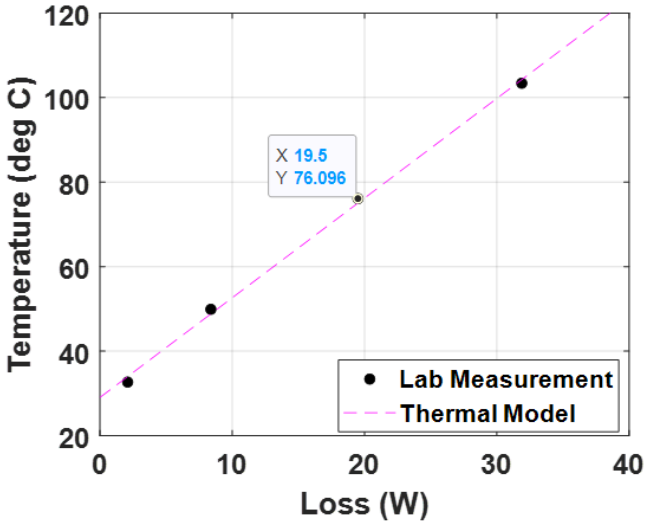

Figure 86 Comparison of lab measurement and thermal model

Furthermore, the thermal model is used to calculate the maximum allowable loss in the inside conductor for a change in ambient temperature. It can be seen from Figure 87 that for an increase in the ambient temperature, the permissible losses in the inside conductor decrease for the given operating conditions.

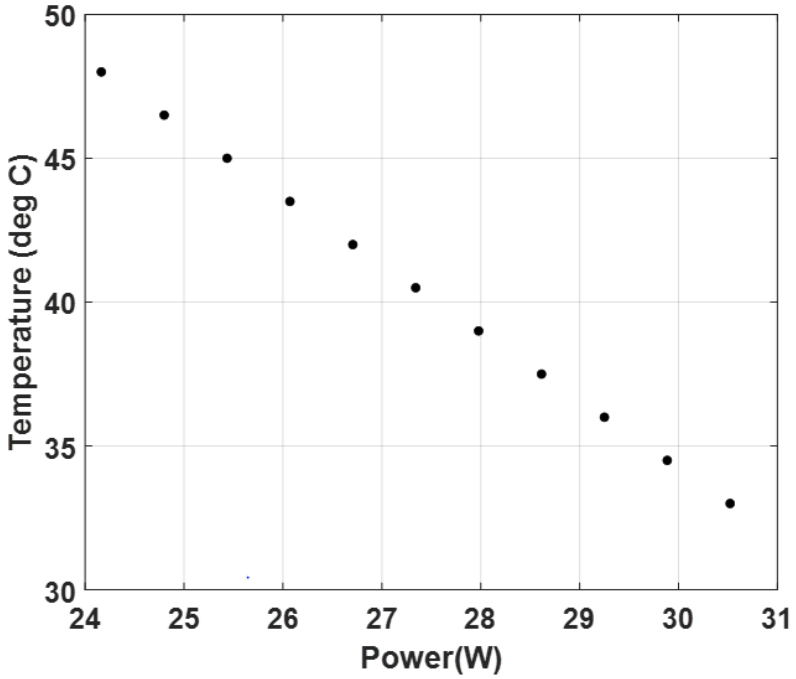

Figure 87 Permissible loss in the inside conductor at different ambient temperature

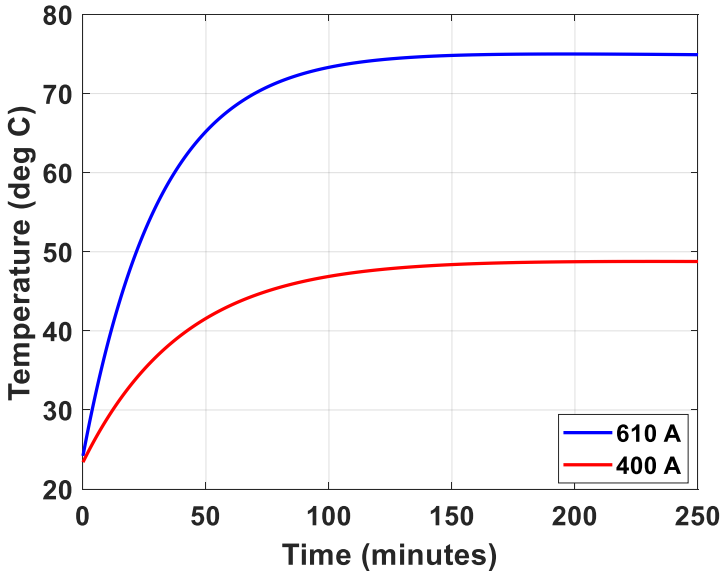

Figure 88 Loading curve of the device at 610 A and 400 A without fan (end turn)

The curves for the outside conductor have been shown in Figure 89 and the time constant was extracted to be 50 minutes and the thermal resistance was extracted to be 0.9319 ℃/W.

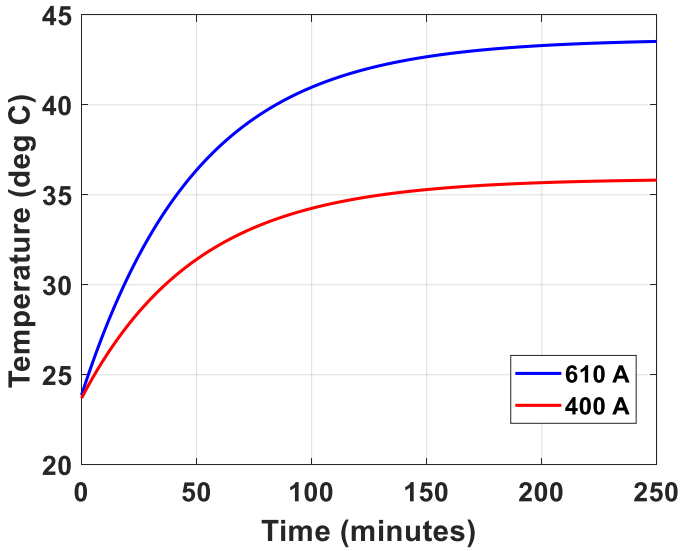

Figure 89 Loading curve of the device at 610 A and 400 A (outside conductor)

The temperature rise of the device at 1200 A is shown in Figure 90 without cooling. For the CWT to have sustained operation at higher power levels of 1200 A (1 MW) or 2500 A (2 MW) this would necessitate cooling the device with air or oil to prevent harm to the insulation of the inside conductor. Further discussion is provided in appendix F.

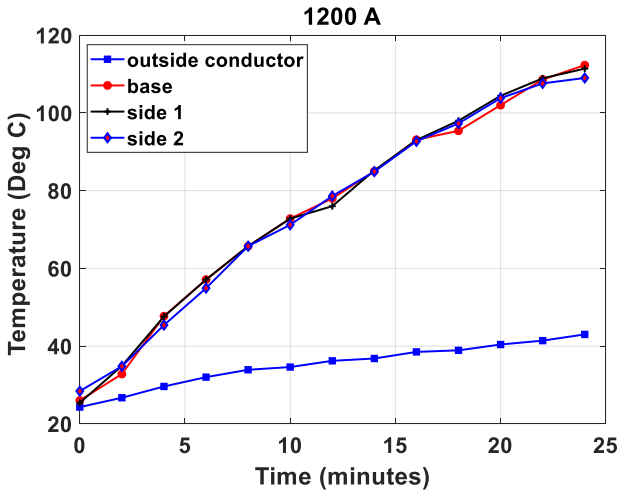

Figure 90 Temperature rise at 1200 A without fan

7.5 Thermal characterization with fans

The following equations are fundamental to being able to model and project loading and overloading characteristics. The transfer of heat from the body to the ambient at a given time is proportional to the temperature difference ($\Delta T = T - T_a$) between the body and the ambient, given by

$$\frac{d\Delta T}{dT} + \frac{1}{\tau}\Delta T = 0 \tag{45}$$

The solution to the above equation is given by

$$\Delta T(t) = \Delta T_0 \exp(-t/\tau) \tag{46}$$

Where ΔT_0 is the initial temperature difference and τ is the time constant.

In this section, the thermal performance of the CWT at 1.66 MW is discussed with the presence of fans at two locations, shown in Figure 33. The performance with a 30 CFM fan has been discussed and temperature is projected at higher currents.

Detailed thermal characterization studies were performed to understand how the device rating could be optimized with cooling. With a 30 CFM fan, temperature measurements at up to 1450 A on the outside conductor were made in the lab and projected to higher currents with a quadratic fit. Equation (46) is used to extract loading and overloading characteristics. This experiment was performed by shorting the outside conductor and passing 29 A through the inside conductor.

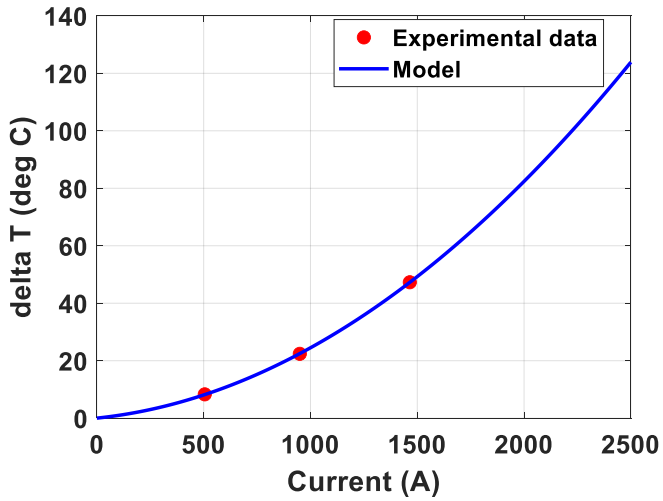

Figure 91 Temperature rise obtained using quadratic fit with 30 CFM fan

The time constant (inside conductor) was extracted to be 5.5 minutes. Data was similarly extracted for the outside conductor and the parameters of the model and the time constant were obtained using MATLAB. The time constant was found to be 12.2 minutes. The

thermal resistance and capacitances extracted using MATLAB are summarized in the table below.

Table 14 Thermal Resistance and Capacitance with fan

Device Component	Thermal Resistance ℃/W	Thermal Capacitance J/℃
Inside conductor	0.387	14.21
Outside Conductor	0.1722	70.84

The slope of the plot (regression coefficient) between temperature (℃) and the total loss in (W) yields the thermal resistance. Knowing the time constant and the thermal resistance, the thermal capacitance may be calculated shown in Figure 92.

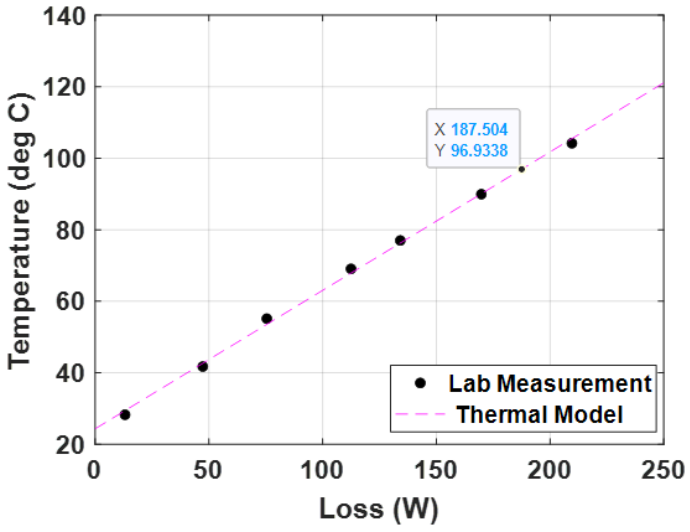

Figure 92 Comparison of lab measurement and thermal model for inside conductor

A comparison of temperatures of the inside conductor and the copper tube have been shown in the following figures.

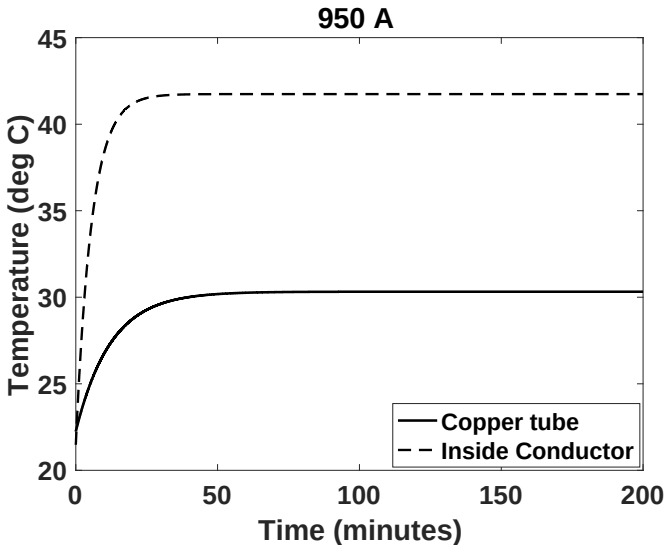

Figure 93 Temperature of the inside and outside conductor at 950 A

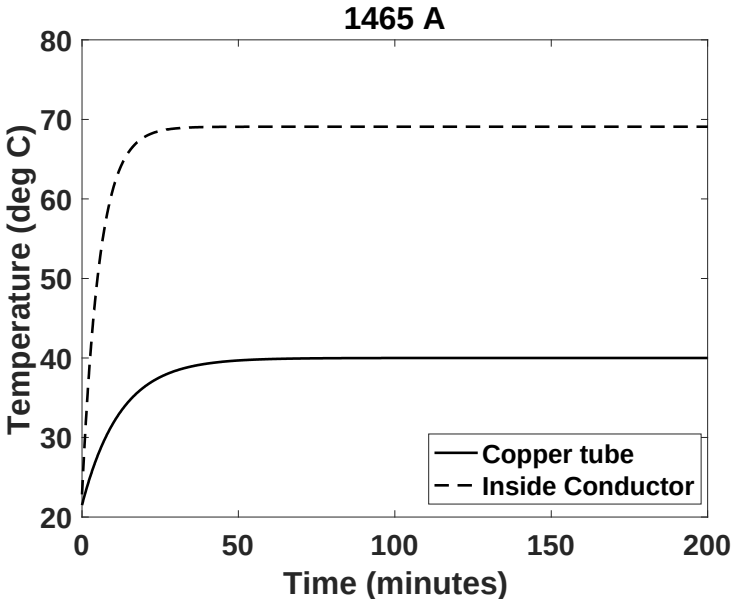

Figure 94 Temperature of the inside and outside conductor at 1465 A

It was observed that continuous operation of up to 2000 A and short-term operation of 2500 A could be possible shown in Figure 95

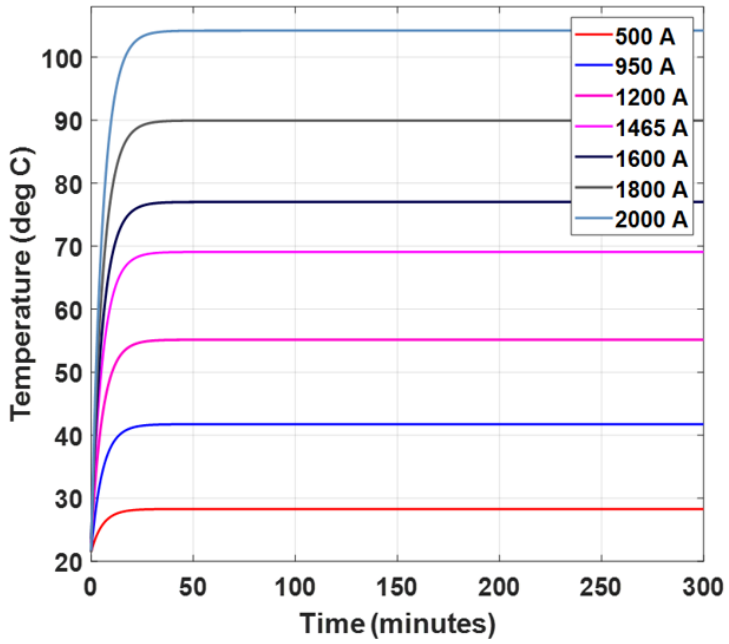

Figure 95 Loading curve of the device with 30 CFM Fan

With a 30 CFM fan, a final temperature of 104.2 deg C may be seen at 2000 A on the inside conductor. The expected temperature at different current levels have been shown in Figure 95. The overloading characteristics of the device have been shown below.

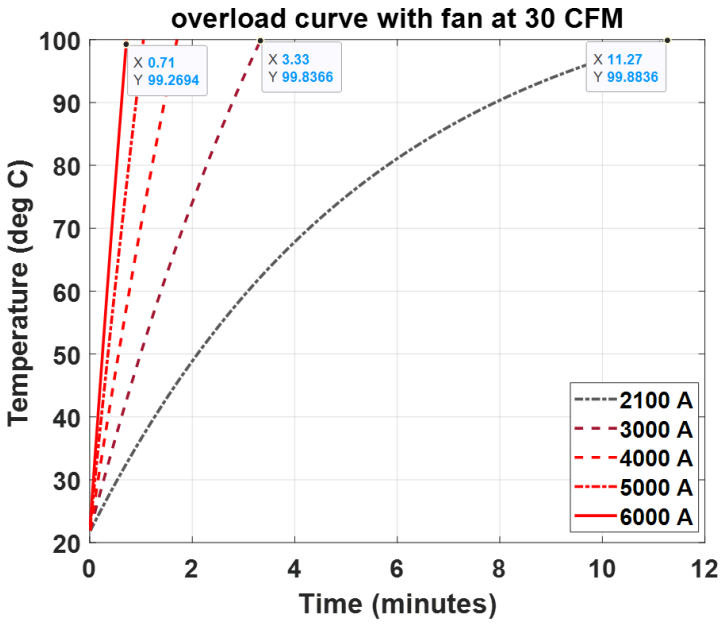

Figure 96 Overloading characteristics of the device up to 6000 A

The overloading characteristics at up to 6000 A is shown in Figure 96. For the temperature of the inside conductor to reach close to 99.26 deg C, it may take 0.71 minutes at 6000 A .

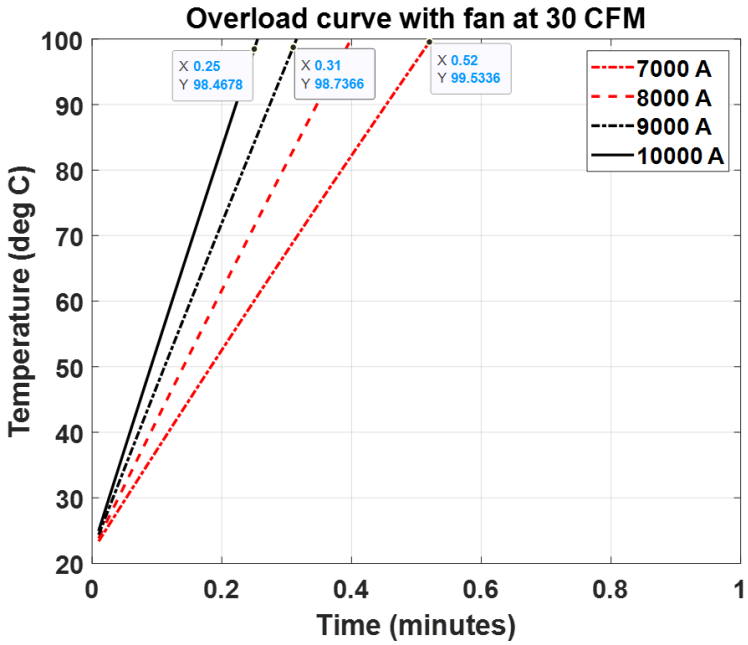

Figure 97 Overloading characteristics of the device up to 10000 A

From the overloading characteristics shown in Figure 97 it may be seen that for the temperature of the inside conductor to reach close to 98.46 deg C, it may take 0.25 minutes at 10000 A.

To further improve the operation at higher current density a 60 CFM was selected by Brandon. The experimental results of thermal characterization have been discussed in chapter 6.

With a 60 CFM fan, a power level of 2 MW was achieved along with the ability to achieve a short-term overloading capability of 3000 A for 5 minutes in comparison with a 30 CFM fan, with which continuous operation of 2000 A (1.66 MW) was achieved and a short-term overloading capability of 2500 A for 5 minutes without affecting the enameled wire insulating rating. Projected results up to 10000 A have been discussed.

The loading curves at the specified current levels and the time taken to reach a final temperature 100 deg C is summarized in Figure 96 and Figure 97. The summary of device performance at different ratings is shown in Table 16 and Table 17

Table 15 System specifications

Primary current (A)	2000 A
voltage	480 V
Voltage variation	± 10%
Frequency	60 Hz
B peak	1.3 T
Injection	6%
Phase	1 or 3

Table 16 Comparison of design and performance

Secondary Voltage (V)	277 V (L-N)	277 (L-N)	277 (L-N)
Current in primary (A)	610 A	1200 A	1500 A
Current in secondary (A)	12.2 A	24 A	30 A
Primary to sec turns	1/50	1/50	1/50
Frequency	60 Hz	60 Hz	60 Hz
Inside conductor diameter	2.58 mm	2.58 mm	2.588 mm
B peak	1.3 T	1.3 T	1.3 T
Core length	0.62 m (24.4 in)	0.62 m (24.4 in)	0.62 m (24.4 in)
Core height	15.24 cm	15.24 cm	15.24 cm
Core ID	5.3975 cm	5.3975 cm	5.3975 cm
Core OD	10.4775 cm	10.4775 cm	10.477 cm
Core weight	30.9 kg	30.9 kg	30.9 kg
No of cores	2 on each side	2 on each side	2 on each side
Inside conductor	Magnet wire	Magnet wire	Magnet wire
Core loss (2.2 W/kg)	68 W	68 W	68 W
Loss in magnet wire	19.5 W	75.4 W	116 W
Loss in copper tube	14.12 W	54.6 W	85.39 W
Efficiency	99.8 % (507 KW)	99.82% (1MW)	99.8% (1.2 MW)
Type of cooling	Ambient air	Fan	Fan

Table 17 Summary of device converter rating

Converter power Rating	3.37 kVA	6.6 kVA	8.3 kVA
Secondary Voltage (V)	277 V (L-N)	277 (L-N)	277 V (L-N)
Voltage variation	± 10%	± 10%	± 10%
Current in secondary (A)	12.2 A	24 A	30 A
Primary to sec turns	1/50	1/50	1/50
frequency	60 Hz	60 Hz	60 Hz
Phase	1 or 3	1 or 3	1 or 3

7.6 Losses in the converter at 30 A

I_{peak} = 42.42 A

R = 3.7 mOhm

Forward voltage drop = 1.26 V

$$I_{ave} = \frac{I_{peak}}{\pi} = \frac{30 * 1.414}{3.14} = 13.51\ A \quad (47)$$

$$Loss\ in\ one\ SCR\ = V_t I_{ave} + (I_{rms}^2 * R)\ = (17.02) + (30*30*3.7/1000) \quad (48)$$

$$= 20.4\ W$$

Additional losses with two SCR: 40.8 W

Total losses: 40.8 + 269.39 = 310.19 W

7.7 Utility applications

For utility applications, the suggested cooling method was inert oil and the system performance was investigated. Con Ed has a meshed secondary network in the city of NYC – Each sub grid is of the order of about 10 - 20 MW. Secondary grid has multiple 1000 KVA or 500 KVA transformers feeding the loads in the grid appropriately at 120 V –

loading gets unbalanced as a line goes down or when there is a cluster of large loading near one transformer. There are vaults on the sidewalk where the transformers and the network protectors are. The space left in the vault is about 2 FT X 3 FT X 2 FT is where a MW scale power flow controller unit should be installed making it challenging. For the mesh to be less susceptible to interruption when transformer failures happen, Con Ed has extreme resiliency and reliability, but at the same time suffer from poor control. SIVOM built around CWTs is proposed to mitigate this extremely challenging problem.

7.8 Thermal characterization of SIVOM

There is a need for the cooling mechanism to be inert and nonconductive. As part of lab experiments, a few different methods of cooling were investigated. The transformer was rated at 1.66 MW at 2000 A, 60 Hz. It was cooled with a few different methods including fans and oil as part of which several experiments were performed. In the process, SIVOM was exposed to higher current levels with and without any intentional cooling as with the design for industrial applications. Experimental data was obtained during the thermal characterization studies and the results are shown in Figure 99.

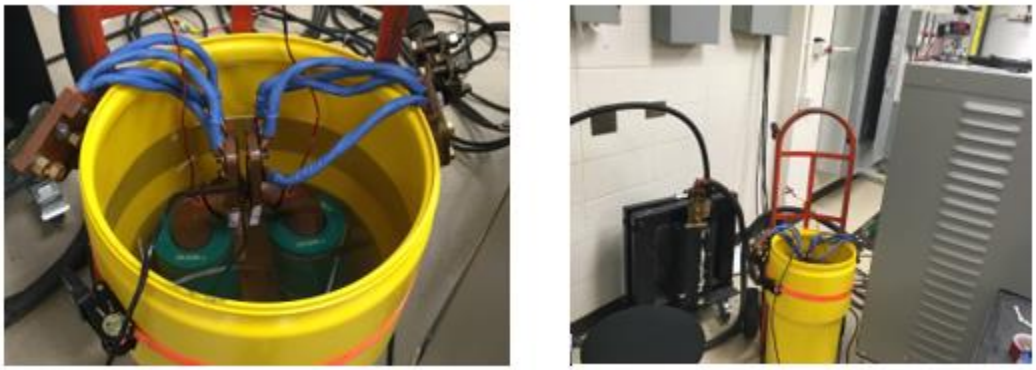

Figure 98 Experimental setup with oil

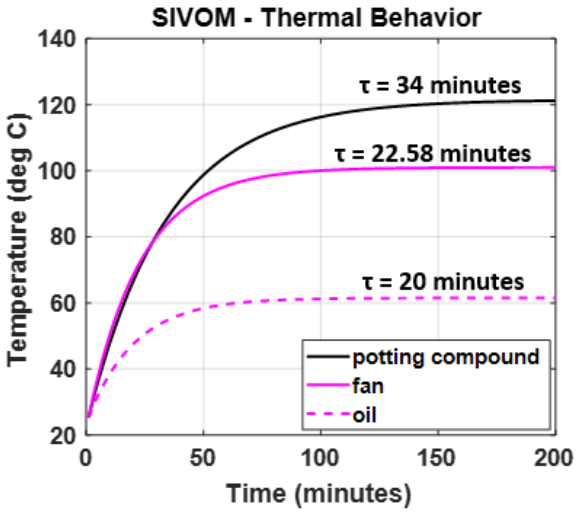

Figure 99 Comparison of thermal performance

The extracted time constant for different cooling methods has been shown in Figure 99. The following table shows a comparison of performance predicted by the model with the data from lab tests.

Table 18 Comparison of thermal model and experimental data

Method of cooling	Lab test (ºC)	Model (ºC)
Potting Compound	117.5 °C	121.5 °C
Fan	102.6 °C	100.877 °C
Oil	61.3 °C	61.48 °C

In addition, the experimental results of thermal performance with oil have been projected to higher current levels as shown below using a mixed model. Temperature measurement

at 500 A, 800 A and 1200 A was obtained to be 31.7 °C, 50.7 °C and 61.3 °C for the inside conductor.

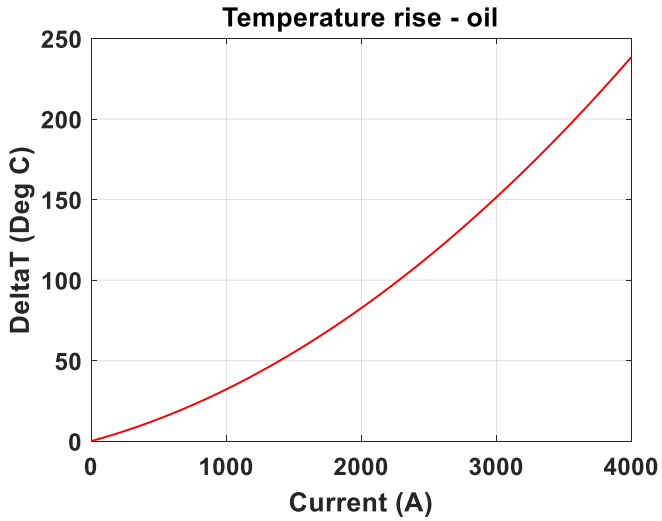

Figure 100 Temperature rise with oil

A comparison of the temperature at 800 A and 1200 A is shown in following figures. The time constant was extracted using Matlab to be 20 minutes for the inside conductor and 25 minutes for the copper tube. The thermal resistance and capacitance for the inside conductor were calculated to be 0.3423 ºC/W and 58.42 J/ ºC

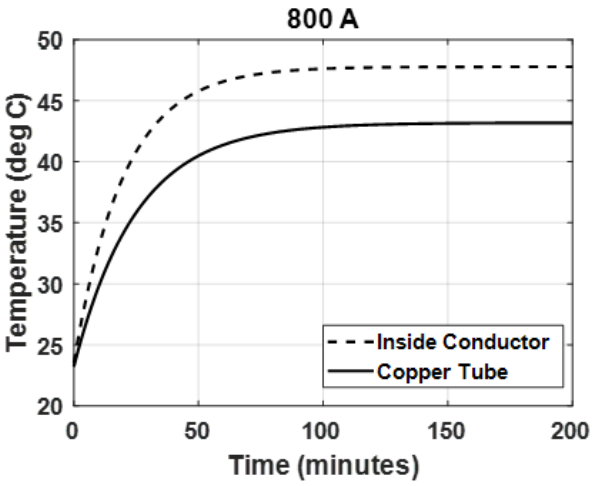

Figure 101 Temperature of inside conductor and copper tube at 800 A

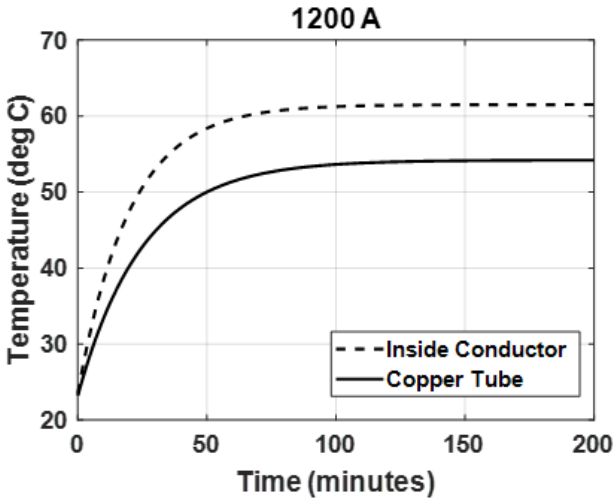

Figure 102 Temperature of inside conductor and copper tube at 1200 A

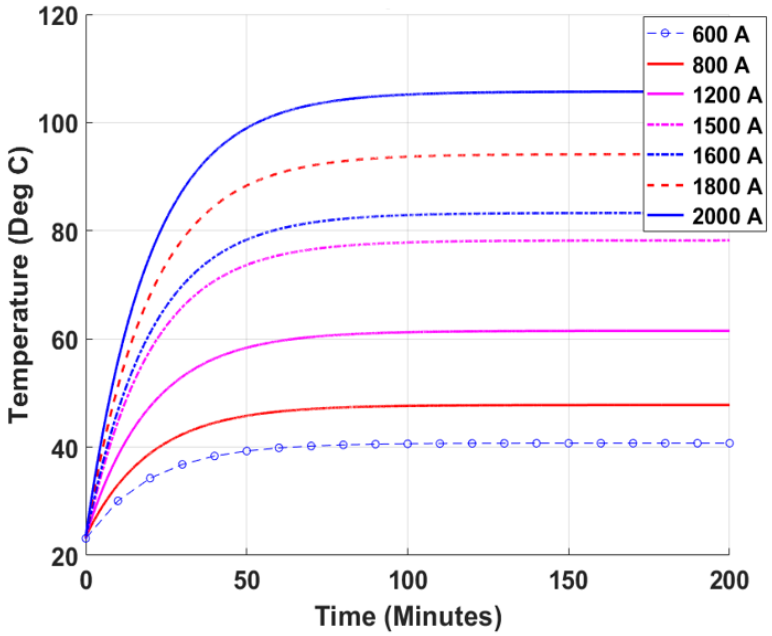

Figure 103 Loading curve with oil (2000 A)

The loading curves at up to 2000 A with oil have been plotted in Figure 103. It may be seen that the temperature of the inside conductor may reach 105.6 ℃ at 2000 A as compared to 40.67 ℃ at 600 A.

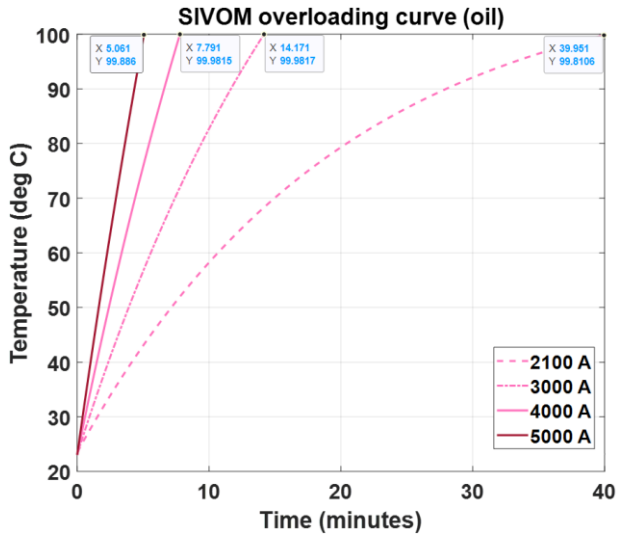

Figure 104 Overloading characteristics up to 5000 A

The overloading characteristics at up to 5000 A is shown in Figure 104. It may be seen that for the temperature of the inside conductor to reach close to 99.88 deg C, it may take 5.061 minutes at 5000 A.

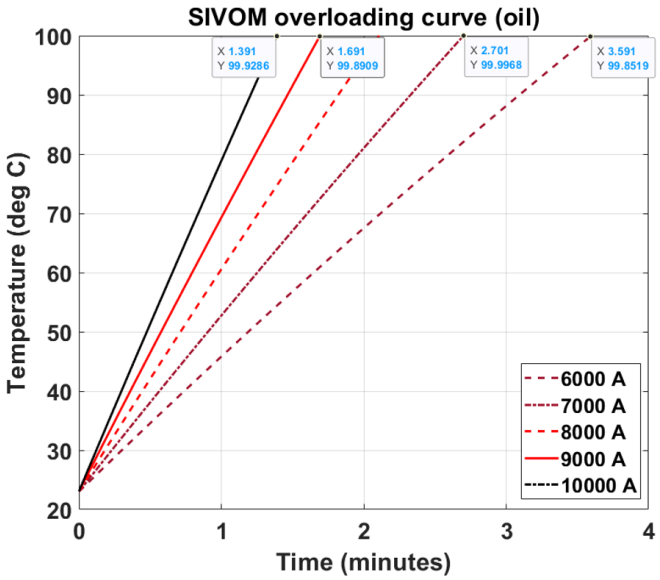

Figure 105 Overloading characteristics up to 10000 A

The overloading characteristics at up to 10000 A is shown in Figure 105. It may be seen that for the temperature of the inside conductor to reach close to 99.92 deg C, it may take 1.391 minutes at 10000 A.

The salient result of the thermal characterization studies is the ability to be able to operate the device with increasing current density. The use of fan or oil has been effective in the removal of air pockets that could be present due to slight device imperfection. The projected results as part of the simulations show that there is significant improvement in performance and concomitant increase in current density without resulting in excessive temperatures. Providing a means to cool the interwinding space is an important means to achieve an optimal design [50]

7.9 Discussion of AC effects

The focus of the thesis is 60 Hz and the associated AC effects may be lower as compared to higher frequencies. A discussion of such effects is provided, and simulations have been shown for comparison.

When alternating current flows in a conductor, it induces an alternating magnetic flux which induces an emf [60]. The emf causes eddy current that flow in the opposite direction to the applied AC current in the interior of the conductor. Eddy current does not provide any useful current flow but may cause additional power loss, which increases the effective resistance for the conductor [60]. Because of eddy current, the current density is maximum at the surface of the conductor and decreases exponentially towards the interior of the conductor. The thickness at which the current density reduces to 1/e of the current density at the surface of the conductor is called skin depth δ. At 60 Hz in copper, the skin depth is about 8.5 mm

$$\text{Skin depth } \delta = \frac{1}{\sqrt{\pi f \mu \sigma}} \tag{49}$$

The increase in resistance is significant for conductors with thickness more than one skin depth. The thickness of the copper tube is 0.3175 cm which is less than the skin depth. The associated losses due to skin effect are minimal. Simulations in Ansys Maxwell have been performed to compare the current density in a coaxial winding transformer at 60 Hz. Results showed that the current distribution is continuous at 60 Hz (Appendix C).

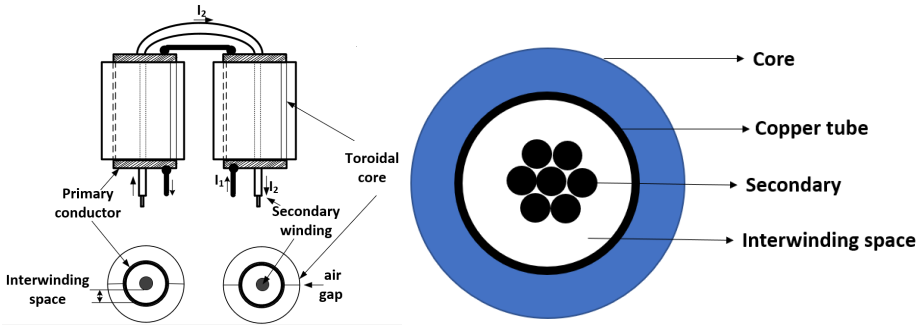

Figure 106 Schematic of a CWT [52]

All power transformers are limited by the ability to dissipate internally generated losses. A transformer with a cooling mechanism may essentially be operated beyond the normal limits of current density, flux density, frequency etc. with the ability to remove device losses [50]

7.9.1 Summary of electrical specifications:

V = 480 V I = 500 A, phase 3, core material: silicon steel, conductor: copper,

temperature ~ 80 deg C, cooling: fan

An important discussion on a CWT made from tubular shells or foil is the large surface area of the conductors as compared to the bundled round conductors. Being able to provide good contact between the heat transfer surfaces, would further allow operation at higher power levels. To maintain low leakage, a lower number of turns is desired, but this may lead to higher magnetizing current. This effect can be minimized by providing an absolute minimum air gap [52] . A calculation is shown to understand the design aspects pertaining to having 4 turns on the outside tube and the impact on ac resistance.

7.9.2 Representative design showing 4 turns in the transformer:

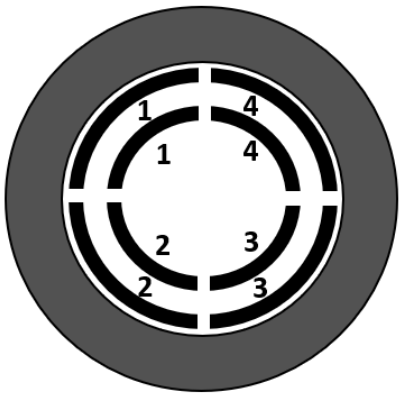

Figure 107 Representative design of a four turn coaxial transformer [52]

Figure 107 shown above is for an arrangement of a 4-turn circular CWT with turns in one layer, an alternative arrangement could have turns in two layers [52]. Each of these would differ in terms of effective resistance and losses, optimal conductor thickness etc. The equation for ac resistance (R_n) of the n_{th} layer per meter of turn length for each winding in the above configuration is given by [52] [60, 61]

$$R_n = C\{(r_{in}B_{in}^2 + r_o B_o^2)F_1(x) - 4\, B_i B_o \sqrt{r_i r_o} F_2(x)\} \quad (50)$$

where $C = \frac{N^2 \rho}{2 I_n^2 \mu_o^2 \delta}$

$$N - number\ of\ segments\ per\ layer, \rho : resistivity, (\Omega m), I_n$$

$$: total\ current\ in\ n_{th}\ layer\ A, \delta - skin\ depth$$

r_{in} – is the radius of the inner surface of the $n_{th} layer, r_o$ is the radius of the outer surface of the $n_{th} layer$, with the magnetic flux density boundary conditions - B_{in} and B_o

$$B_{in} = \frac{\mu_o (n-1) I}{2\pi r_{in}} \quad B_o = \frac{\mu_o n I}{2\pi r_o}$$

$$x = \frac{r_o - r_{in}}{\delta}$$

$$F_1(x) = \frac{\sinh(2x) + \sin(2x)}{\cosh(2x) - \cos(2x)} \quad F_2(x) = \frac{\sinh(x)\cos(x) + \cosh(x)\sin(x)}{\cosh(2x) - \cos(2x)}$$

Assumptions for the calculation shown: copper tube OD: 2" Number of layers = 1, number of segments per layer: 4. Calculation is shown for AC resistance normalized to dc resistance of a copper tube with thickness equal to one skin depth N = 4 in Figure 108

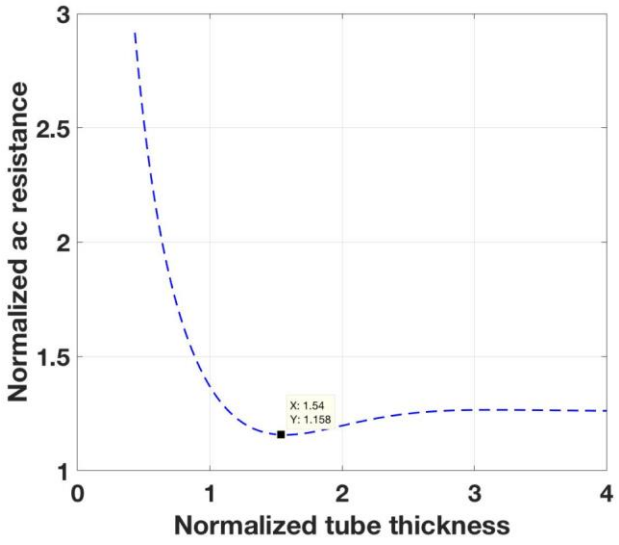

Figure 108 Calculation of AC resistance for a CWT with N = 4

For a CWT, a comparison based on change in the number of layers is discussed below.

Table 19 Normalized tube thickness and AC resistances

Number of layers	Normalized tube thickness	Normalized AC resistance
1	1.562	1.157
2	0.8243	2.02
3	0.6291	2.559
4	0.5423	2.97
5	0.4772	3.276

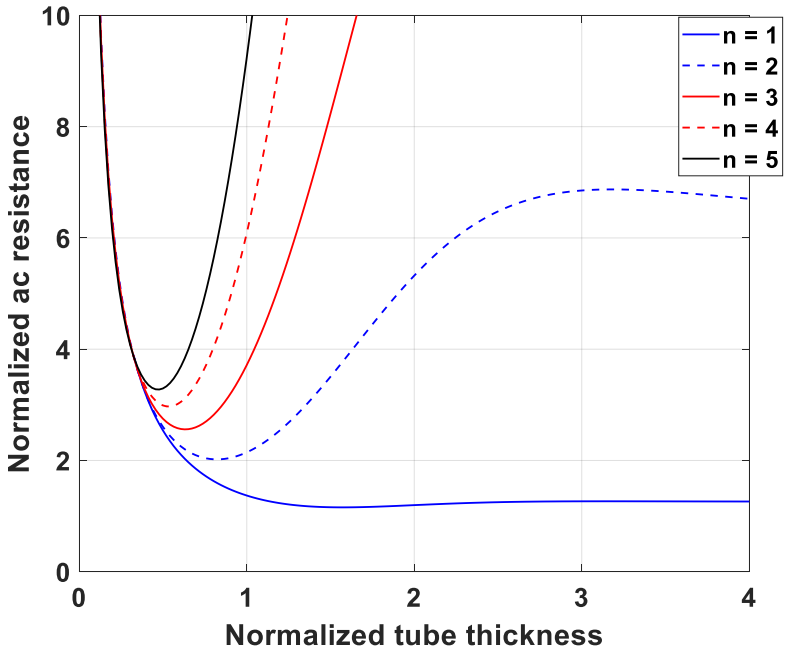

Figure 109 Comparison of AC resistance for a CWT

Figure 109 shows the change in normalized AC resistance as the number of layers is varied from n = 1 to n = 5.

An alternative design option could be based on a hybrid helical-coaxial transformer (CHWT) [61] that may have primary winding coaxial (split primary winding) and the secondary winding is helical. A representative CHWT is shown in Figure 110

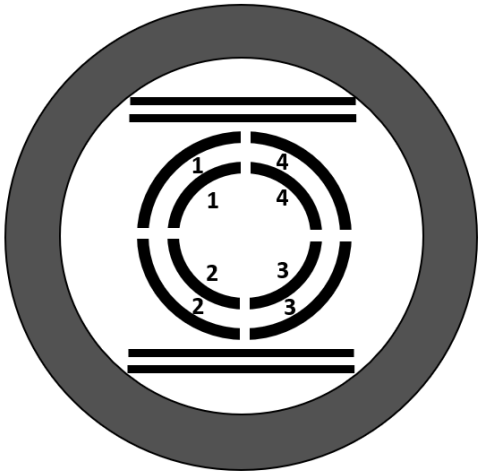

Figure 110 Hybrid helical-coaxial transformer

In such a design the loss in the copper tube may need to be carefully understood [61]. However, the use of foil wound conductors as part of the secondary winding may provide operation at higher power level by providing good thermal contact.

7.10 Losses and thermal characterization of 360 KVA CWT

The transformer dimensions are calculated as shown below. Using equation (17), the core flux area cross section was calculated to be $0.01386\ m^2$. The core is a silicon steel toroid whose length was calculated to be $67.15\ cm$ ($33.5\ cm\ each\ side$) assuming an inner diameter of 5.3975 cm and an outer diameter of 9.525 cm. With a core height of 3.49 cm, approximately 9 cores on each side are required. The core volume was calculated to be 3248.36 cm^3 and the weight of the core was calculated to be 24.85 kg. The transformer length is calculated as one half of the length of the copper tube, which equals 48.53 cm. The outer diameter of the copper tube approximately equals the inner diameter of the core.[51]

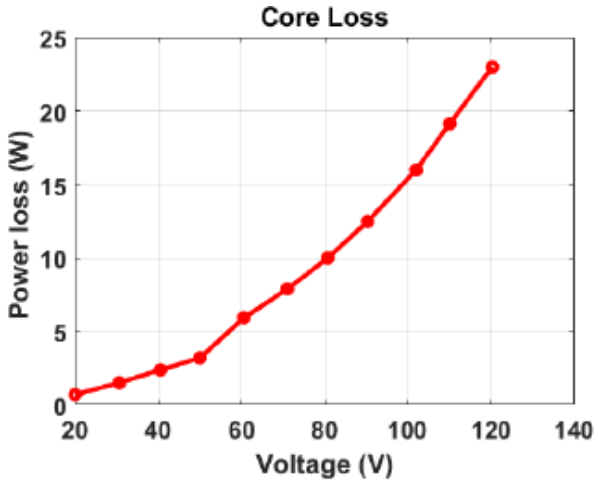

Figure 111 Core loss measurement

The 360 KVA CWT was characterized to extract the losses. The measurement of core loss is shown in Figure 111. Similarly, copper loss measurement was performed. It was observed that the device losses were very low. The copper loss was measured to be $220\ W$ at 1000 A. The leakage inductance was extracted to be $171\ nH$.

A finite element simulation software for thermal simulation solves for the following set of equations discussed in references [59, 62]

$$\rho \frac{\partial v}{\partial t} + \rho\,(v.\nabla)\,v = -\nabla p + \mu\nabla^2 v + \rho g \tag{51}$$

$$\frac{\partial \rho}{\partial t} + \nabla.(\rho\, v) = 0 \tag{52}$$

$$\rho\, C_p \frac{\partial T}{\partial t} + \rho C_p\, v.\nabla T = \nabla.(k\nabla T) + Q \tag{53}$$

Where the temperature at a point is T, p is the pressure, ρ is the density, v is the velocity field, the heat generated is given by Q, C_p is the specific heat capacity and k is the thermal conductivity. Equation (51) is the Navier-Stokes equation, equation (52) is the continuity equation and equation (53) is the energy equation. The solution to a highly non-linear problem of natural convection is time consuming and reference [59] has discussed that a finite element model with second degree elements may not converge after hours of simulation or several iterations with state of the art powerful computers and that there is a need for a model to be simple and accurate to yield the temperature without being computationally intensive.

A comparison of experimental measurement and ideal thermal model investigated in this thesis for the coaxial transformer is shown Figure 114. Experiments in the lab were conducted on the CWT prototype at various power levels. In Figure 112 shown below, arrows point to the location of the thermocouples at five locations. The experimental data has been plotted along with the ideal thermal model for the transformer. The temperature

was recorded in steps of 10 minutes until steady state. For the inside conductor, the temperature measurement at location 1 and 5 were very similar.

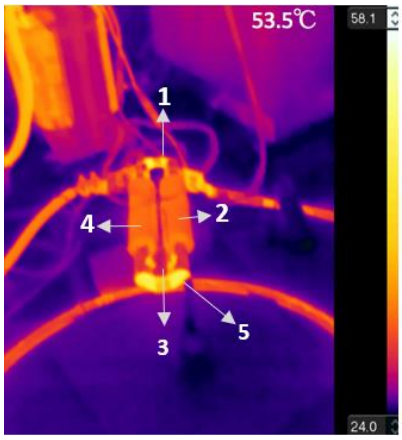

Figure 112 Placement of thermocouple in the prototype

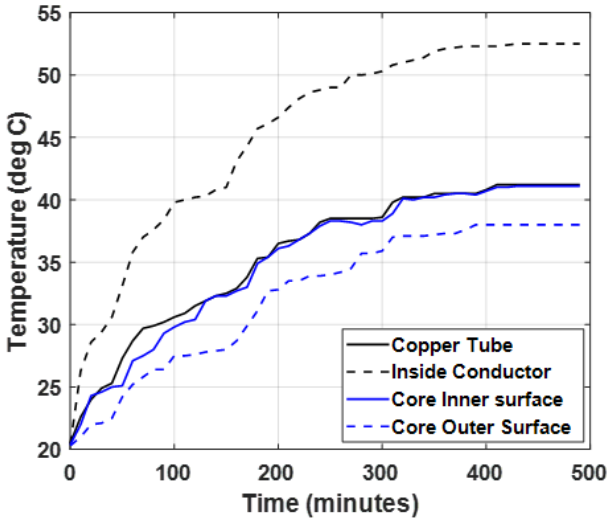

Figure 113 Thermal characterization of the coaxial winding transformer at 500 A

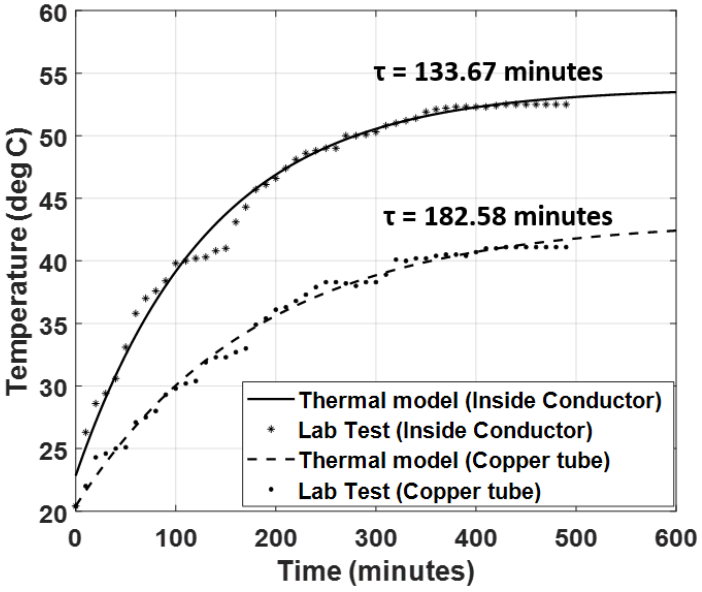

Figure 114 Comparison of thermal model and lab measurement

The hot spot temperature is located at the inside conductor. From Figure 114 it may be observed that the thermal model led to 53.83 °C for the inside conductor and 43.27 ºC for the outside conductor. The thermal resistance and thermal capacitance for the inside conductor were extracted to be 1.156 $℃/W$ and 115.63 $J/°C$. For the outside conductor, the thermal resistance and thermal capacitance were extracted to be 4.167 $℃/W$ and 43.81 $J/°C$

The slope of the plot (regression coefficient) between temperature (℃) and the total loss in (W) yields the thermal resistance. Knowing the time constant (shown in Figure 114) and the thermal resistance, the thermal capacitance may be calculated shown in Table 20. The coefficient of determination was extracted from MATLAB to be 1, implying that most of the variability in the response is explained by the regression model. [63]

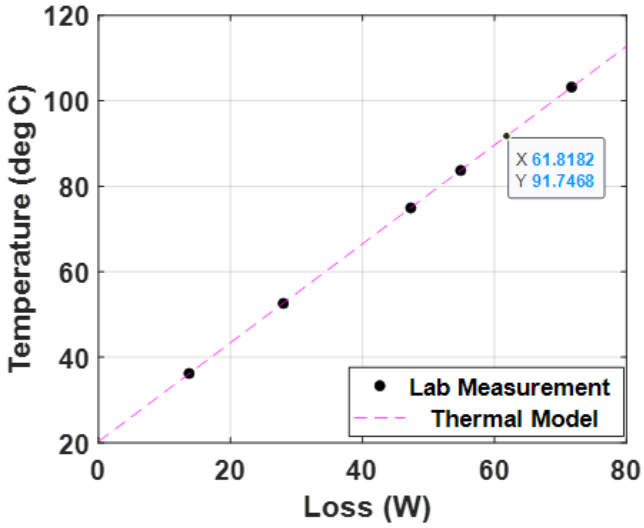

Figure 115 Comparison of lab measurement and thermal model for inner winding

Using the thermal model, the allowable loss (W) in the inside conductor for a change in ambient temperature is shown in Figure 116 for the given operating conditions, that may lead to an operating temperature of 105 ºC.

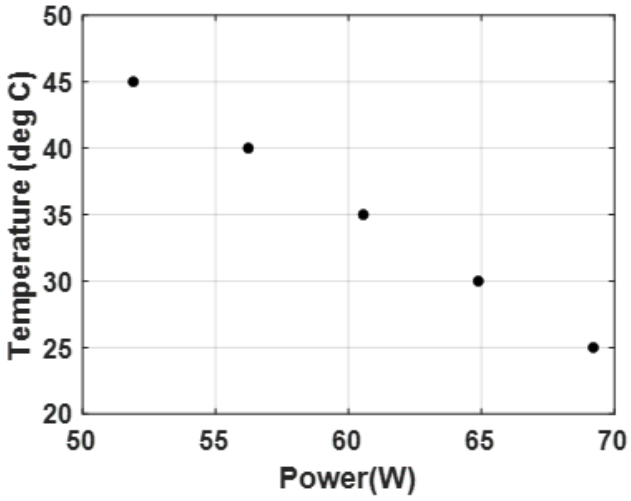

Figure 116 Loss in the inside conductor and ambient temperature

Furthermore, the thermal model is applied to extract the temperature rise for the inside and outside conductor shown in Figure 117. The results of the thermal model are summarized as a heatmap in Figure 120

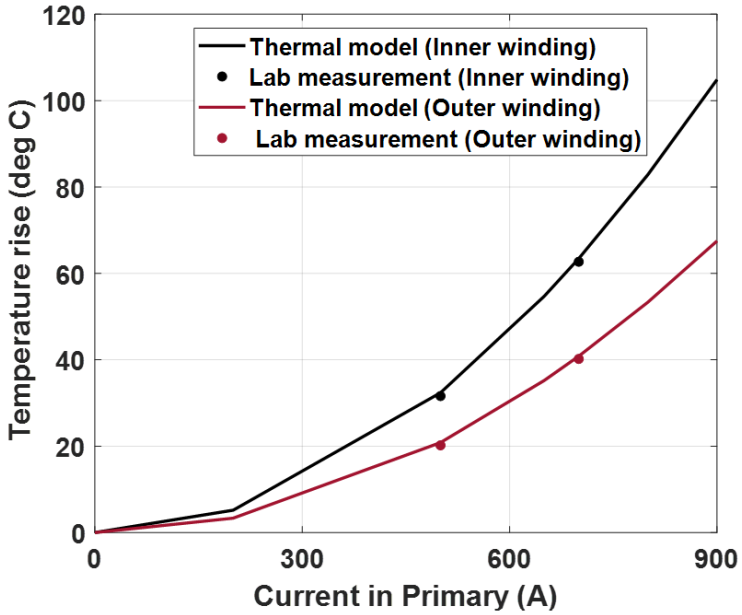

Figure 117 Temperature rise for inside and outside conductor

The results of thermal characterization are summarized below :

Table 20 Thermal resistances and capacitances of the coaxial transformer

Device Component	Thermal resistance °C/W	Thermal Capacitance J/°C
Inside Conductor	1.156	115.63
Outside Conductor	4.167	43.81

Table 21 Thermal characterization at 700 A

Copper tube	61.2 deg C
Litz Wire	83.7 deg C
Inner surface of core	61 deg C
Outer surface of core	56.2 deg C

Table 22 Thermal characterization at 500 A

Copper tube	41.2 deg C
Litz Wire	52.6 deg C
Inner surface of core	41.1 deg C
Outer surface of core	38 deg C

The thermal performance of the coaxial transformer with natural convection is simulated using the mixed model approach based on the data shown in Table 21 and Table 22 for the inside conductor shown in Figure 118. It was observed that continuous operation of up to 800 A may lead to a temperature of 103.2057 ºC. A short-term operation at 1000 A for 2 hours and 6 minutes, may lead to a temperature of 99.81 ºC and at 1100 A for 1 hour and 33 minutes, may lead to a temperature of 99.4751 ºC.

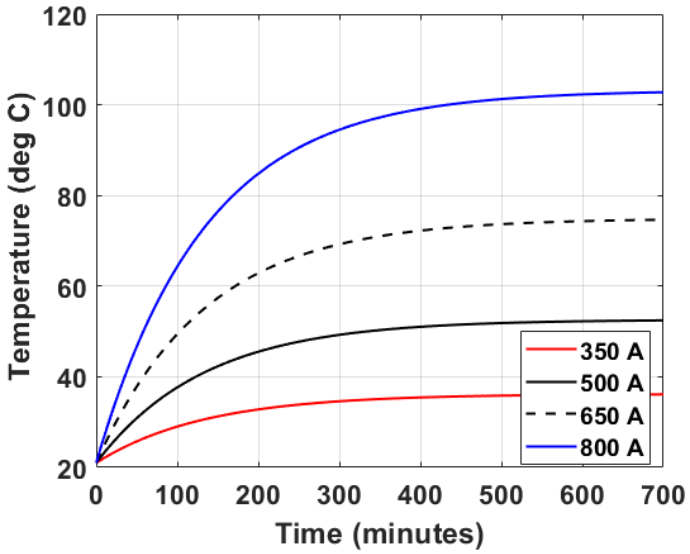

Figure 118 Thermal performance of the coaxial winding transformer

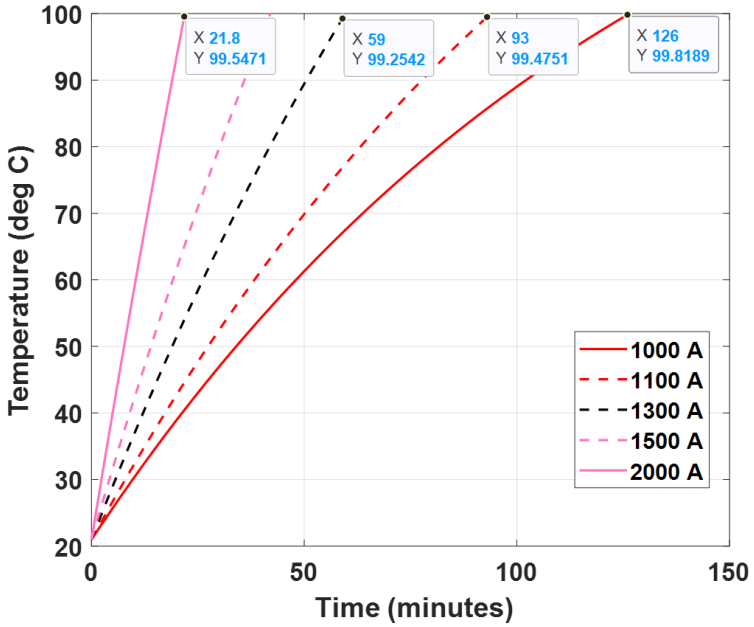

Figure 119 Thermal overloading characteristics of the CWT

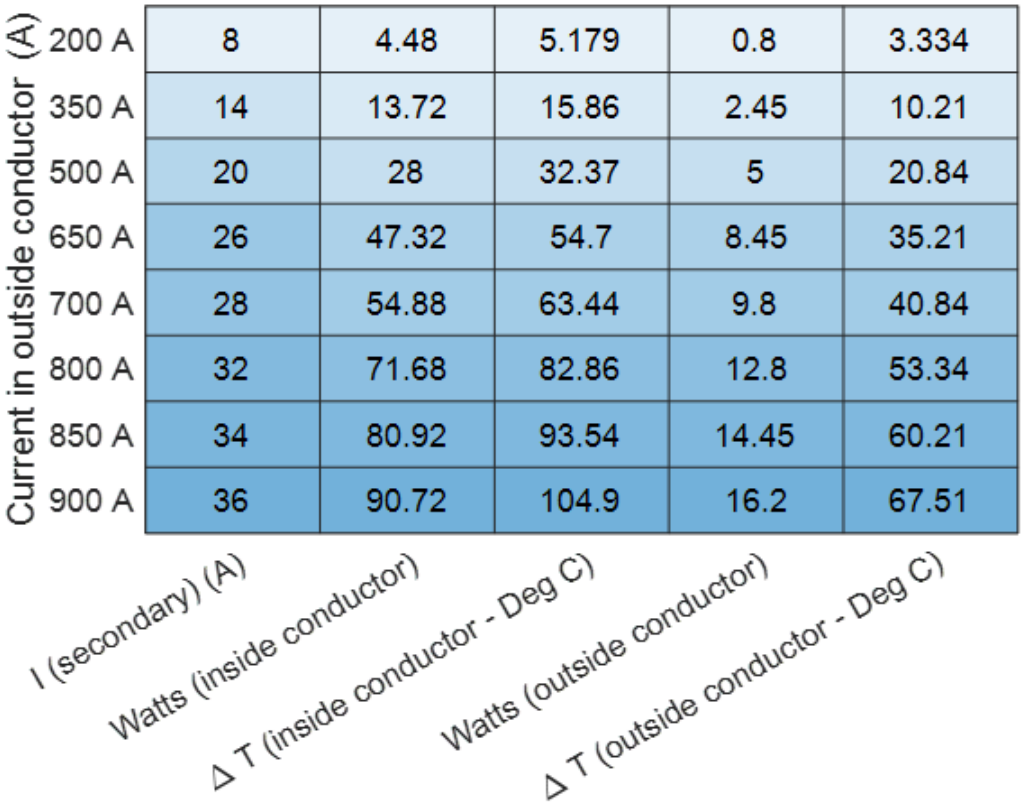

Figure 120 Thermal model represented as a heatmap

The thermal model is used to extract the temperature of inner winding for continuous operation summarized in Figure 121

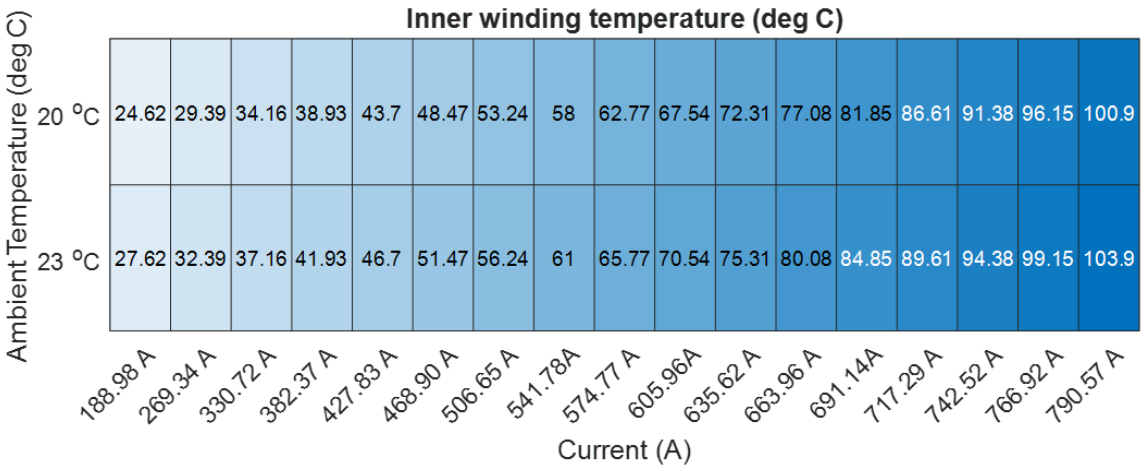

Figure 121 Inner winding temperature extracted from thermal model

One of the applications of the thermal model could be to understand the expected lifetime of the device. Based on the Arrhenius model [64], the per unit life may be calculated as

$$Per\ unit\ life = A \exp\left(\frac{B}{T + 273}\right) \tag{54}$$

The constants in the above equation have been chosen as discussed in reference [64]. B is the aging rate constant and A is selected such that at temperature T = 110 °C, the per unit life equals one. For the device, the per unit life at different current levels (for continuous operation) is shown in Figure 122

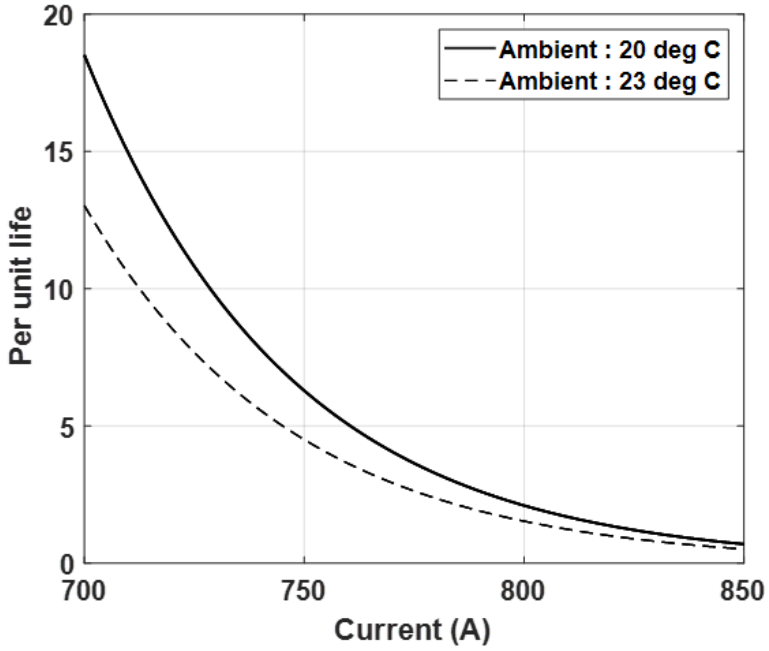

Figure 122 Per unit life at different current levels

Figure 123 shows the plot of current versus time. 24 randomly generated current values at each hour have been plotted. The thermal model was used to calculate the temperature of the inner winding pertaining to each of these conditions. The resulting temperatures have been plotted in Figure 124 and the average temperature at each hour is shown in Figure 125. The ambient temperature was chosen to be 23 deg C.

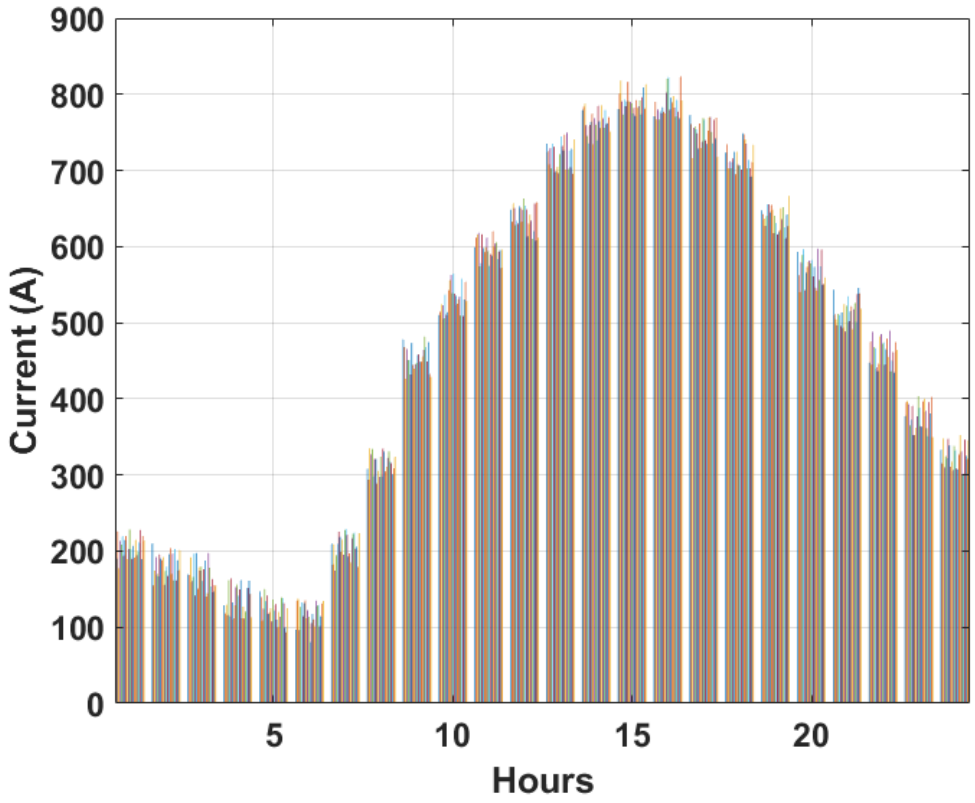

Figure 123 Current at each hour obtained in MATLAB

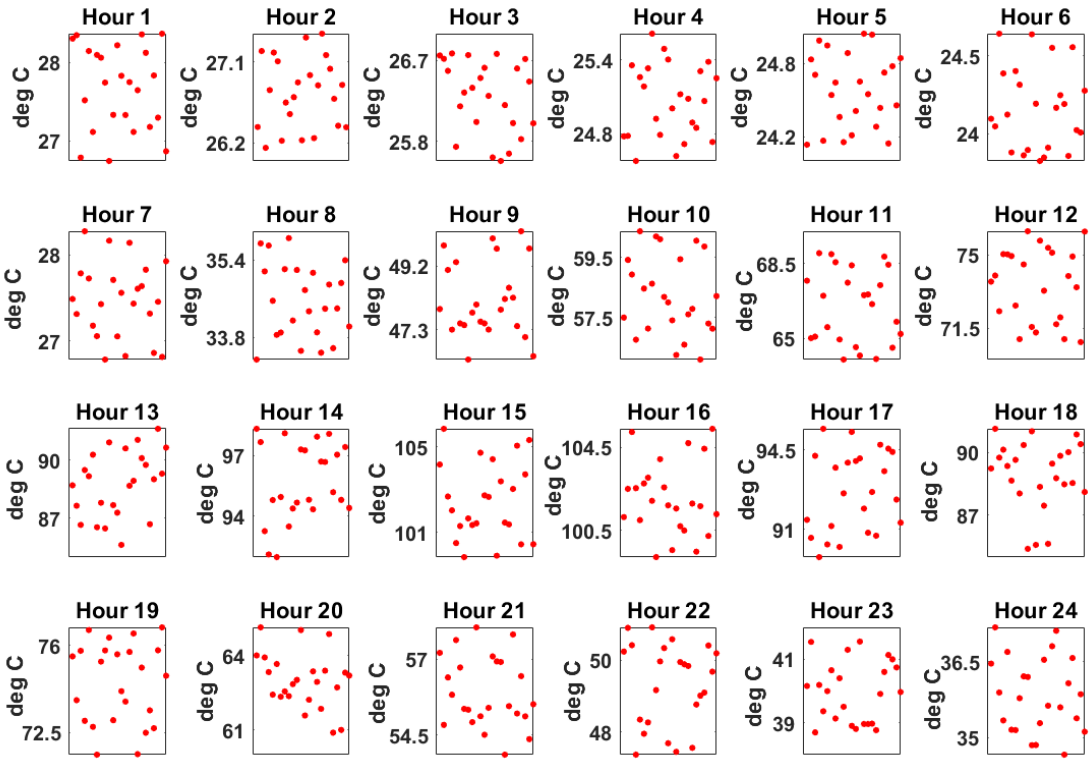

Figure 124 Temperature of inner winding for each scenario

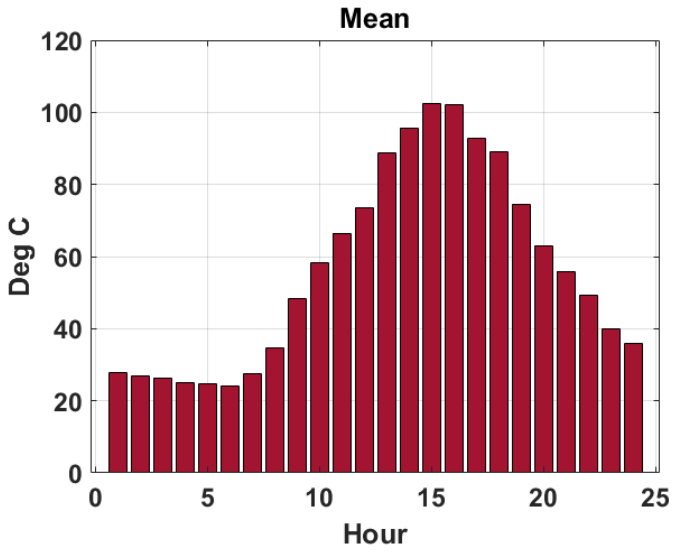

Figure 125 Average temperature for each of the scenarios

For the second scenario, the following distribution (that resembles a truncated normal distribution) shown in Figure 126, was obtained in MATLAB where a 1000 data points of current have been shown in the form of a histogram with 50 bins. Pertaining to each of these data points, the thermal model was used to obtain the inner winding temperature (at 23 °C ambient temperature) and the resulting per unit lifetime, shown in Figure 127 and Figure 128.

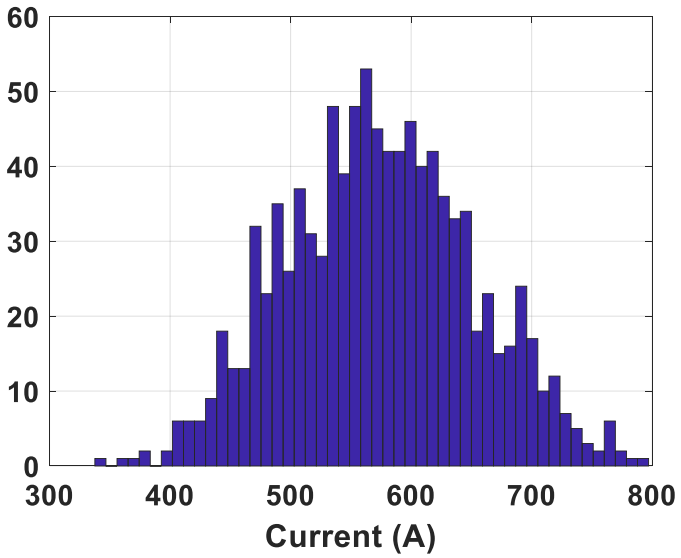

Figure 126 Current distribution obtained in MATLAB

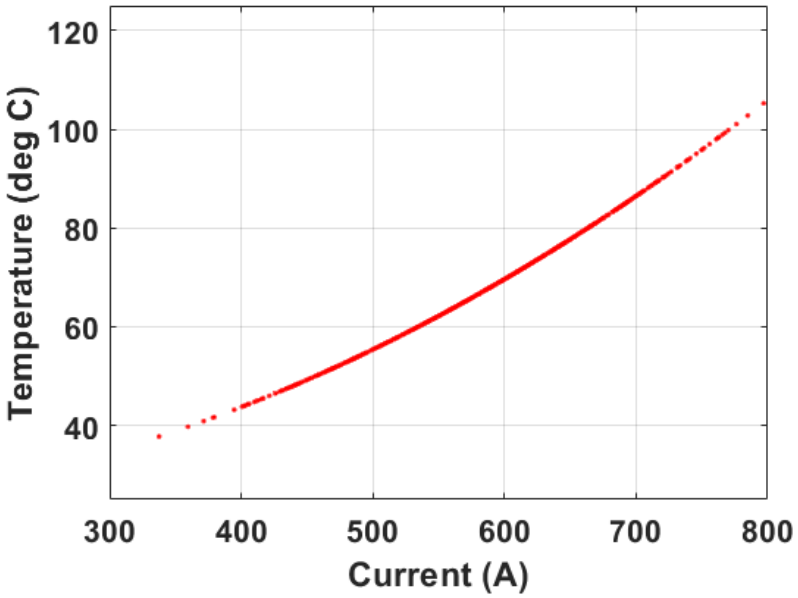

Figure 127 Inner winding temperature for each of the 1000 data points of current

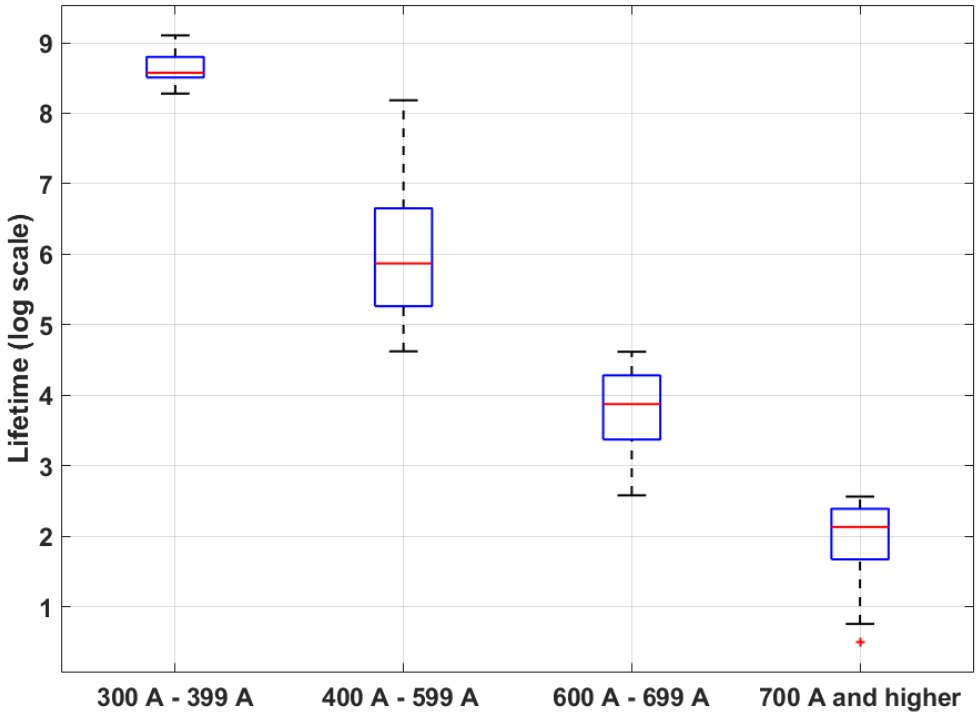

Figure 128 Per unit lifetime shown in logarithmic scale

A reasonable approach towards optimizing the device performance could be obtained with a cooling mechanism. A comparison of different cooling methods has been investigated at high power. Detailed thermal model and projections based on experimental data for continuous operation along with overloading conditions (at up to 10000 A) have been discussed. These methods have been effective in removal of air pockets that may be present in the device. Furthermore, experimental results of losses and discussion of AC effects due to different device configurations has been provided.

CHAPTER 8. SUMMARY OF CONTRIBUTIONS AND FUTURE WORK

8.1 Introduction

The key contributions of this work are explaining from fundamental principles the quantification of CVR factor with industrial loads and the important requirements of a device for voltage management. The use of coaxial winding transformers at high power has been discussed in detailed. Simulation and experimental studies have been shown. The following are the important conclusions of the work.

8.2 Conclusions

- Chapter 2 explains the problem statement and chapter 3 discusses a detailed survey of literature.
- With the mix of loads that change throughout the day, the CVR factor of an industrial plant changes. A method to extract CVR factor of a plant was discussed and the approach was validated through simulations and experiments that showed that voltage changes caused by changes in load have a negative correlation and load changes caused by changes in voltage have a positive correlation. The method was applied to voltage and power measurements from an industrial plant and the CVR factor was extracted to be 1.1.
- The detailed requirements of a device for voltage management have been explained in chapter 5. They are dynamic control – voltage sags, fail normal capability, fault current handling capability, efficiency, and thermal management.

- A voltage management device based on coaxial winding transformers is introduced in chapter 6. Detailed simulation and experimental results are discussed pertaining to the requirements in chapter 5.
- The ability of the device to inject or bypass a voltage at up to 1000 A has been shown through experimental results. Results showed a change in current from 1000 A to 970 A for a -1 V injection. Experimental results of dynamic response showed that a change in voltage of 2.8 V may be achieved for the device to transition from zero voltage injection mode to voltage boost mode. Similar response time can be achieved for the device to transition from voltage reduction mode to fail normal mode.
- The experimental results from high current impulse test showed the ability of the device to be robust to handle tens of kA. With the experimental setup in the lab, a 10 ms pulse of 530 A was applied on the low current side of the device, which led to 26000 A on the high current side. An extremely small movement of 0.04 mm was measured between the two terminals of the outside conductor using laser interferometer-based displacement sensors. Since most of the forces act on the system during the first peak, this test gives a good validation to the ability of the device to be robust to handle the force. Furthermore, detailed simulation and experimental results showed that in the event of an open circuit situation on the secondary side, about 10 V at nominal conditions of 2500 A and 12 V under conditions of fault may be injected on the primary side.
- Measurement of core temperature at different current levels was performed by circulating current on the primary winding and having the high voltage side open.

The results showed that the fans in the device could assist in cooling the core in an open circuit situation and to able to work on the device installed in a system. Saturation leads to minimal impact to plant operations in the event of a fault within the device.

- The efficiency of the device was found to be over 99.8%. Experimental measurement of temperature was done to understand the thermal behavior and the overload capability of the SIVOM system. It was found that continuous operation of up to 2500 A may be possible that could lead to a final temperature of 95 deg C with the fans. Similarly, a short-term overloading operation of 3000 A for 5 minutes is permissible, without affecting the enameled wire temperature rating.
- Chapter 7 focuses on thermal characterization and losses. Experimental measurement and modeling of temperature, different ways of cooling and measurement of losses have been discussed. The results showed that a reasonable approach towards optimizing the device performance could be obtained with a cooling mechanism. The various methods of cooling have been shown to be effective. The projected results as part of simulations (at up to 10000 A) show that there is significant improvement in performance and concomitant increase in current density without resulting in excessive temperatures. Furthermore, detailed thermal models based on linear regression have been applied to extract the parameters and resulting temperature rise.

8.3 Publications

- S. Jayaraman, M. Miranbeigi, R. P. Kandula and D. Divan, "Improving Energy Efficiency and Productivity at Industrial Plants Using Dynamic Voltage

Management," in IEEE Transactions on Industry Applications, vol. 56, no. 2, pp. 1250-1257, March-April 2020.

- S. Jayaraman, M. Miranbeigi, P. Kandula, T. Grant and D. Divan, "Reducing Energy Consumption in Industrial Plants Using Behind the Meter Conservation Voltage Reduction," 2018 IEEE Energy Conversion Congress and Exposition (ECCE), Portland, OR, 2018, pp. 4791-4798.

- S. Jayaraman, M. Miranbeigi, P. Kandula and D. Divan, "Improving Energy Efficiency and Productivity at Industrial Plants Using Dynamic Voltage Management," 2019 IEEE Industry Applications Society Annual Meeting, Baltimore, MD, USA, 2019, pp. 1-8.

- Jinsiwale, Rohit, Sathish Jayaraman, Rajendra Prasad Kandula, Frank Lambert, Deepak Divan, Andrew Reid, and Peter Day. "Implementing volt-Var control in meshed low voltage grids." In 2018 IEEE PES Innovative Smart Grid Technologies Conference Europe (ISGT-Europe), pp. 1-6. IEEE, 2018.

Part of the results from chapter 7 will be submitted to a journal that is being prepared.

8.4 Recommendations for future work

- This thesis has shown based on data from a plant the quantification of CVR factor. An experimentally validated approach was applied. Some references have pointed out to the ability of machine learning techniques such as neural networks that could be used as part of load modeling [65] and may be investigated further.

Furthermore, this thesis has taken a detailed experimental approach that may provide an understanding of load to voltage sensitivity. Some references have discussed effects of weather or seasonal effects that may be useful to investigate further. A good example of such a load could be residential air conditioners or heating loads depending on the month or time of the year [11].

- In this work electromechanical relays have been used for transition from negative injection to positive injection. Early simulation and experimental results suggested the use of SCRs instead of electromechanical relays could be possible. A future work could investigate further and understand the issues that may be of importance at higher power levels.
- SIVOM in utility and industrial applications have been discussed in this work. Analysis and experimental data from three coaxial transformers have been discussed. The ability of the device to inject a voltage has been shown as part of this thesis. While the design and build of a system with nine transformers in a three-phase system is non- trivial and challenging, which may also involve a detailed design of control and thermal management strategies along with the ability to estimate CVR factor, this thesis is a first step towards the use of coaxial winding transformer for voltage management. Additional design considerations in such a system may be investigated.
- Reference [66] has discussed possible improvement to ZIP load model, commonly represented by scalar coefficients corresponding to the constant impedance, constant current and constant power component. Recently there has been a gradual

shift from incandescent lamps to more efficient LED lamps that resemble constant power loads as well as compact fluorescent lamps (CFLs). The hypothesis discussed in reference [66] that the change to more efficient constant power loads may possibly increase line losses there by affecting to some extent the perceived benefits of conservation voltage reduction needs to be investigated further. In addition, both LEDs and CFLs have been discussed to be sources of harmonic currents in reference [66]. To accurately quantify the effects of technical losses associated with these load types, it may be required to incorporate the current harmonic distortion component. A future work could investigate the effects of voltage reduction in a system with high level of harmonic pollution through the use of ZIP models for active and reactive power that takes into consideration the effects of harmonic distortion.

- As detailed in the literature survey, there may be voltage management devices in a system such as voltage regulators, capacitor banks as well as tap changing transformers. Reference [13] has suggested that one of the technical barriers towards voltage management could arise due to the lack of coordination between existing devices to reduce voltage effectively, which may be investigated further as part of future work. A detailed simulation study associated with the potential impact of failure of one or more devices as well as being able to understand how some of these may interact with each other in a system could be investigated further. For example, reference [19] has discussed some issues surrounding the interaction of capacitor banks with upstream voltage regulators and coordination between upstream and downstream voltage regulators.

APPENDIX A. CALCULATION OF CVR FACTOR

Table 23 Calculation of average weekly and annual savings

hour	AVERAGE CVR	AVERAGE LOAD	Watts * hours consumed (KWh)		Energy savings = delta V (assuming 5% yields the CVR factor) * KW *CVR % Savings
0	1.476053064	18.1969115	18.1969115	18.1969115	1.342980349
1	1.476053064	18.1969115	18.1969115	18.1969115	1.342980349
2	1.62541248	15.735103	15.735103	15.735103	1.278801639
3	0.967841408	13.091661	13.091661	13.091661	0.633532581
4	1.618925095	10.73723933	10.73723933	10.73723933	0.86913931
5	1.119692725	25.704314	25.704314	25.704314	1.439046669
6	0.87988544	27.90846375	27.90846375	27.90846375	1.227812546
7	0.43987328	38.5966525	38.5966525	38.5966525	0.848881807
8	0.43987328	38.5966525	38.5966525	38.5966525	0.848881807
9	1.090894485	40.1243124	40.1243124	40.1243124	2.188569555
10	0.828052555	42.95828333	42.95828333	42.95828333	1.778585814
11	0.492796473	39.04374	39.04374	39.04374	0.962030869
12	1.66116199	34.89869	34.89869	34.89869	2.898618867
13	1.069635652	26.640787	26.640787	26.640787	1.424796779
14	0.492796473	38.08212	38.08212	38.08212	0.938336721
15	0.29051045	28.37564667	28.37564667	28.37564667	0.412171095
16	1.235895751	8.022046	8.022046	8.022046	0.495720628
17	0.793698245	16.467349	16.467349	16.467349	0.6535053
18	1.08071114	24.3522292	24.3522292	24.3522292	1.315886269
19	1.380312638	16.46728233	16.46728233	16.46728233	1.136499896
20	1.165693075	21.51617	21.51617	21.51617	1.254062518
21	1.32734673	15.8850916	15.8850916	15.8850916	1.05425122
22	1.222639152	18.9484575	18.9484575	18.9484575	1.1583563
23	1.222639152	18.9484575	18.9484575	18.9484575	1.1583563
		TOTAL KWH SAVED (1 DAY)			28.66180519 saving :
		total KWH (1 day)			597.4945716
		TOTAL KWH SAVED (5 DAY)			143.3090259
		TOTAL KWH SAVED (1 YEAR)			7452.069349
		Cost savings for this plant (total energy saved 1 year * 12 cents)			$900
		total energy cost (today energy 1 day * 5 days * 52 weeks *12 cents)			18641.83063
		Energy savings % (total energy savings 1 day / total energy 1 day)			4.796998425 percentage
		CVRF			0.959399685
					18641.83063

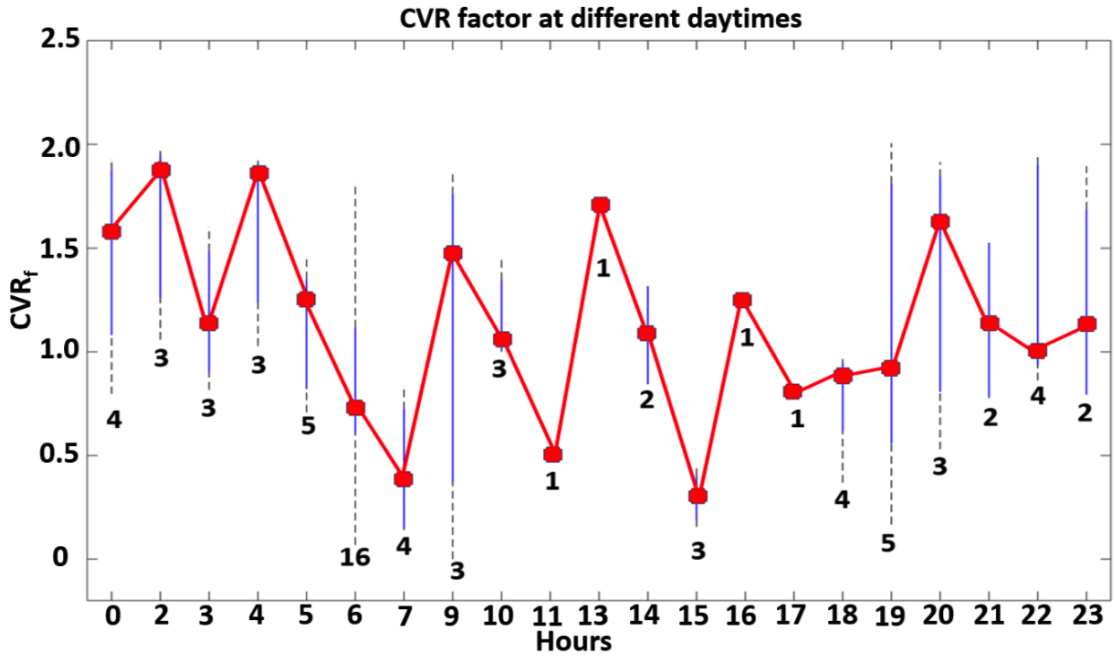

Figure 129 CVR factor at different daytimes

Extracted CVR factor at different times of the day is shown in Figure 129

APPENDIX B. CORE LOSS IN AN OPEN CIRCUIT SITUATION ON HIGH VOLTAGE SIDE

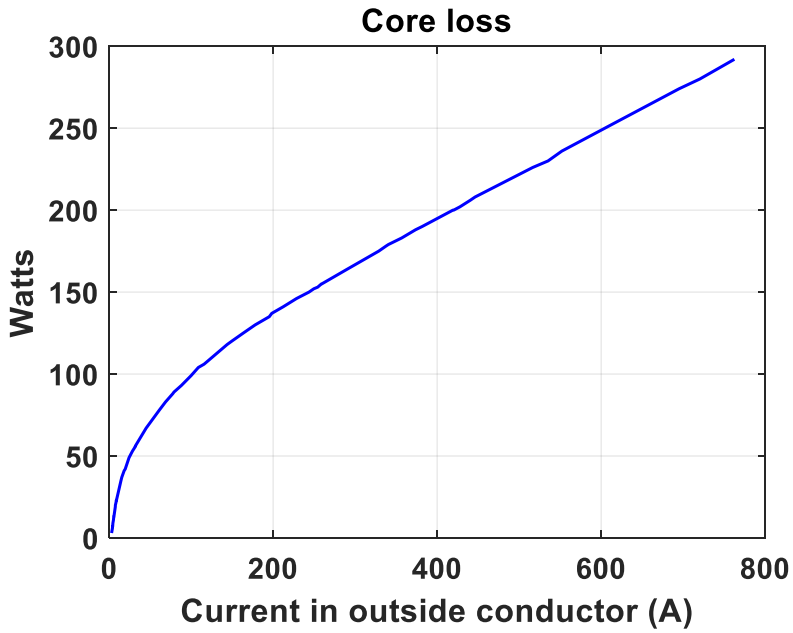

Figure 130 Measurement of core loss under open circuit situation

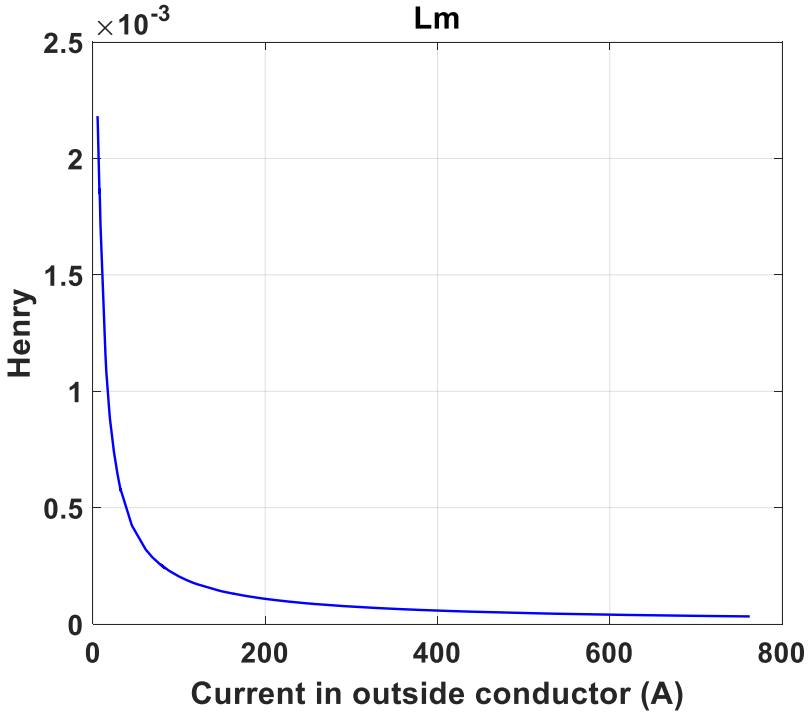

Figure 131 Measurement of inductance under open circuit situation

Additional experimental data under an open circuit situation on the high voltage winding have been shown in Figure 130 and Figure 131

APPENDIX C. SIMULATION OF COAXIAL WINDING TRANSFORMER

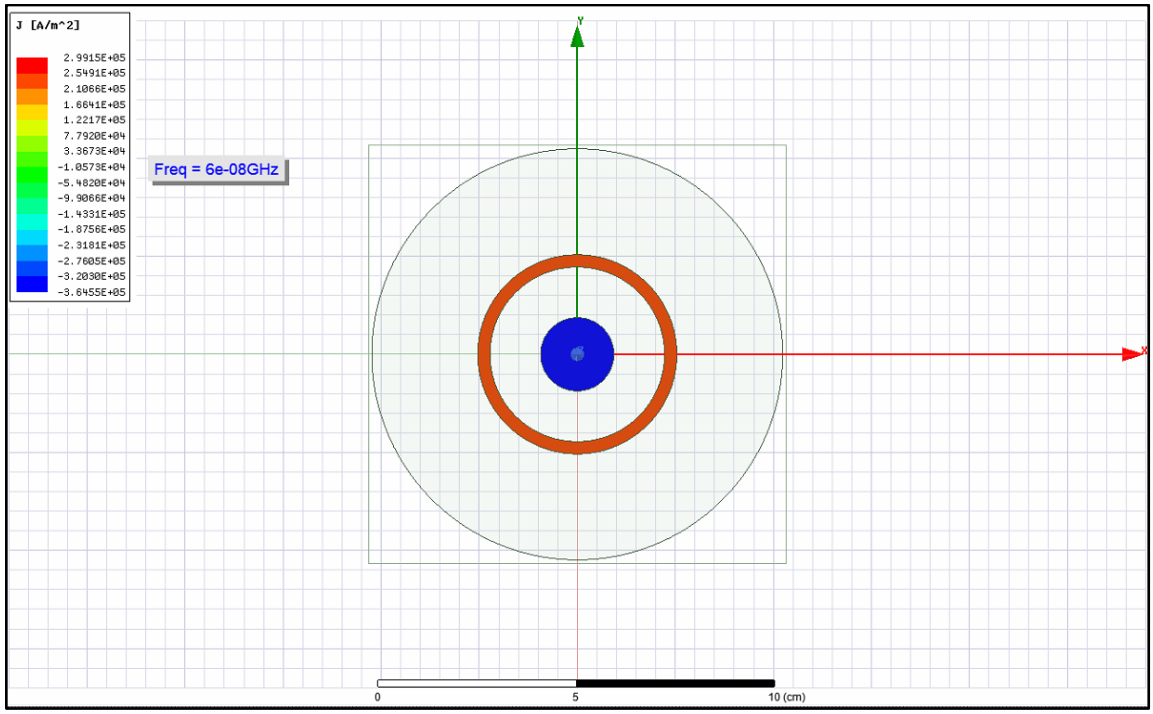

Figure 132 Simulation of current density in a CWT with equal excitation on inside and outside conductor at 60 Hz

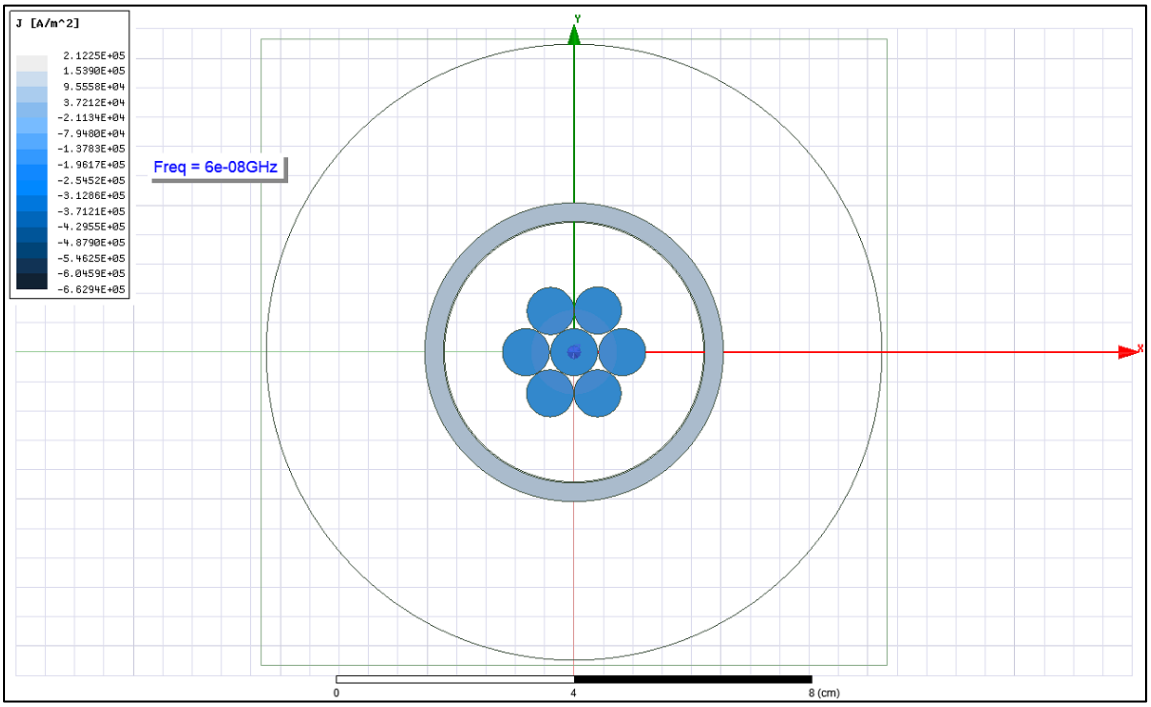

Figure 133 Current density in solid conductor at 60 Hz

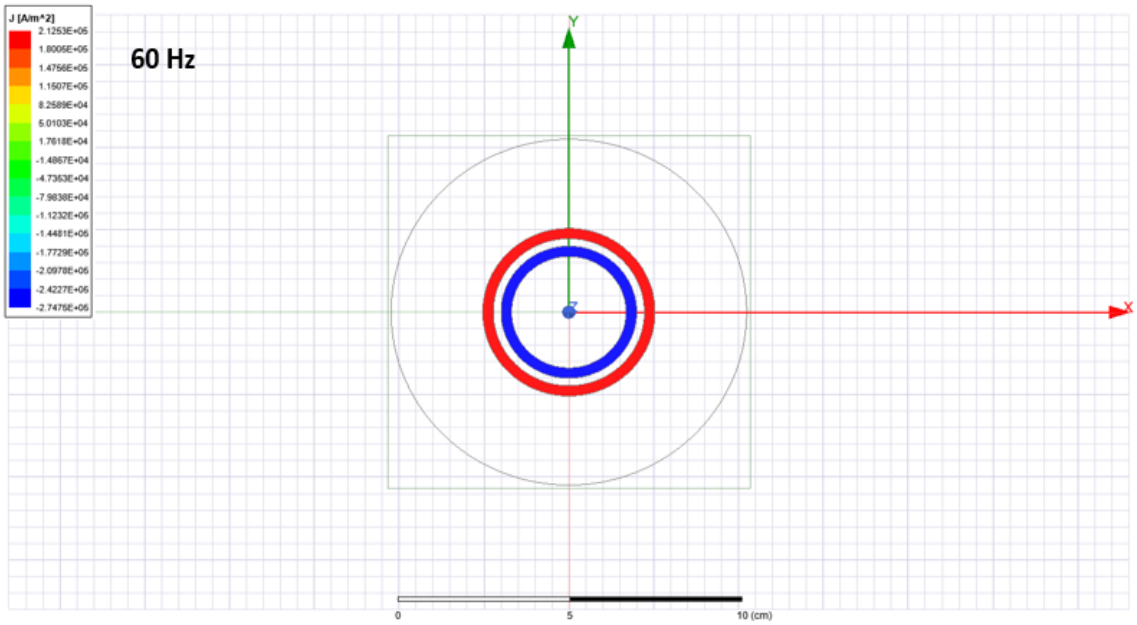

Figure 134 Simulation of current density in a coaxial transformer with a tubular inside and outside conductor at 60 Hz

Reference [60] has discussed that a coaxial winding transformer with a tubular inside conductor is rarely used as the cross sectional area of the inner conductor may be less than that of the outside conductor. Furthermore, alternative designs that may provide improved design flexibility have been discussed in reference [60] that may have concentric copper tubes connected in series. This could lead to multiple turns on the outside conductor represented in Figure 135.

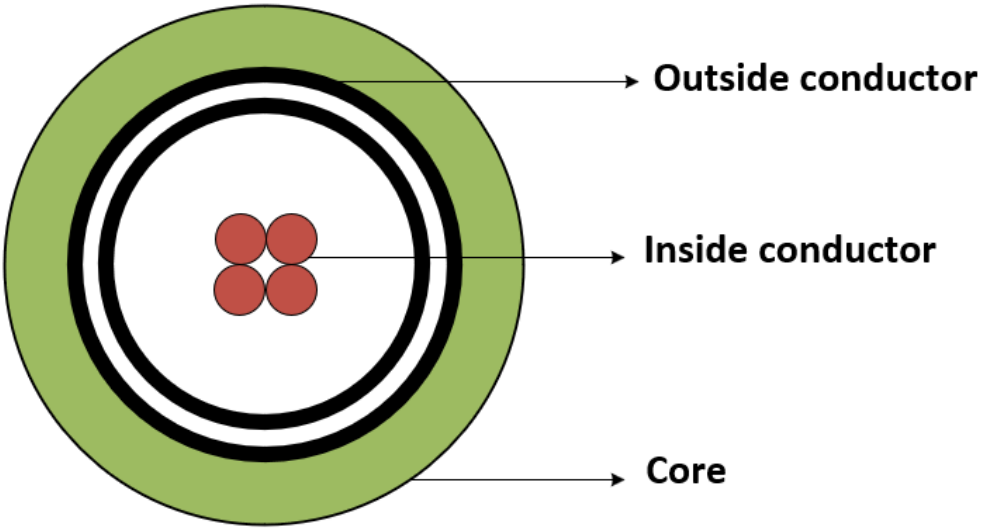

Figure 135 Coaxial winding transformer with concentric copper tubes (primary) and inner conductor

A representative system is simulated in Ansys Maxwell. Two turns on the inside conductor and outside conductor are shown in Figure 136 at 35 A on inside and outside conductor. Simulation result at 60 Hz is shown

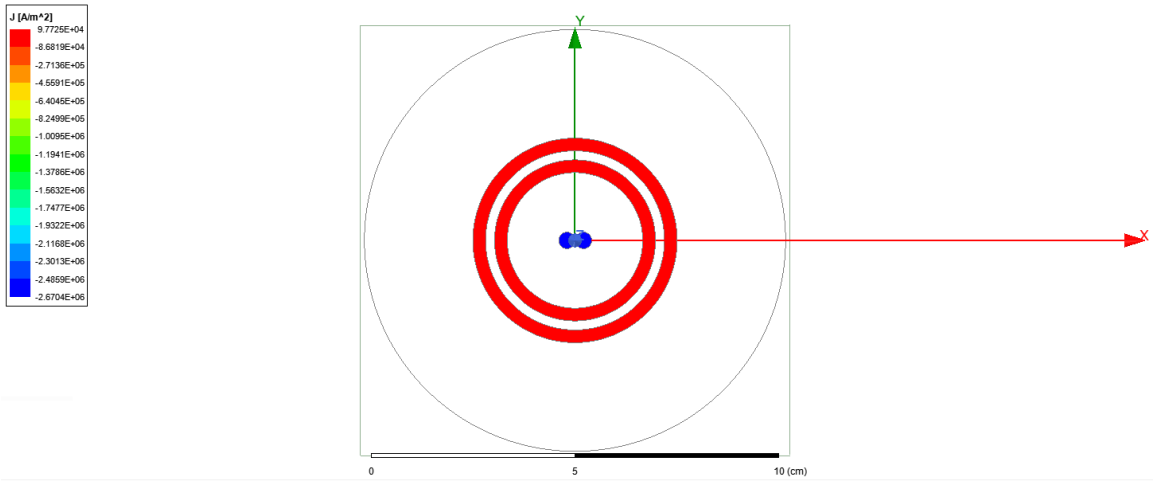

Figure 136 Simulation of current density in a coaxial transformer with two turns on the inside and outside conductor.

Figure 137 shows Ansys simulation of a representative coaxial winding transformer. The current in the inside conductor is 30 A and on the outside conductor is 20 A. Simulation result at 60 Hz is shown.

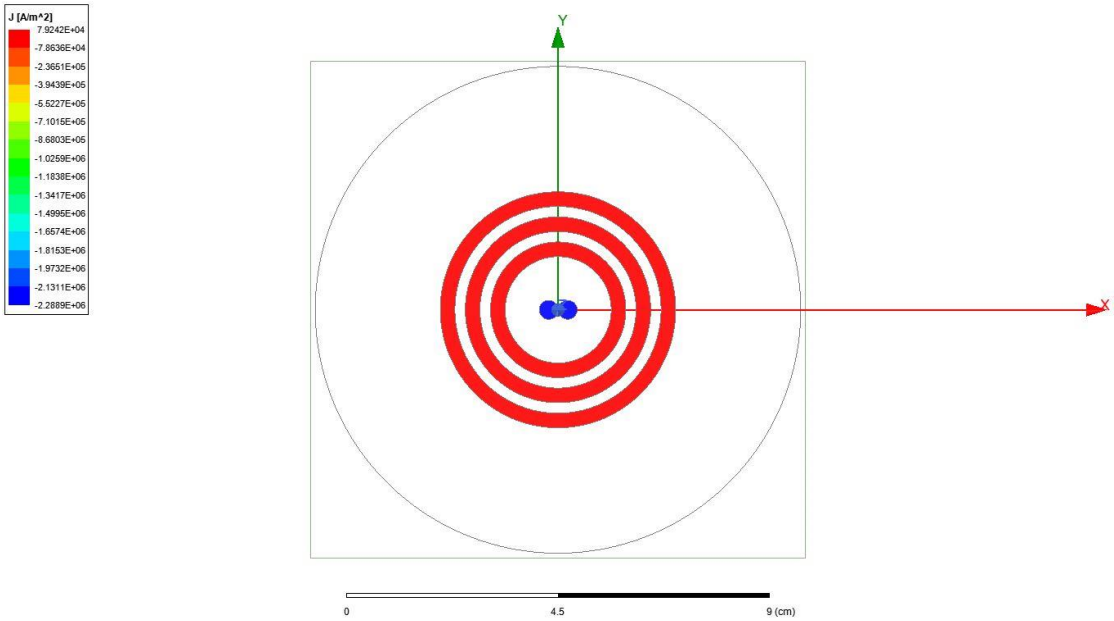

Figure 137 Simulation of current density in a coaxial transformer with three turns on the outside conductor and two turns on the inside conductor

Figure 138 shows the simulation of a representative coaxial winding transformer with two turns on the outer winding and one turn on the inside winding. Excitation on the outside conductor is 10 A and on the inside conductor is 20 A. Simulation result at 60 Hz is shown

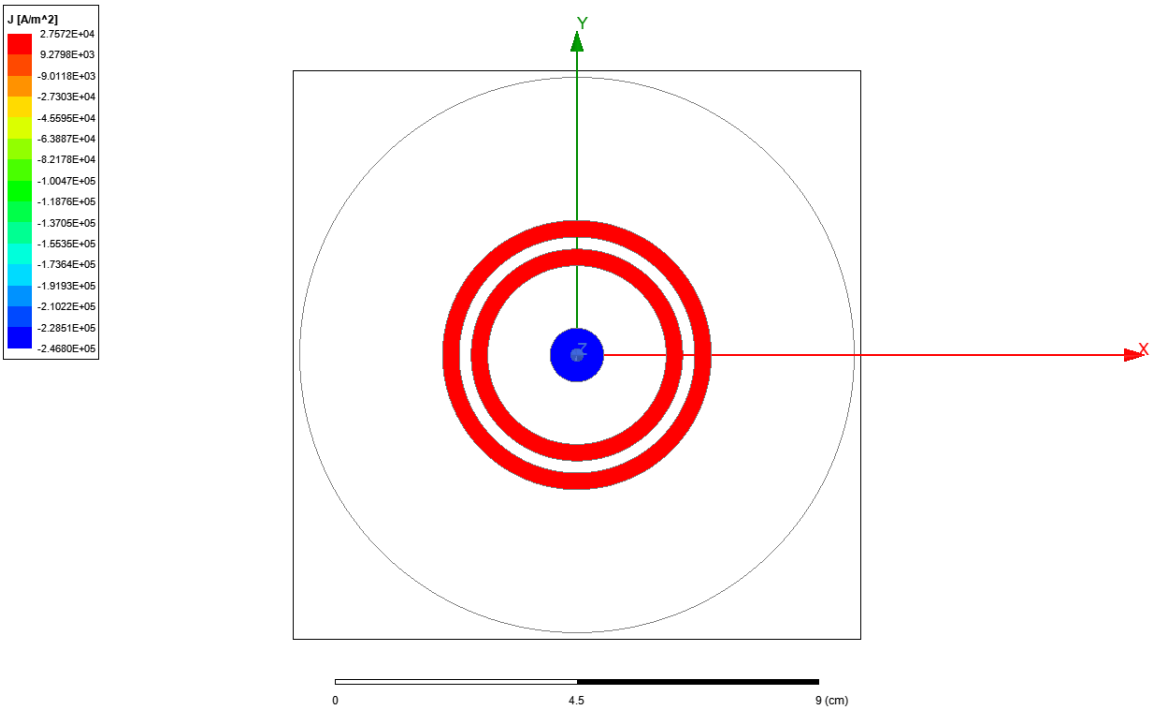

Figure 138 Simulation of current density in a coaxial winding transformer with two turn outer winding and one turn inner winding

Figure 139 shows Ansys simulation of a representative coaxial winding transformer. The current on the inside conductor is 30 A and on the outside conductor is 10 A. Simulation result at 60 Hz is shown.

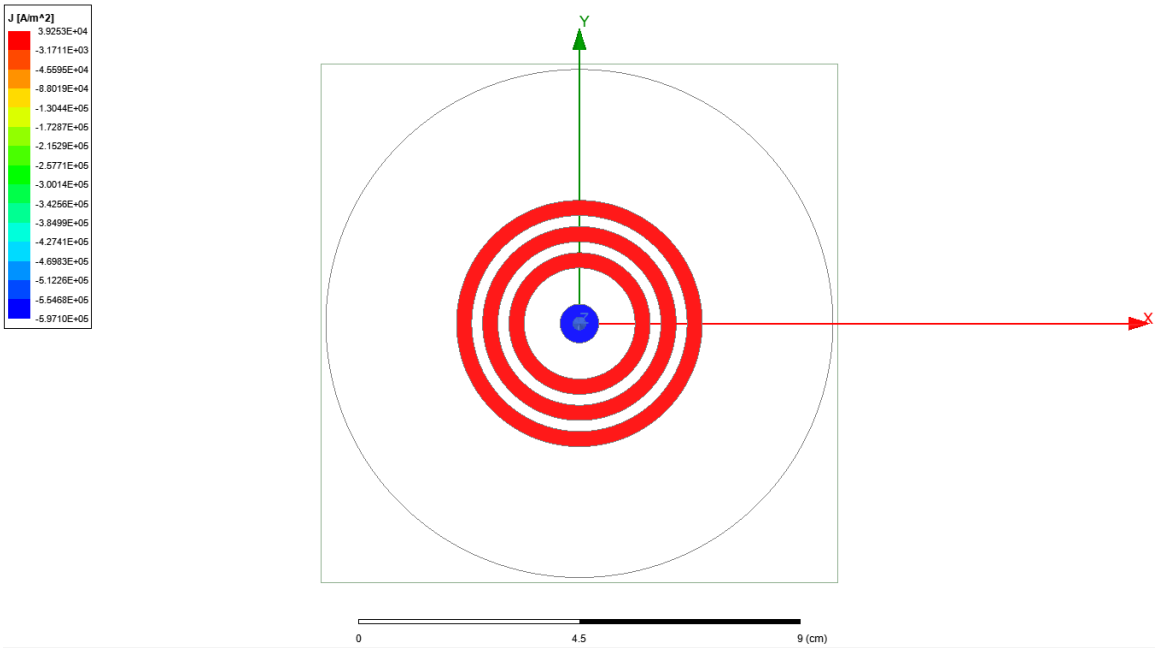

Figure 139 Simulation of current density in a coaxial winding transformer with three turns on the outside conductor and one turn on the inside conductor

References [52, 60] discuss another way to create multiple turns from a tubular conductor by splitting a tube into sections and connecting them in series. Figure 140 shows the Ansys Maxwell simulation of a representative CWT with two turns on the inside and outside conductor. Excitation on the inside and outside conductor is 50 A. Simulation result at 60 Hz is shown.

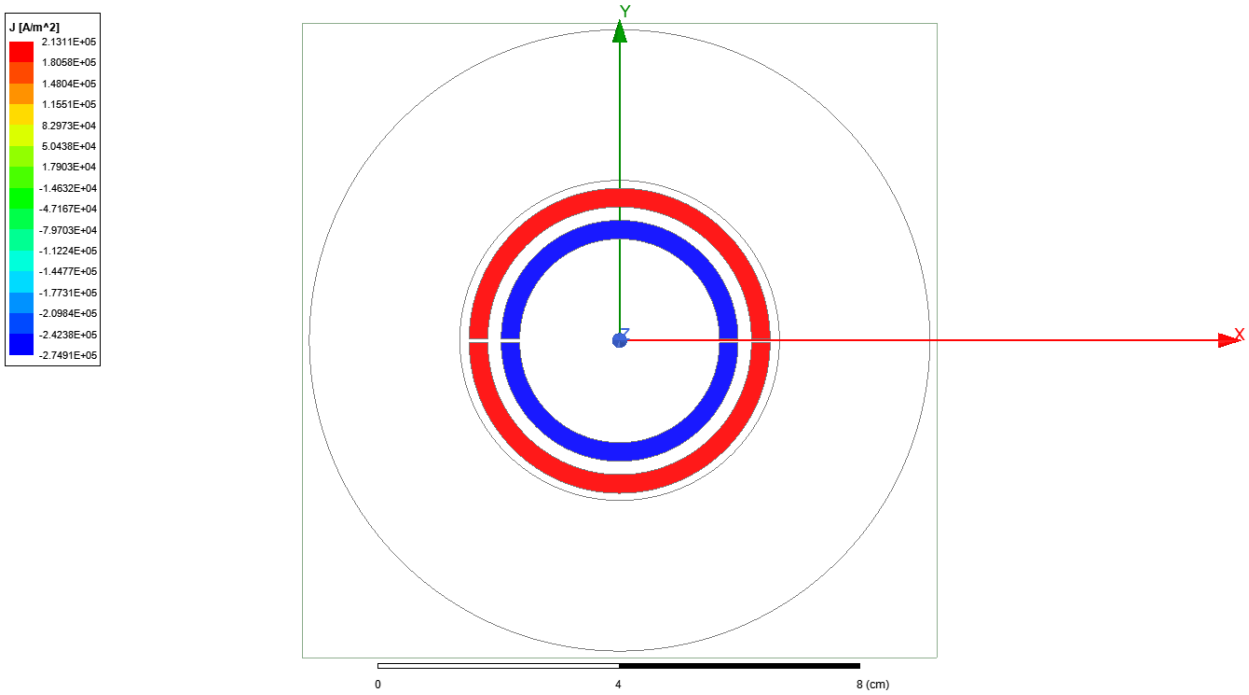

Figure 140 Simulation of current density in a coaxial winding transformer with two turns on the inside and outside conductor

Figure 141 shows the simulation of a representative coaxial winding transformer with two turns on the inside conductor and two turns on the outside conductor. Excitation on the inside and outside conductor is 20 A. Simulation result at 60 Hz is shown.

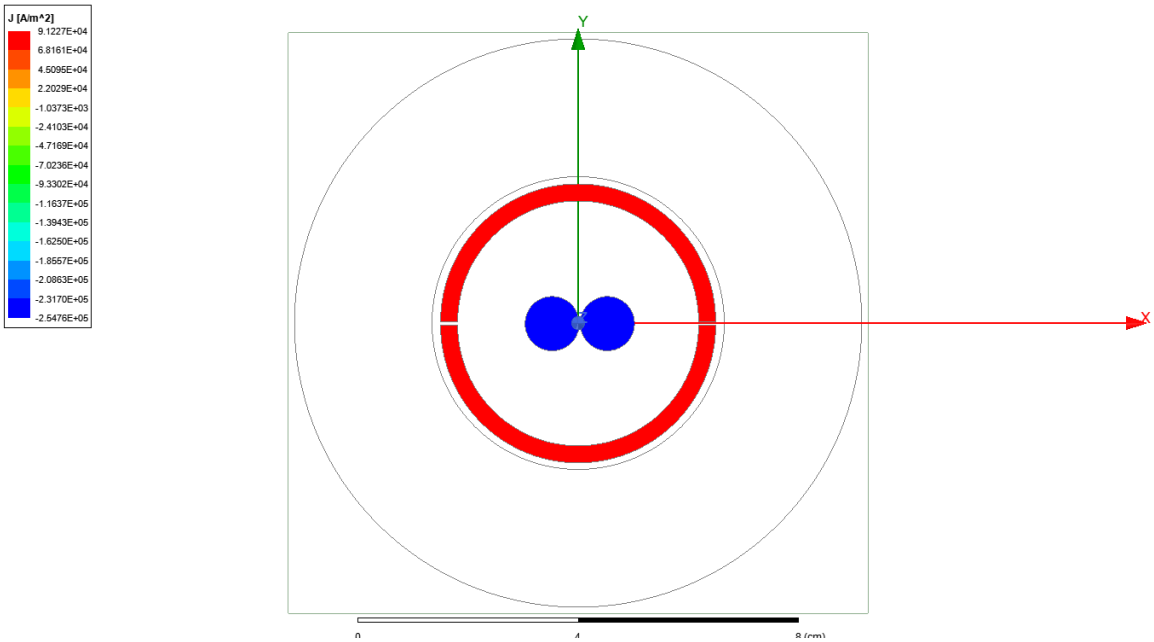

Figure 141 Simulation of current density in a CWT with a two turn outside conductor and two turns on the inside conductor

Figure 142 shows the simulation of a representative coaxial winding transformer with four turns on the inside conductor and two turns on the outside conductor. Excitation on the inside conductor is 20 A and on the outside conductor is 40 A. Simulation result at 60 Hz is shown.

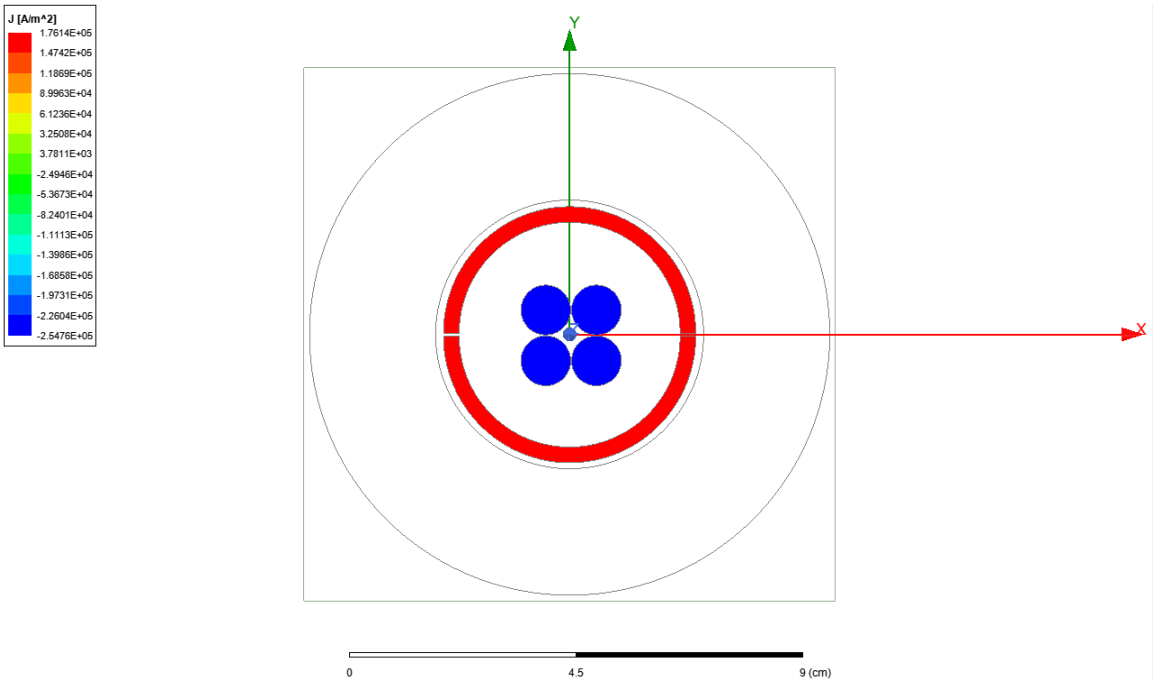

Figure 142 Simulation of current density in a coaxial winding transformer with two turn outer winding and four turn inner winding

Figure 143 shows the simulation of a representative coaxial winding transformer with a four-turn inner winding and four-turn outer winding. Excitation on the inner and outer winding is 50 A. Simulation result at 60 Hz is shown.

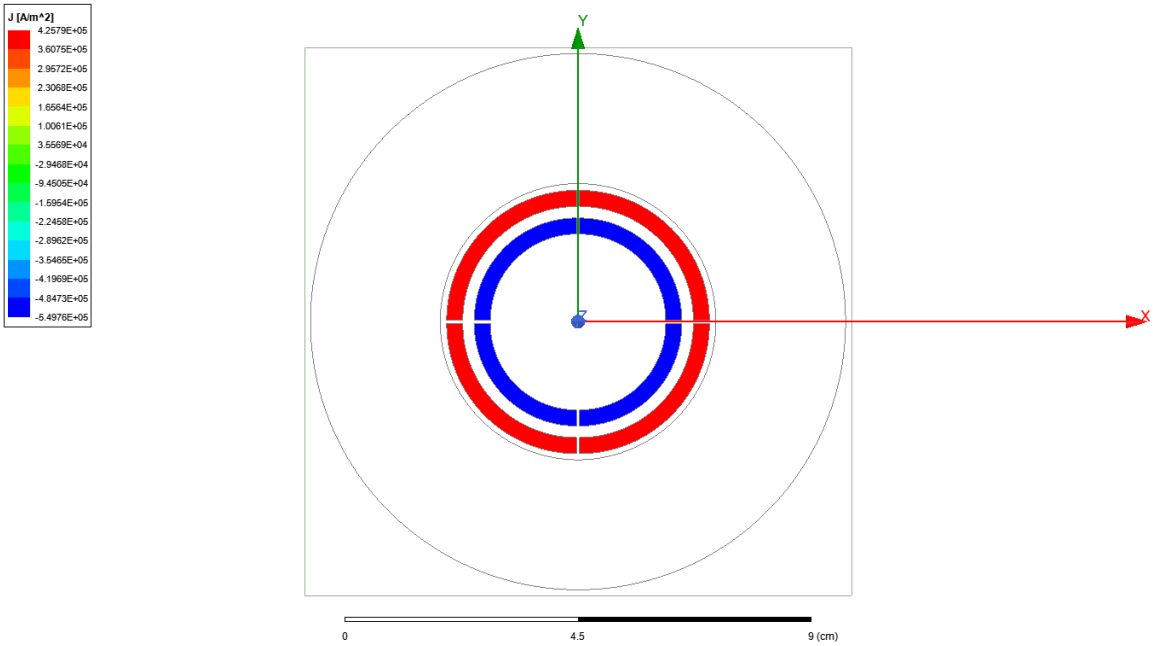

Figure 143 Simulation of current density in coaxial winding transformer with four turns on the inside conductor and four turns on the outside conductor

Figure 144 shows the simulation of a representative coaxial winding transformer with a four-turn outer winding and two turn inner winding. Excitation on the outer winding is 10 A and on the inner winding is 20 A. Simulation result at 60 Hz is shown.

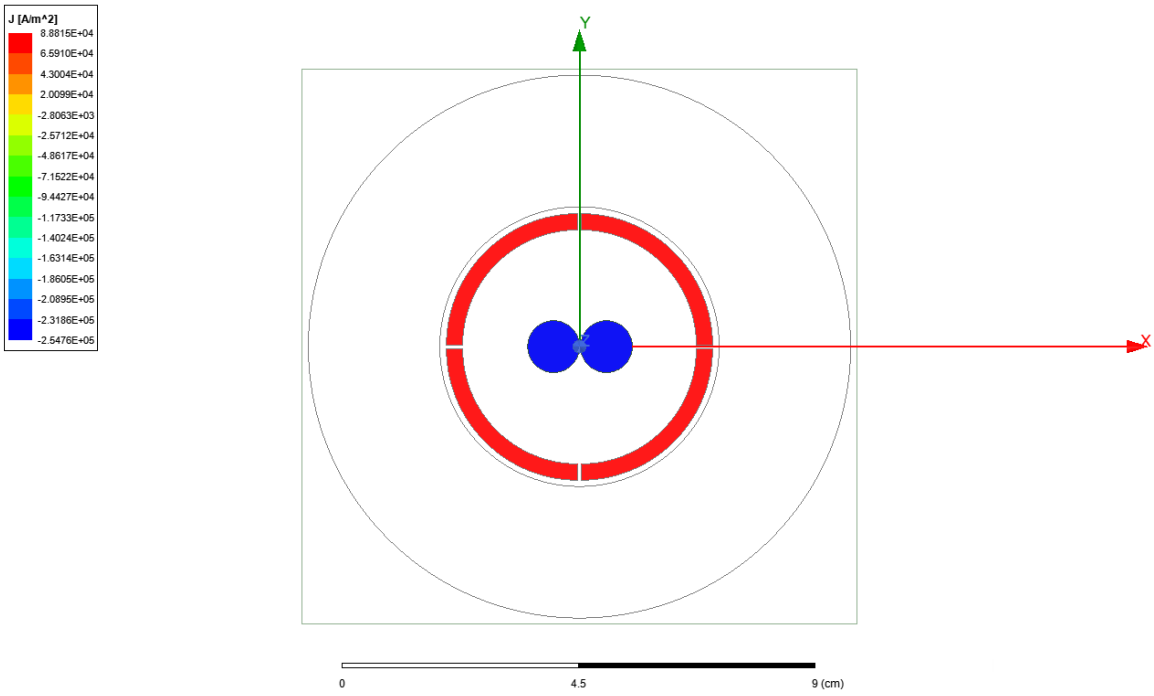

Figure 144 Simulation of current density in a coaxial winding transformer with four turns on the outside winding and two turns on the inside winding

An alternative arrangement of a representative coaxial winding transformer is shown in Figure 145 where four turns on the inside conductor and four turns on the outside conductor have been shown. Excitation on the inside and outside conductor is 10 A. Simulation result at 60 Hz is shown.

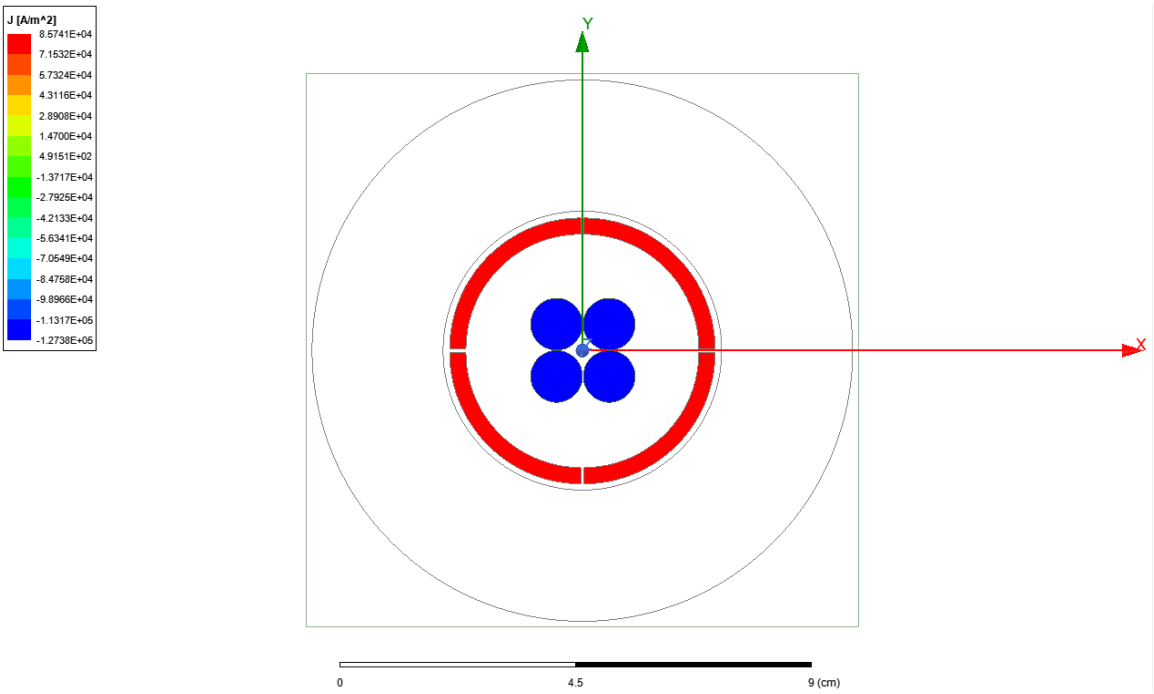

Figure 145 Simulation of current density in a coaxial winding transformer with a four-turn inner winding and four turn outer winding

Figure 146 shows the simulation of a representative coaxial winding transformer with four turns on the inside and outside conductor. Excitation on the inside and outside conductor is 15 A. Simulation result at 60 Hz is shown.

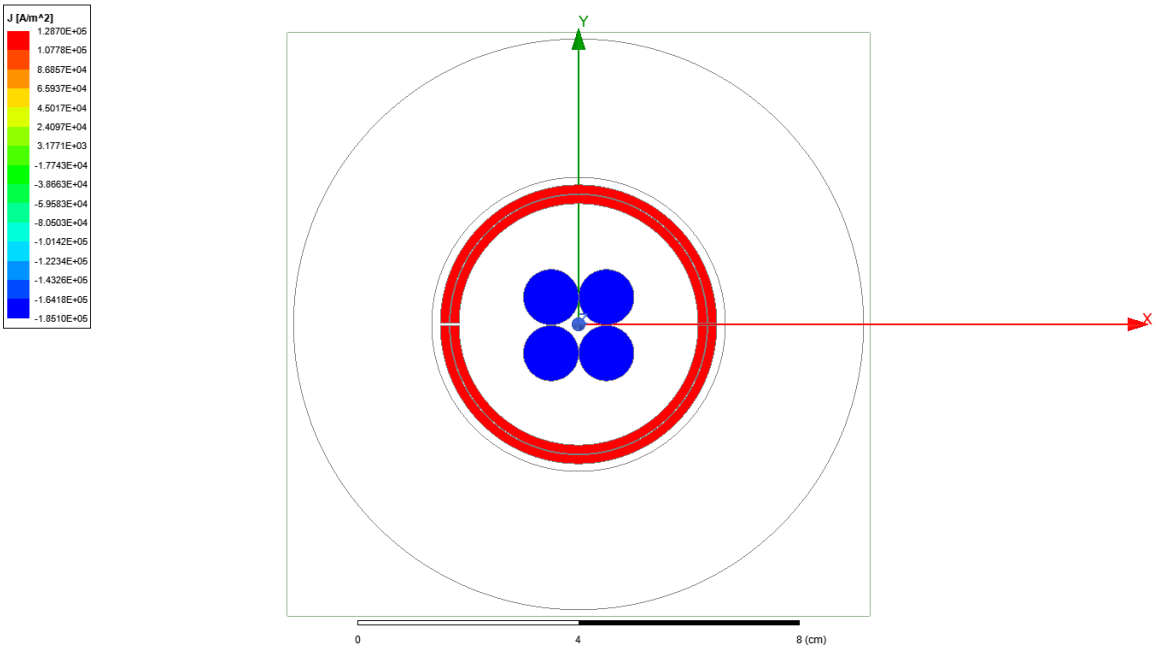

Figure 146 Simulation of current density in a coaxial winding transformer with four turns on the inner and outer winding

Figure 147 shows the simulation of a representative coaxial winding transformer with four turns on the outside conductor and two turns on the inside conductor. Excitation on the outside conductor is 7.5 A and on the inside conductor is 15 A. Simulation result at 60 Hz is shown.

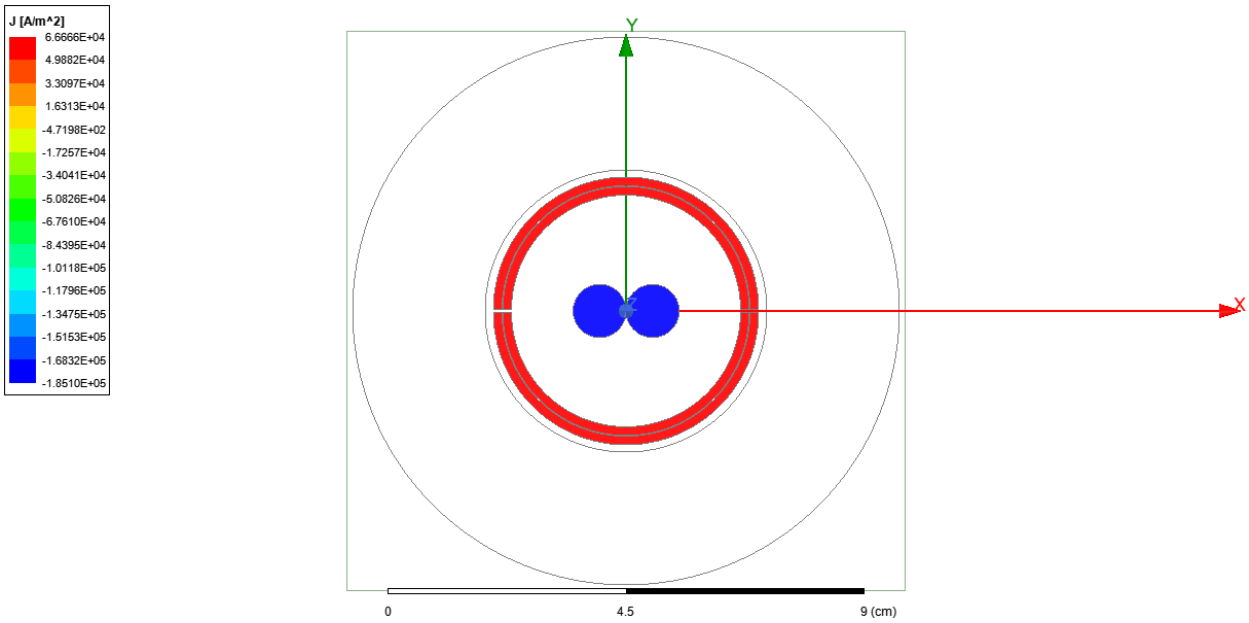

Figure 147 Simulation of current density in a coaxial winding transformer with four turns on the outer winding and two turns on the inner winding

Figure 148 shows the simulation of a representative coaxial winding transformer with four turns on the inner and outer winding. Excitation on the inner and outer winding is 15 A. Simulation result at 60 Hz is shown.

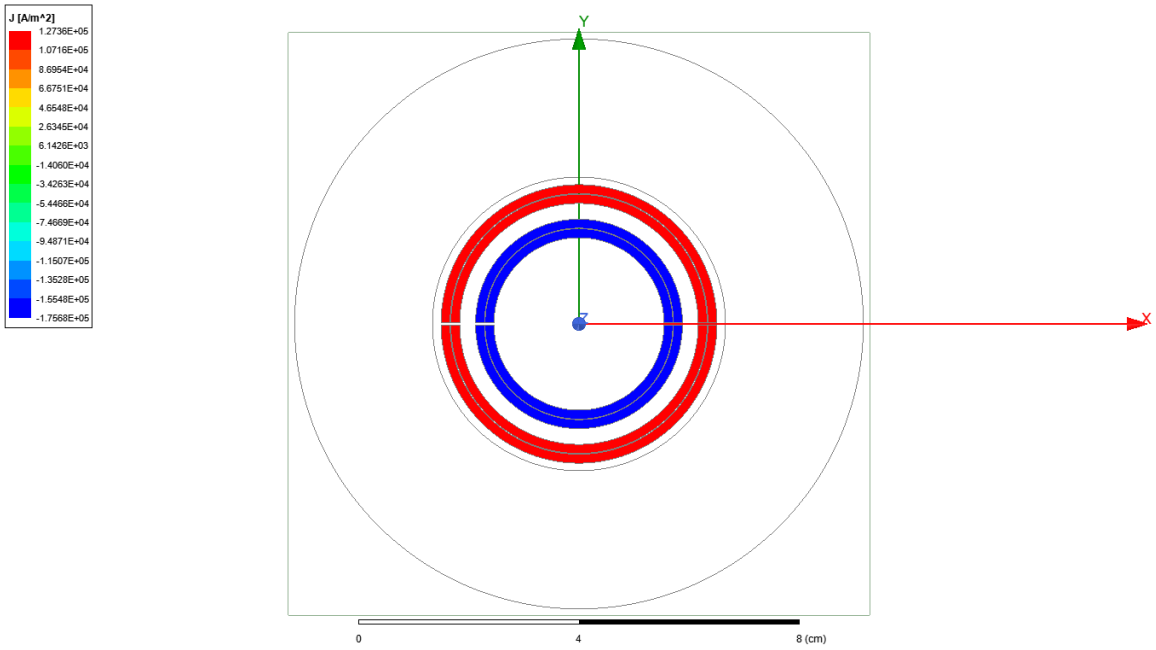

Figure 148 Simulation of current density in a coaxial winding transformer with four turns on the inner winding and four turns on the outer winding

Figure 149 shows the simulation of a representative coaxial transformer with four turns on the outer winding and two turns on the inner winding. Excitation on the outer winding is 10 A and on the inner winding is 20 A. Simulation result at 60 Hz is shown.

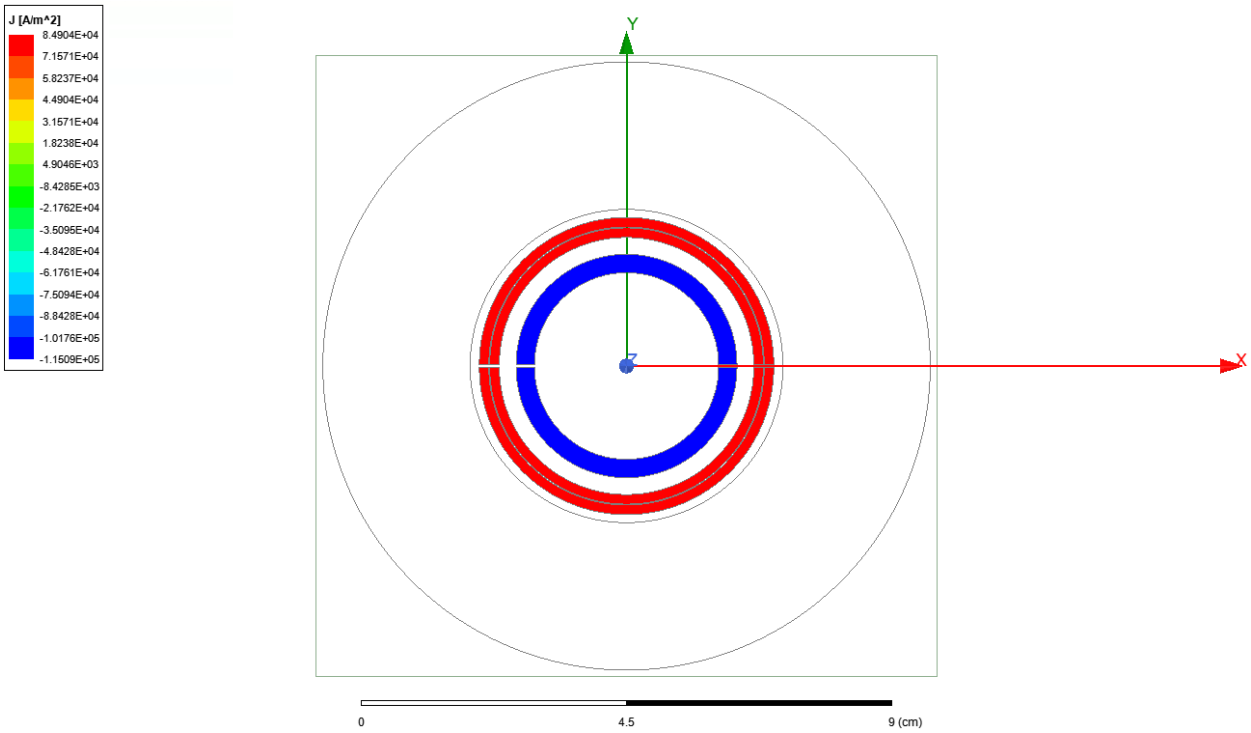

Figure 149 Simulation of current density in a coaxial transformer with four turns on the outer winding and two turns on the inner winding.

Figure 150 shows the simulation of a representative coaxial winding transformer with four turns on the inner and outer winding. Excitation on both inner and outer winding is 15 A. Simulation result at 60 Hz is shown.

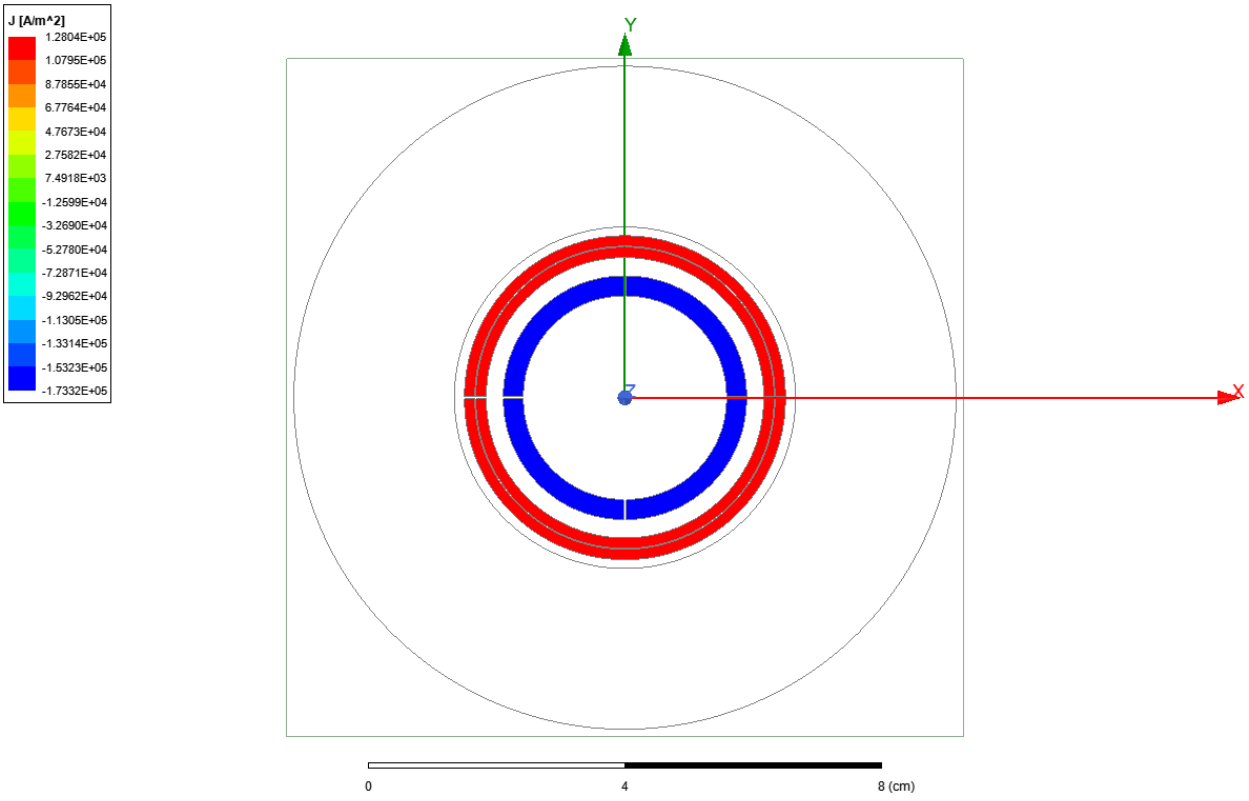

Figure 150 Simulation of current density in a coaxial winding transformer with four turns on the inner and outer winding

Figure 151 shows a representative four turn CHWT simulated in Ansys Maxwell (solution type : magnetostatic). Simulation result at 12 A excitation is shown

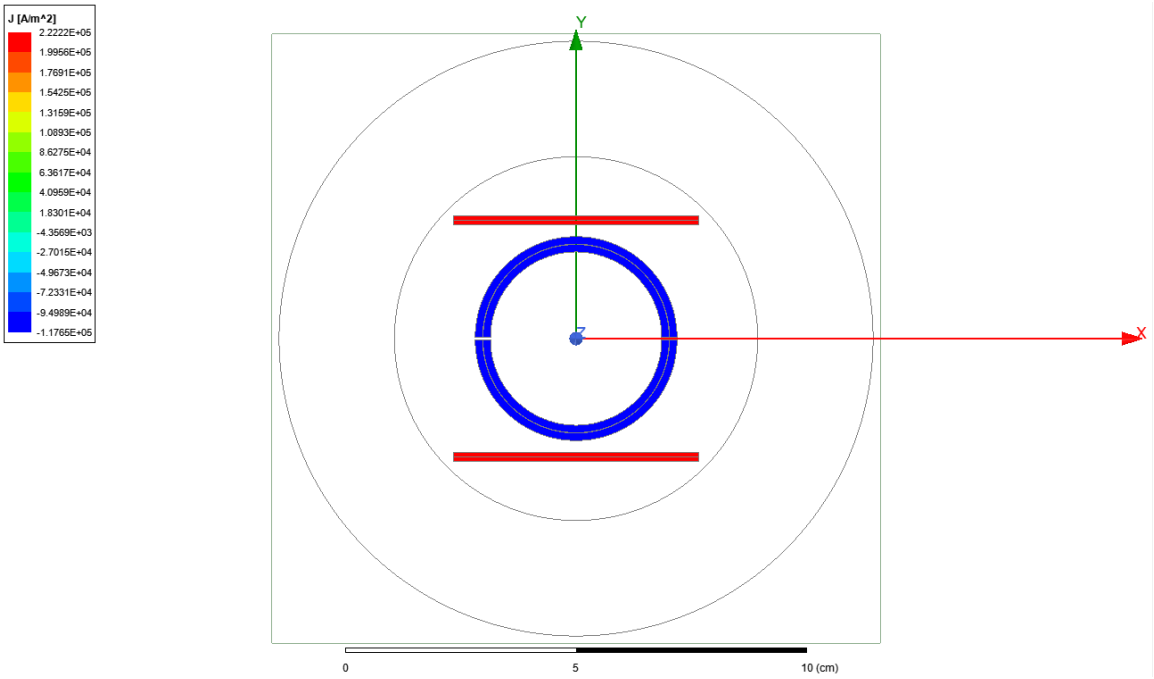

Figure 151 Simulation of current density in a four turn CHWT

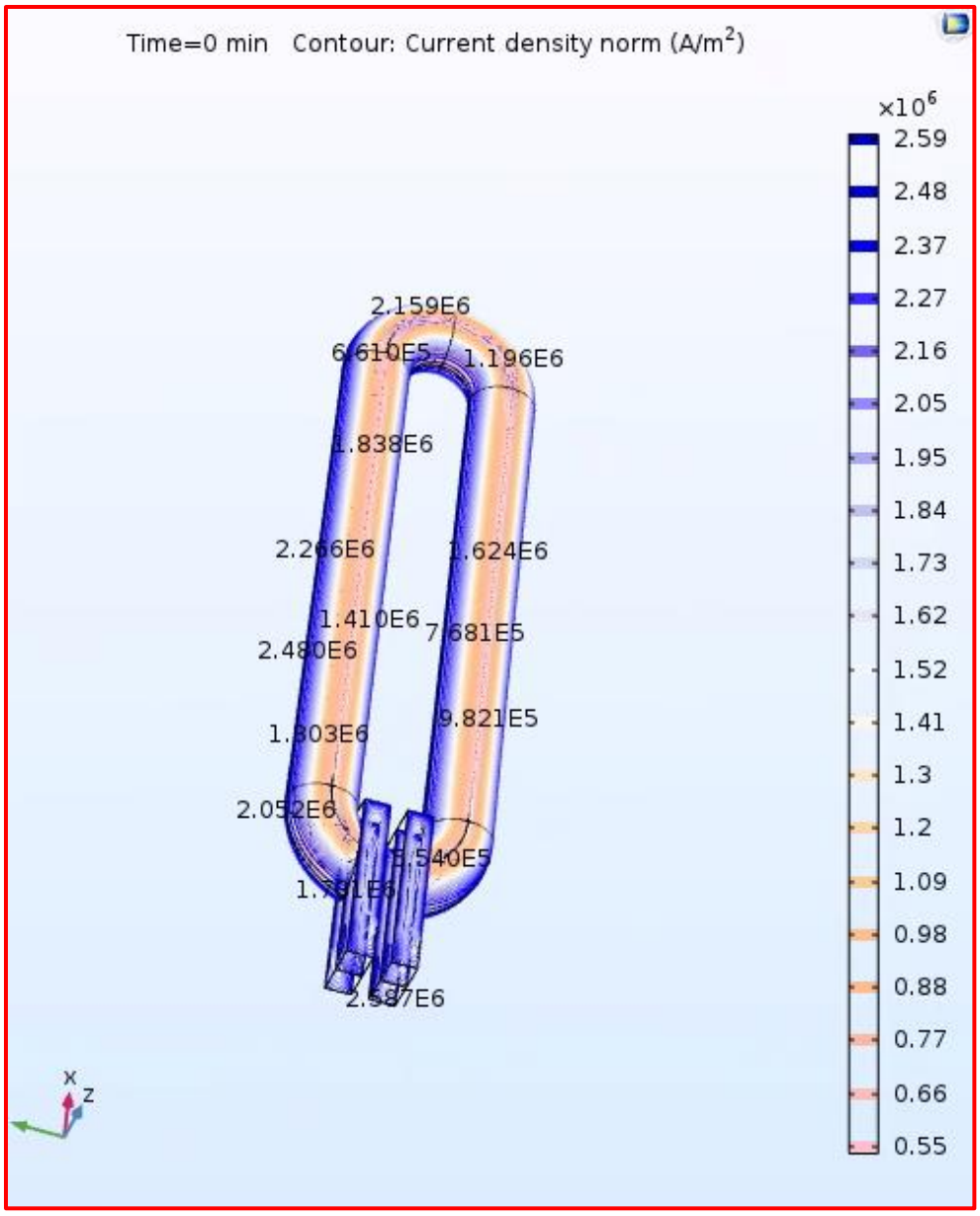

Figure 152 Simulation of current density in a CWT primary winding

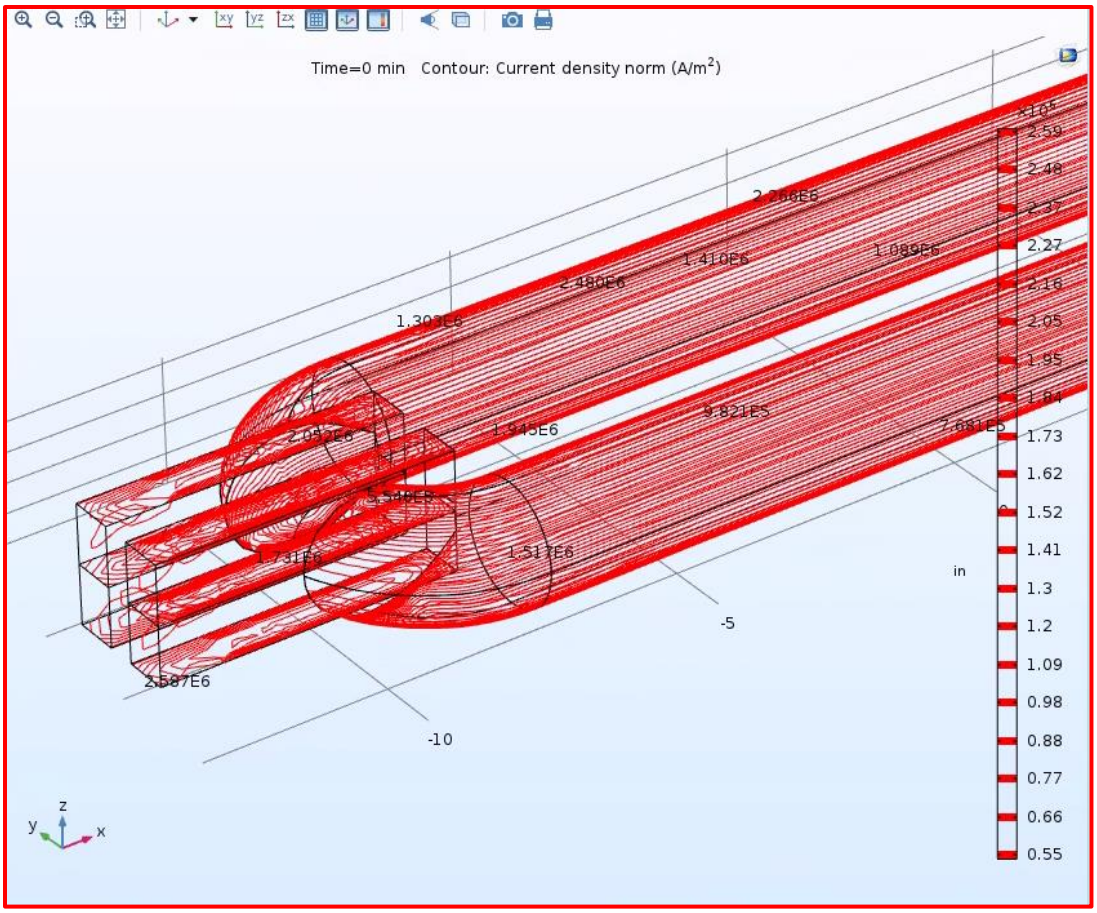

Figure 153 Simulation of current density in CWT primary winding (zoomed in)

Simulation of current density in the primary winding of a CWT have been shown in Figure 152 and Figure 153.

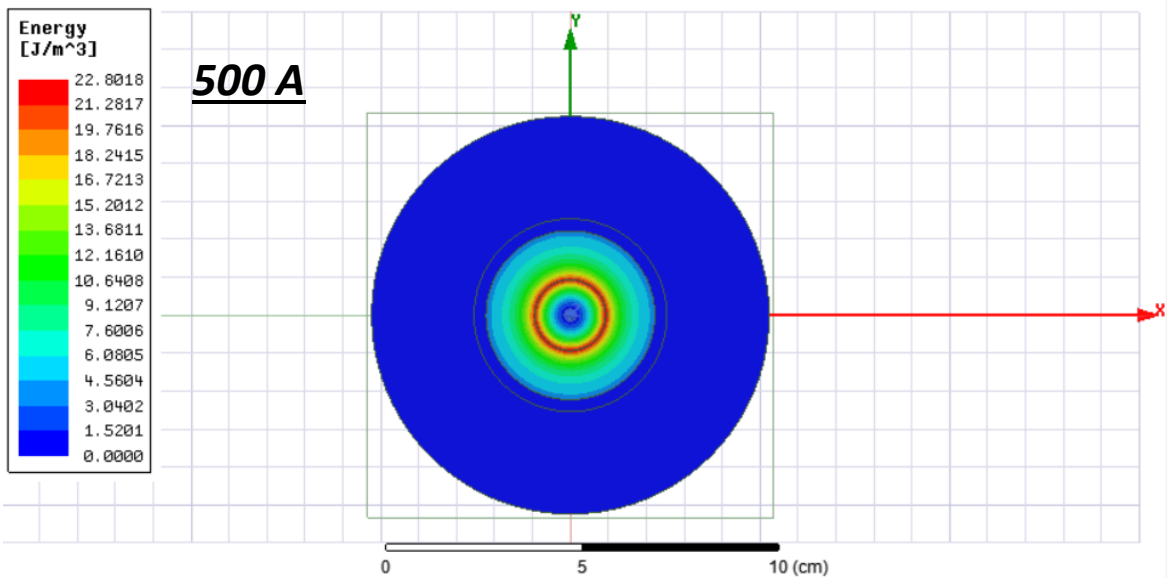

Figure 154 Simulation of leakage energy in CWT at 500 A

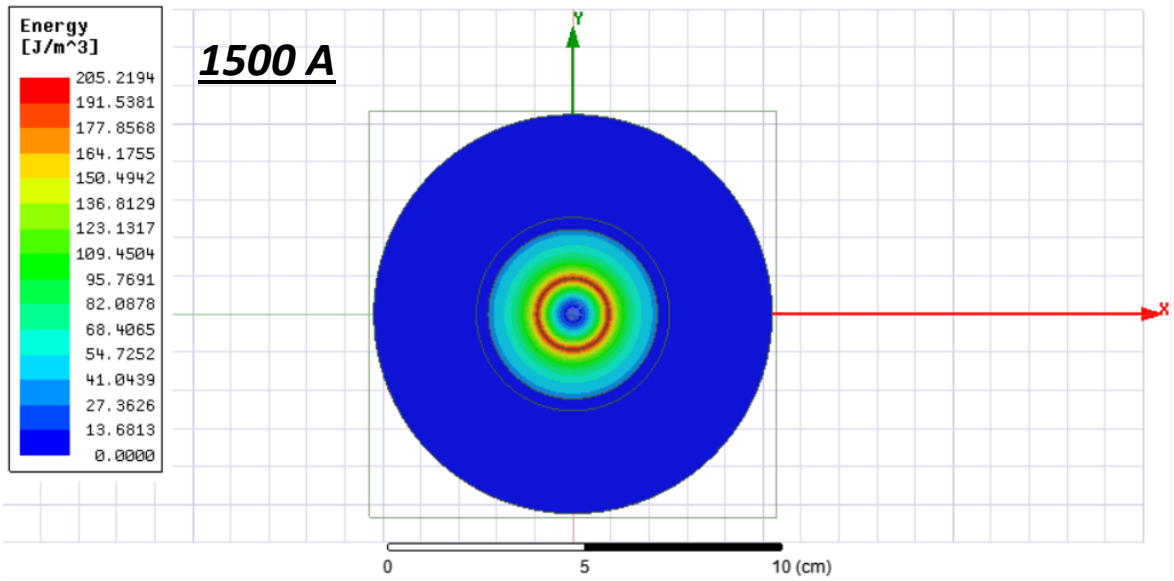

Figure 155 Simulation of leakage energy in CWT at 1500 A

Simulation of leakage energy in a CWT at 500 A and 1500 A have been shown in Figure 154 and Figure 155

APPENDIX D. PROJECTION OF SIVOM THERMAL CHARACTERISTICS

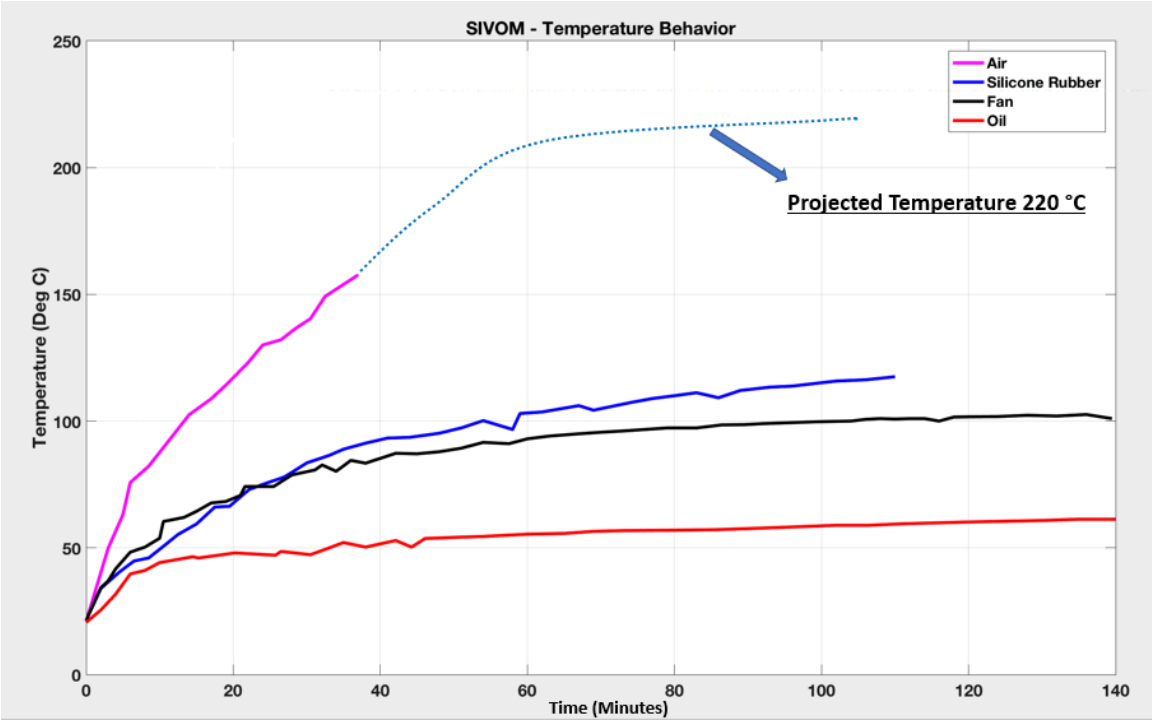

Figure 156 Projection of SIVOM thermal behavior

The thermal performance of SIVOM is shown in Figure 156. With no additional cooling, a final temperature of 220 ºC was projected. Experimental results with different cooling methods have been shown.

APPENDIX E. THERMAL CHARACTERISTICS OF THE DEVICE

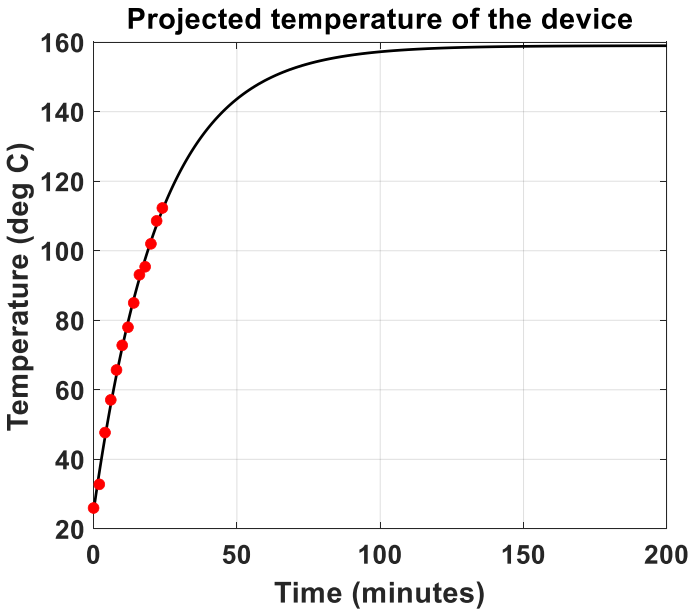

Figure 157 Thermal characteristics of the device at 1200 A

Without any additional cooling, the temperature rise shown in chapter 7 (Figure 90 at the end turn (base)) is expected to lead to a final temperature of close to 159 deg C.

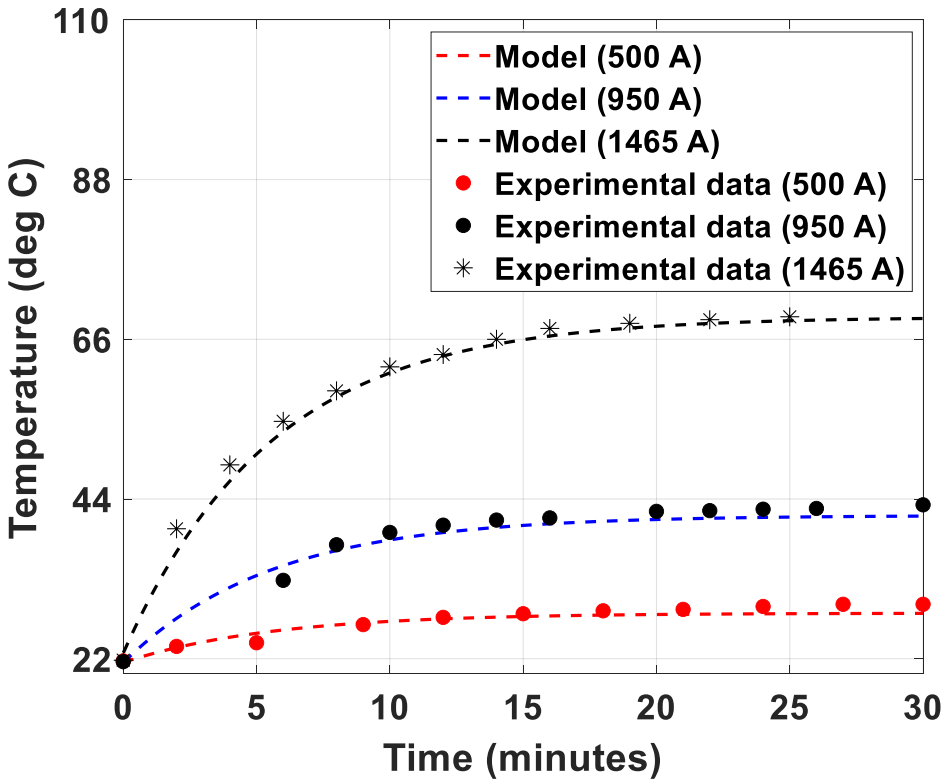

Figure 158 Comparison of experimental data and model

Figure 158 shows a comparison between experimental measurement of temperature for the inside conductor with 30 CFM fan and model at 500 A, 950 A and 1465 A.

APPENDIX F. THERMAL RESISTANCES IN THE DEVICE

In chapter 7, a thermal equivalent circuit for the device has been discussed under normal operating conditions. More explanation is provided below.

Heat is transferred radially from the magnet wire to the copper tube through convection. The thermal resistance for convective transfer of heat is given by

$$R_1 = \frac{1}{\bar{h} A_{sec}} \, ^\circ C/W \tag{55}$$

Where A_{sec} is the surface area of the inside conductor. Based on discussion in reference [67], equation (55) may further be written as

$$R_1 = \frac{1}{1.34 \, A_{sec}} \left(\frac{d_{sec}}{T_{sec} - T_{primary}} \right)^{0.25} \, ^\circ C/W \tag{56}$$

Where A_{sec} is the surface area of the inside conductor, d_{sec} is the diameter of the inside conductor, T_{sec} is the temperature of the inside conductor and $T_{primary}$ is the temperature of the copper tube.

The heat is then transferred radially through conduction from the outer surface of the copper tube to the inner surface of the core. The thermal resistance is given by

$$R_2 = \frac{ln\left(\frac{R_{core\ inner}}{R_{primary\ outer}}\right)}{2\pi L_c \lambda_{primary}} = 8.06 * 10^{-5}\ °C/W \quad (57)$$

Where $R_{core\ inner}$ is the inner radius of the core, $R_{primary\ outer}$ is the outer radius of the copper tube, $\lambda_{primary}$ is the thermal conductivity of the primary and L_c is discussed in chapter 6. Thermal conductivity of copper is assumed to be 386 W/m/ºC.

Heat from the inner surface of the core is conducted through the body of the core to the outer surface of the core. The thermal resistance due to conduction is given by

$$R_3 = \frac{\ln\left(\frac{R_{core\ outer}}{R_{core\ inner}}\right)}{2\pi L_c \lambda_{core}} = 8.10 * 10^{-3}\ °C/W \quad (58)$$

Where $R_{core\ outer}$ is the outer radius of the core, $R_{core\ inner}$ is the inner radius of the core and λ_{core} is the thermal conductivity of silicon steel, assumed to be 42 W/m/ºC discussed in reference [58]

From the outer surface of the core, heat is transferred through convection to the ambient air.

$$R_4 = \frac{1}{\bar{h} A_{core}}\ °C/W \quad (59)$$

Where A_{core} is the surface area of the core. This equation may further be written as

$$R_4 = \frac{1}{1.34\, A_{core}} \left(\frac{D_{core}}{T_{core\ outer} - T_{amb}} \right)^{0.25} \ ^\circ C/W \tag{60}$$

Where D_{core} is outer diameter of the core (10.4775 cm), $T_{core\ outer}$ is the temperature of the outer surface of the core and T_{amb} is the ambient temperature. The surface area of the core was calculated to be 0.102 m^2.

At the end turns, majority of the heat will be transferred from the inside conductor to the copper tube through convection. The thermal resistance is given by

$$R_5 = \frac{1}{\bar{h} A_{sec}} \ ^\circ C/W \tag{61}$$

Equation (61) may further be written as

$$R_5 = \frac{1}{1.34\, A_{sec}} \left(\frac{d_{sec}}{T_{sec} - T_{primary}} \right)^{0.25} \ ^\circ C/W \tag{62}$$

Heat from the outer surface of the copper tube is transferred to the ambient air through convection. The corresponding thermal resistance is given by

$$R_6 = \frac{1}{\bar{h} A_{primary}} \ ^\circ C/W \tag{63}$$

Where $A_{primary}$ is the surface area of the primary winding. Equation (63) may further be written as

$$R_6 = \frac{1}{1.34\, A_{primary}} \left(\frac{d_{primary}}{T_{primary} - T_{amb}} \right)^{0.25} \; ^\circ C/W \tag{64}$$

Where $A_{primary}$ is the surface area of the primary winding, $d_{primary}$ is the outer diameter of the copper tube (5.08 cm), $T_{primary}$ is the temperature of the copper tube and T_{amb} is the ambient temperature. At the end turn, $A_{primary}$ was calculated to be 0.0525 m^2. From equation (64) it may be seen that the expression for thermal resistance requires an estimate of the surface temperature. Reference [50] has discussed, the surface temperature of the primary is used as difference with the ambient temperature, taken as fourth root and may be insensitive to errors. Results may be slightly improved by iteratively updating the surface temperature.

Thermal capacitance $(C_t)$is the ability of the body to store thermal energy and is a function of the material's volume (V), specific heat (c) and mass density (ρ_m). It is given by

$$C_t = \rho_m \, V \, c \quad J/^\circ\mathrm{C} \tag{65}$$

Volume of the copper tube is calculated to be $76.08\ cm^3$ on each side. The thermal capacitance can be calculated to be 261.65 $J/^\circ\mathrm{C}$. Both copper conductors and core are component parts with important thermal capacity. Using the thermal resistance and capacitance, the device performance characteristics may be understood through the calculation of time constant. Since the model deals with the steady state calculations, capacitances are not discussed in the thermal equivalent circuit [59].

APPENDIX G. NO-LOAD LOSSES IN AN INDUCTION MOTOR

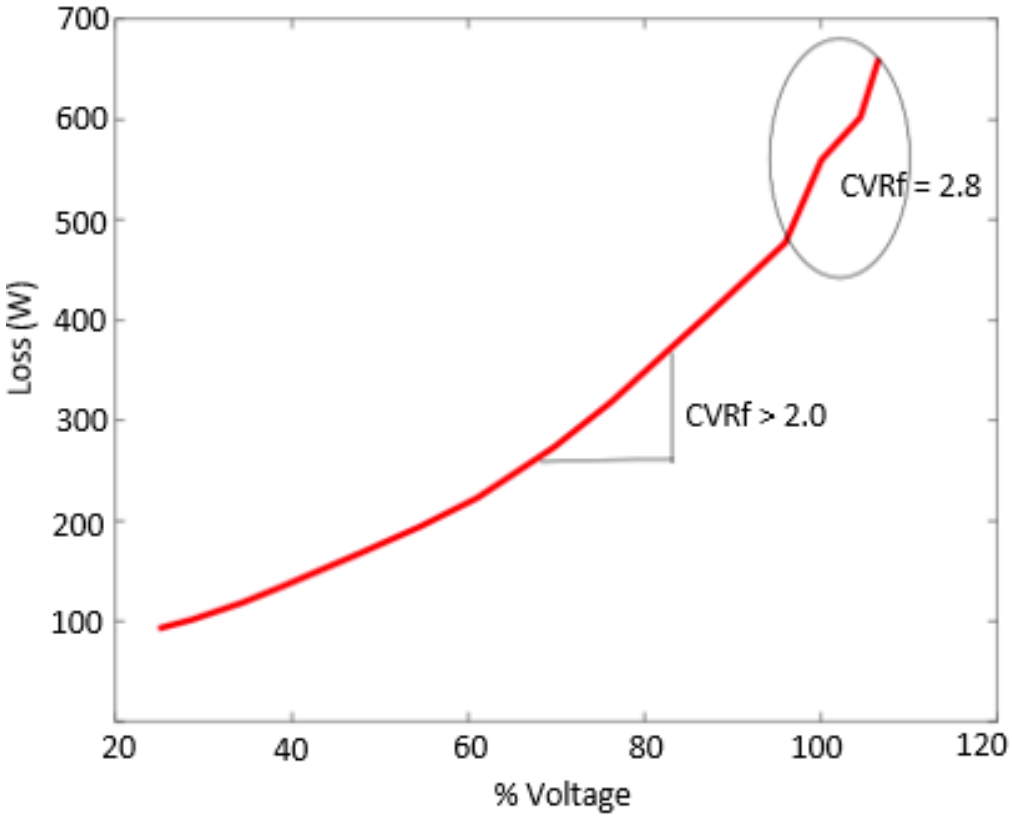

Figure 159 Measurement of core loss in an induction motor

Figure 159 shows the measurement of core loss in a 25 HP induction motor along with CVR factor.

APPENDIX H. CONVERSION BETWEEN ZIP LOAD MODEL AND EXPONENTIAL LOAD MODEL

The discussion on load model from literature review is continued to show a comparison between coefficients based on ZIP load model and exponential load model. The conversion between ZIP model and exponential model is given by

$$a_p = 2a_2 + a_1 \tag{66}$$

Where a_p is the coefficient pertaining to the exponential model, a_2 corresponds to the constant impedance load component in a ZIP load model and a_1 corresponds to constant current load component.

Synthetic data generated in MATLAB shown in Figure 160 below shows the change in power consumption for a 50 KW load modeled using exponential load model in MATLAB and Simulink, if $a_p = 0.95$. This may be represented by a ZIP load with coefficients $a_2 = 0.25$ and $a_1 = 0.45$ or $a_2 = 0.35$ and $a_1 = 0.25$

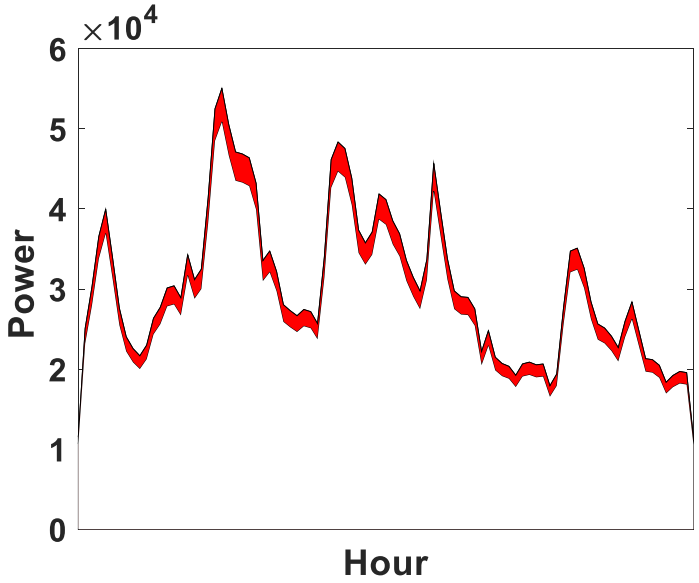

Figure 160 Change in power consumption for a 50 KW load simulated for a voltage change from 500 V to 460 V when a_p= 0.95

REFERENCES

[1] L. D. G. Lagos, "Advanced voltage control for energy conservation in distribution networks," The University of Manchester (United Kingdom), 2018.

[2] "Climate Change 2013: The Physical Science Basis [Online]," The Intergovernmental Panel on Climate Change (IPCC)2013, Available: http://www.ipcc.ch/report/ar5/wg1/.

[3] "Electricity Information 2019 : Overview," International Energy Agency (IEA)2019, Available: https://webstore.iea.org/electricity-information-2019-overview.

[4] "Climate Change 2014: Synthesis Report Summary for Policymakers," Intergovernmental Panel on Climate Change - IPCC2014, Available: http://www.ipcc.ch/report/ar5/syr/.

[5] A. Ballanti, "Voltage-led load management in UK distribution networks," PhD Thesis, University of Manchester, 2018.

[6] (2005). *Interim Evaluation of The Utility Distribution System Efficiency Initiative (DEI) - Phase 1*. Available: https://neea.org/img/uploads/distribution-efficiency-initiative-e05-139.pdf

[7] D. Divan, G. A. Luckjiff, W. E. Brumsickle, J. Freeborg, and A. Bhadkamkar, "A grid information resource for nationwide real-time power monitoring," *IEEE Transactions on Industry Applications,* vol. 40, no. 2, pp. 699-705, 2004.

[8] P. K. Sen and K. H. Lee, "Conservation Voltage Reduction Technique: An Application Guideline for Smarter Grid," *IEEE Transactions on Industry Applications,* vol. 52, no. 3, pp. 2122-2128, 2016.

[9] T. Wilson, "Energy conservation with voltage reduction-fact or fantasy," in *Rural Electric Power Conference, 2002. 2002 IEEE*, 2002, pp. C3-1: IEEE.

[10] P. K. Sen and K. H. Lee, "Conservation voltage reduction technique: An application guideline for smarter grid," in *Rural Electric Power Conference (REPC), 2014 IEEE*, 2014, pp. B1-1-B1-8: IEEE.

[11] Z. Wang and J. Wang, "Review on implementation and assessment of conservation voltage reduction," *IEEE Transactions on Power Systems,* vol. 29, no. 3, pp. 1306-1315, 2014.

[12] R. Preiss and V. Warnock, "Impact of voltage reduction on energy and demand," *IEEE Transactions on Power Apparatus and Systems,* no. 5, pp. 1665-1671, 1978.

[13] J. De Steese, S. Merrick, R. Tepel, and J. Callaway, "Assessment of conservation voltage reduction applicable in the bpa service region," *BPA, PNL,* vol. 6380, 1987.

[14] B. Williams, "Distribution capacitor automation provides integrated control of customer voltage levels and distribution reactive power flow," in *Power Industry Computer Application Conference, 1995. Conference Proceedings., 1995 IEEE*, 1995, pp. 215-220: IEEE.

[15] A. Dwyer, R. E. Nielsen, J. Stangl, and N. S. Markushevich, "Load to voltage dependency tests at BC Hydro," *IEEE Transactions on Power Systems,* vol. 10, no. 2, pp. 709-715, 1995.

[16] J. Parks, "Preparing for the Utility of the Future Jim Parks, Sacramento Municipal Utility District," in *ACEEE Summer Study on Energy Efficiency in Buildings* ed, 2016.

[17] M. Chen, R. Shoults, J. Fitzer, and H. Songster, "The effects of reduced voltages on the efficiency of electric loads," *IEEE Transactions on Power Apparatus and Systems,* no. 7, pp. 2158-2166, 1982.

[18] S. Smith, H. Chun, V. Metha, R. Moghe, and D. Tholomier, "Reducing Peak Demand through Distributed Grid Edge Control," in *2017 IEEE Rural Electric Power Conference (REPC)*, 2017, pp. 52-60: IEEE.

[19] T. A. Short, *Electric power distribution handbook*. CRC press, 2014.

[20] P. Anderson, "Conservation Voltage Reduction," *Idaho Power, PowerPoint Slides,[Online].] Accessed,* vol. 10, 2014.

[21] J. Casavant, "Conservation voltage reduction: Improve energy efficiency and lower demand," in *PowerPoint Presentation Slides, IEEE 2013 REPC Conference, Stone Mountain, GA*, 2013.

[22] W. Sunderman, "Conservation voltage reduction system modeling, measurement, and verification," in *Transmission and Distribution Conference and Exposition (T&D), 2012 IEEE PES*, 2012, pp. 1-4: IEEE.

[23] M. A. Peskin, P. W. Powell, and E. J. Hall, "Conservation voltage reduction with feedback from advanced metering infrastructure," in *Transmission and Distribution Conference and Exposition (T&D), 2012 IEEE PES*, 2012, pp. 1-8: IEEE.

[24] K. P. Schneider, J. C. Fuller, F. K. Tuffner, and R. Singh, "Evaluation of conservation voltage reduction (CVR) on a national level," Pacific Northwest National Lab.(PNNL), Richland, WA (United States)2010.

[25] R. Singh, F. Tuffner, J. Fuller, and K. Schneider, "Effects of distributed energy resources on conservation voltage reduction (CVR)," in *2011 IEEE Power and Energy Society General Meeting*.

[26] D. P. Chassin, K. Schneider, and C. Gerkensmeyer, "GridLAB-D: An open-source power systems modeling and simulation environment," in *2008 IEEE/PES Transmission and Distribution Conference and Exposition*, 2008, pp. 1-5: IEEE.

[27] R. H. Fletcher and A. Saeed, "Integrating engineering and economic analysis for conservation voltage reduction," in *Power Engineering Society Summer Meeting, 2002 IEEE*, 2002, vol. 2, pp. 725-730: IEEE.

[28] B. Kennedy and R. Fletcher, "Conservation voltage reduction (CVR) at Snohomish County PUD," *IEEE Transactions on Power Systems*, vol. 6, no. 3, pp. 986-998, 1991.

[29] D. Lauria, "Conservation Voltage Reduction (CVR) at northeast utilities," *IEEE Transactions on Power Delivery*, vol. 2, no. 4, pp. 1186-1191, 1987.

[30] D. Kirshner, "Implementation of conservation voltage reduction at Commonwealth Edison," *IEEE Transactions on Power Systems*, vol. 5, no. 4, pp. 1178-1182, 1990.

[31] J. Erickson and S. Gilligan, "The effects of voltage reduction on distribution circuit loads," *IEEE Transactions on Power Apparatus and Systems*, no. 7, pp. 2014-2018, 1982.

[32] B. Shah, A. Bose, and A. Srivastava, *Load modeling and voltage optimization using smart meter infrastructure*. IEEE, 2013.

[33] R. Lawrence, "Voltage optimization," *IEEE Industry Applications Magazine*, vol. 12, no. 5, pp. 28-33, 2006.

[34] A. Bendre, D. Divan, W. Kranz, and W. E. Brumsickle, "Are voltage sags destroying equipment?," *IEEE Industry Applications Magazine*, vol. 12, no. 4, pp. 12-21, 2006.

[35] W. E. Brumsickle, R. S. Schneider, G. A. Luckjiff, D. M. Divan, and M. F. McGranaghan, "Dynamic sag correctors: cost-effective industrial power line conditioning," *IEEE Transactions on Industry Applications*, vol. 37, no. 1, pp. 212-217, 2001.

[36] A. Bokhari *et al.*, "Experimental determination of the ZIP coefficients for modern residential, commercial, and industrial loads," *IEEE Transactions on Power Delivery*, vol. 29, no. 3, pp. 1372-1381, 2014.

[37] M. Diaz-Aguiló *et al.*, "Field-validated load model for the analysis of CVR in distribution secondary networks: Energy conservation," *IEEE Transactions on Power Delivery*, vol. 28, no. 4, pp. 2428-2436, 2013.

[38] J. De Steese, J. Englin, and R. Sands, "Conservation voltage reduction potential in the pacific northwest," Pacific Northwest Lab., Richland, WA (USA)1990.

[39] C.-S. Chen, T.-H. Wu, C.-C. Lee, and Y.-M. Tzeng, "The application of load models of electric appliances to distribution system analysis," *IEEE transactions on power systems*, vol. 10, no. 3, pp. 1376-1382, 1995.

[40] C.-S. Chen, "The effect of voltage control to the efficiency and operation of electric distribution system," University of Texas at Arlington, 1984.

[41] N. Markushevich and A. Berman, "New aspects of IVVO in active distribution networks," in *PES T&D 2012*, 2012, pp. 1-5: IEEE.

[42] J. Marchgraber, E. Xypolytou, I. Lupandina, W. Gawlik, and M. Stifter, "Measurement-based determination of static load models in a low voltage grid," *2016 IEEE PES Innovative Smart Grid Technologies Conference Europe (Isgt-Europe)*, 2016.

[43] C. A. Baone, S. Veda, Y. Pan, W. Premerlani, J. Dai, and A. Johnson, "Measurement based Static Load Model Identification," *2015 IEEE Power & Energy Society General Meeting*, 2015.

[44] J. Wang, Q. Hunag, A. Raza, T. Hong, Z. Zhang, and H. Li, "ZIP and equivalent thermostatic loads impacts on energy savings of conservation voltage reduction," in *2017 2nd International Conference on Power and Renewable Energy (ICPRE)*, 2017, pp. 250-254: IEEE.

[45] X. Liang, W. Xu, C. Chung, W. Freitas, and K. Xiong, "Dynamic load models for industrial facilities," *IEEE Transactions on Power systems*, vol. 27, no. 1, pp. 69-80, 2012.

[46] A. Borghetti, R. Caldon, A. Mari, and C. Nucci, "On dynamic load models for voltage stability studies," *IEEE Transactions on Power Systems*, vol. 12, no. 1, pp. 293-303, 1997.

[47] S. Jayaraman, M. Miranbeigi, P. Kandula, T. Grant, and D. Divan, "Reducing Energy Consumption in Industrial Plants Using Behind the Meter Conservation Voltage Reduction," in *2018 IEEE Energy Conversion Congress and Exposition (ECCE)*, 2018, pp. 4791-4798: IEEE.

[48] Z. Wang, M. Begovic, and J. Wang, "Analysis of conservation voltage reduction effects based on multistage SVR and stochastic process," *IEEE Transactions on Smart Grid*, vol. 5, no. 1, pp. 431-439, 2014.

[49] K.-S. Shim *et al.*, "Estimation of conservation voltage reduction factors using measurement data of KEPCO system," *Energies*, vol. 10, no. 12, p. 2148, 2017.

[50] K. W. Klontz, "Analysis and design of a coaxial winding transformer interface for an electric vehicle charging system," 1996.

[51] D. M. Divan and D. W. Novotny, "High temperature co-axial winding transformers," 1993.

[52] K. W. Klontz, D. M. Divan, and D. W. Novotny, "An actively cooled 120 kW coaxial winding transformer for fast charging electric vehicles," *IEEE Transactions on Industry Applications,* vol. 31, no. 6, pp. 1257-1263, 1995.

[53] M. H. Kheraluwala, D. W. Novotny, and D. M. Divan, "Coaxially wound transformers for high-power high-frequency applications," *IEEE Transactions on power electronics,* vol. 7, no. 1, pp. 54-62, 1992.

[54] P. Perfector. (2018). *Case studies [Online]*. Available: https://powerperfector.com/

[55] E. Europa. (2018). *Case studies [Online]*. Available: https://www.energia-europa.com/en/energia-europa-1

[56] M. El-Sherbiny, "Representation of the magnetization characteristic by a sum of exponentials," *IEEE Transactions on Magnetics,* vol. 9, no. 1, pp. 60-61, 1973.

[57] C. Perez-Rojas, "Fitting saturation and hysteresis via arctangent functions," *IEEE Power Engineering Review,* vol. 20, no. 11, pp. 55-57, 2000.

[58] F. Kreith, R. M. Manglik, and M. S. Bohn, *Principles of heat transfer*. Cengage learning, 2012.

[59] S. Purushothaman and F. De León, "Heat-transfer model for toroidal transformers," *IEEE transactions on power delivery,* vol. 27, no. 2, pp. 813-820, 2012.

[60] M. Rauls, "Analysis and design of high frequency co-axial winding transformers," *MSc, University of Wisconsin-Madison, USA,* 1992.

[61] N. H. Kutkut, *An electric vehicle battery charging system*. University of Wisconsin--Madison, 1995.

[62] R. B. Bird, "WE Stewart, and EN Lightfoot," *Transport phenomena,* vol. 11, p. 5, 1960.

[63] D. C. Montgomery, E. A. Peck, and G. G. Vining, *Introduction to linear regression analysis*. John Wiley & Sons, 2021.

[64] T. Zarei, "Analysis of reliability improvements of transformers after application of dynamic rating," 2017.

[65] A. El-Shahat, R. J. Haddad, R. Alba-Flores, F. Rios, and Z. Helton, "Conservation Voltage Reduction Case Study," *IEEE Access,* vol. 8, pp. 55383-55397, 2020.

[66] G. McLorn, J. Morrow, D. Laverty, R. Best, X. Liu, and S. McLoone, "Enhanced ZIP load modelling for the analysis of harmonic distortion under Conservation

Voltage Reduction," *CIRED-Open Access Proceedings Journal,* vol. 2017, no. 1, pp. 1094-1097, 2017.

[67] H. Johal, "Distributed series reactance: a new approach to realize grid power flow control," Georgia Institute of Technology, 2008.